Università degli Studi di Torino

Corso di Dottorato in Fisica Sperimentale
(XIX Ciclo)

dottorando:
Roberto GEMME

Study of the ALICE ZDC detector performance

Relatore: Prof. M.Gallio

Contro-Relatore: Prof. E.Menichetti

Torino, 21 Dicembre 2006

Contents

Chapter 1

The ZDC detector for the ALICE experiment

1.1 The physics of ultra-relativistic heavy-ion collisions

High-energy physics has established and validated over the last decades a detailed, though still incomplete, theory of elementary particles and their fundamental interactions, called the Standard Model. Applying and extending the Standard Model to complex and dynamically evolving systems of finite size is the aim of ultra-relativistic heavy-ion physics. The focus of heavy-ion physics is to study and understand how collective phenomena and macroscopic properties, involving many degrees of freedom, emerge from the microscopic laws of elementary-particle physics. Specifically, heavy-ion physics addresses these questions in the sector of strong interactions by studying nuclear matter under conditions of extreme density and temperature.

The occurrence of phase transitions in quantum fields at characteristic energy densities, predicted by the Standard Model, affects crucially our current understanding of both the structure of the Standard Model at low energy and of the evolution of the early Universe. According to Big-Bang cosmology, the Universe evolved from an initial state of extreme energy density to its present state through rapid expansion and cooling, thereby traversing the series of phase transitions predicted by the Standard Model. Global features of our Universe, like baryon asymmetry or the large scale structure (galaxy distribution), are believed to be linked to characteristic properties of these phase transitions.

Within the framework of the Standard Model, the appearance of phase transitions involving elementary quantum fields is intrinsically connected to

the breaking of fundamental symmetries of nature and thus to the origin of the mass. In general, intrinsic symmetries of the theory, which are valid at high-energy densities, are broken below certain critical energy densities. Particle content and particle masses originate as a direct consequence of the symmetry-breaking mechanism. Lattice calculations of Quantum ChromoDynamics (QCD), the theory of strong interactions, predict that at a critical temperature of $\simeq 170MeV$, corresponding to an energy density of $\varepsilon_c \simeq 1GeVfm^{-3}$, nuclear matter undergoes a phase transition to a deconfined state of quarks and gluons [1]. In addition, chiral symmetry is approximately restored and quark masses are reduced from their large effective values in hadronic matter to their small bare ones.

In ultra-relativistic heavy-ion collisions, one expects to attain energy densities which reach and exceed the critical energy density ε_c, thus making possible the QCD phase transition, the only one predicted by the Standard Model that is within reach of laboratory experiments.

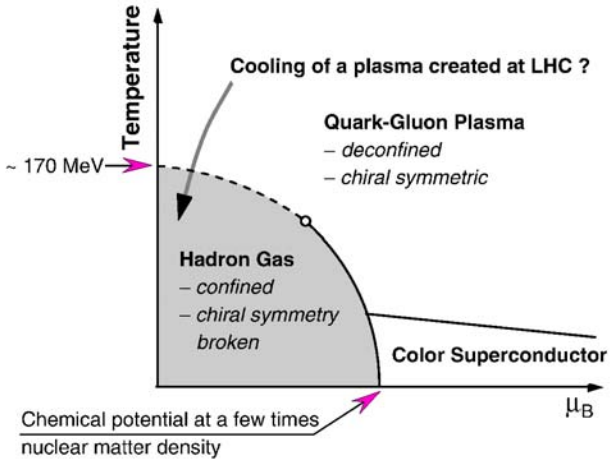

Fig. 1.1: *QCD phase diagram. The variable in abscissa is the chemical potential μ_B (baryon-number density). The solid lines indicate likely first-order transitions, while the dashed line indicate a possible region of a continuous but rapid crossover transition.*

The main objective of heavy-ion physics is to explore the phase diagram (Fig. 1.1) of strongly interacting matter, to study the QCD phase transition and the physics of the Quark Gluon Plasma (QGP) state. However, the system created in heavy-ion collisions undergoes a fast dynamical evolution from the extreme initial conditions to the dilute final hadronic state. The understanding of this fast evolving system is a theoretical challenge which goes far

beyond the exploration of equilibrium QCD. It provides the opportunity to further develop and test a combination of concepts from elementary-particle physics, nuclear physics, equilibrium and non-equilibrium thermodynamics, and hydrodynamics in an interdisciplinary approach [2].

1.2 The ALICE experiment at the LHC

ALICE (A Large Ion Collider Experiment) is a general-purpose heavy-ion experiment designed to study the physics of strongly interacting matter and the quark-gluon plasma in nucleus-nucleus collisions at the LHC.

ALICE will study the role of chiral symmetry in the generation of mass in composite particles (hadrons) using heavy-ion collisions to attain high-energy densities over large volumes and long timescales. This experiment will investigate equilibrium as well as non-equilibrium physics of strongly interacting matter in the energy density regime $\varepsilon \simeq 1 - 1000 GeV fm^{-3}$. In addition, the aim is to gain insight into the physics of parton densities close to phase-space saturation, and their collective dynamical evolution towards hadronization (confinement) in a dense nuclear environment. In this way, one also expects to gain further insight into the structure of the QCD phase diagram and the properties of the QGP phase [2].

Moreover, the results of heavy ion experiments, like ALICE, are expected to have an impact on various astrophysical fields. For example, they might be of relevance for the understanding of the dynamics of supernova explosions and the stability of neutron stars, which depends on the compressibility and therefore on the equation of the state of nuclear matter, since the core of the neutron stars could consist of cold and extremely dense nuclear matter [3].

1.2.1 ALICE experimental program

To establish experimentally the collective properties of the hot and dense matter created in nucleus-nucleus collisions, ALICE aims firstly at accumulating sufficient integrated luminosity in Pb-Pb collisions at $\sqrt{s} = 5.5 TeV$ per nucleon pair. However, the interpretation of these experimental data relies considerably on a systematic comparison with the same observables measured in proton-proton and proton-nucleus collisions as well as in collisions of lighter ions. In this way, the phenomena truly indicative of the hot equilibrating matter can be separated from other contributions.

The successful completion of the heavy-ion programme thus requires the study of pp, pA and lighter A-A collisions in order to establish the benchmark processes under the same experimental conditions. In addition, these

measurements are interesting in themselves. In fact, due to its excellent tracking and particle identification capabilities, the ALICE pp and pA programmes complement those of dedicated pp experiments (ATLAS, CMS). Finally, within the capabilities of ALICE there are also other physics subjects like ultra-peripheral collisions and cosmic-ray physics [2].

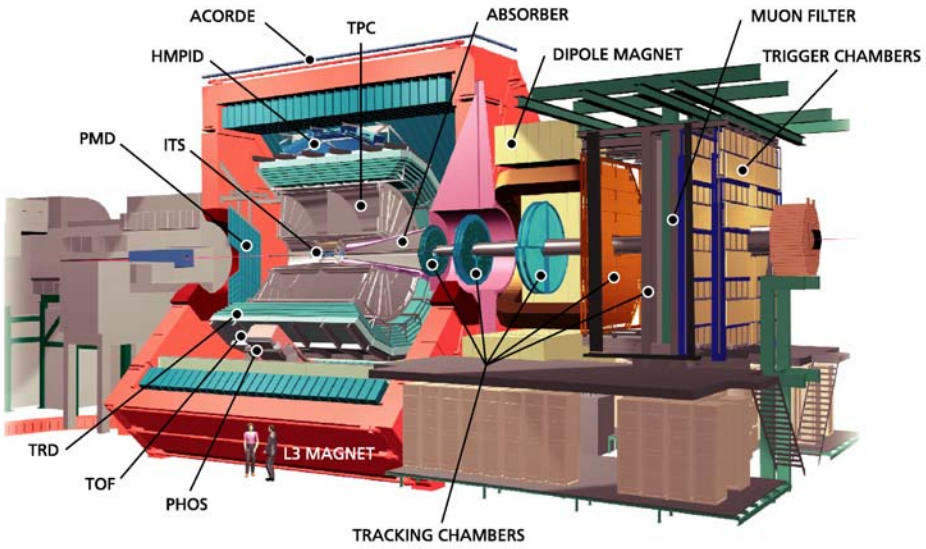

Fig. 1.2: *Layout of the ALICE detector.*

1.2.2 ALICE detector overview

The ALICE experiment, shown in Fig. 1.2, consists of a central detector system, covering mid-rapidity ($|\eta| \leq 0.9$) over the full azimuth, and several forward systems [2].

The central system is installed inside a large solenoidal magnet which generates a magnetic field of $\leq 0.5T$. The central system includes, from the interaction vertex to the outside, six layers of high-resolution silicon detectors (Inner Tracking System-ITS), the main tracking system of the experiment (Time-Projection Chamber-TPC), a transition radiation detector for electron identification (Transition-Radiation Detector-TRD), and a particle identification array (Time-Of-Flight-TOF).

The central system is complemented by two small-area detectors: an array of ring-imaging Cherenkov detectors ($|\eta| \leq 0.6$, 57.6° azimuthal coverage)

for the identification of high-momentum particles (High-Momentum Particle Identification Detector-HMPID), and an electromagnetic calorimeter ($|\eta| \leq 0.12$, 100° azimuthal coverage) consisting of arrays of high-density crystals (PHOton Spectrometer- PHOS).

The large rapidity systems include a muon spectrometer ($-4.0 \leq \eta \leq -2.4$, on the right side of the solenoid), a photon counting detector (Photon Multiplicity Detector-PMD, on the opposite side), an ensemble of multiplicity detectors (Forward Multiplicity Detector-FMD) covering the large rapidity region (up to $\eta = 5.1$). An absorber positioned very close to the vertex shields the muon spectrometer. The spectrometer consists of a dipole magnet, five tracking stations, an iron wall (muon filter) to absorb remaining hadrons, and two trigger stations behind the muon filter.

A system of scintillators and quartz counters (T0 and V0) will provide fast trigger signals, and two sets of hadronic calorimeters, located at 0° and about 116 m away from the interaction vertex, will measure the impact parameter (Zero-Degree Calorimeter-ZDC).

1.3 The Zero Degree Calorimeter detector

1.3.1 Introduction

In heavy-ion interactions many QGP signatures manifest themselves as a threshold behaviour of certain observables (e.g. production of charmonia and bottomonia states, strangeness) as a function of the energy density, estimated through the centrality of the collision. A good resolution on the centrality measurement is therefore essential, in order to properly probe the existence of such a threshold, which could otherwise be smeared out [5].

The observable most directly related to the geometry of the collision is the number of participant nucleons, which can be estimated by measuring the energy carried in the forward direction (at zero degree relative to the beam direction) by non-interacting (spectator) nucleons. The zero degree forward energy decreases with increasing centrality. Spectator nucleons will be detected in ALICE by means of Zero-Degree Calorimeters (ZDC) [2].

1.3.2 Detector layout

In the ALICE experiment, two identical sets of hadronic calorimeters will be located at opposite sides with respect to the beam Intersection Point 2 (IP2), 116 meters away from it, where the distance between the beam pipes ($\sim 8cm$) allows the insertion of a detector.

At this distance, spectator protons are spatially separated from neutrons by the magnetic elements of the LHC beam line. Therefore two distinct detectors will be used: one for spectator neutrons (ZN), placed at zero degrees relative to the LHC axis, and one for spectator protons (ZP), placed externally to the outgoing beam pipe on the side where positive particles are deflected (see Fig. 1.3) [2, 5, 8].

Moreover, to improve the centrality trigger, the ZDC project includes two small forward electromagnetic calorimeters (ZEM), that will be placed at about 7 m from IP2, on the side opposite to the muon spectrometer, out of the emission cone of spectators [2, 5].

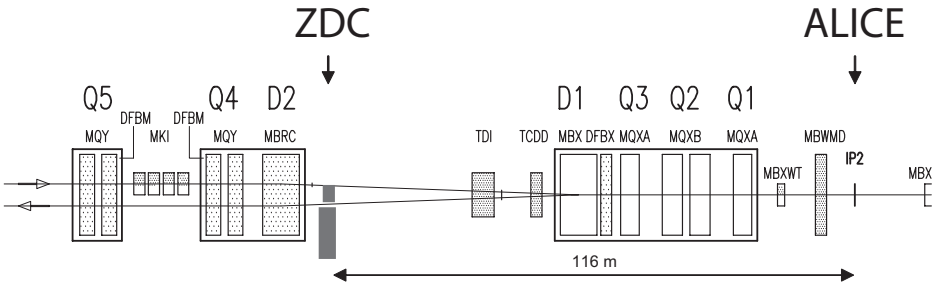

Fig. 1.3: *Schematic view of the beam line and the ZDC location.*

1.3.3 Detection technique

The quartz fibres calorimetry technique [9] has been adopted for the ALICE ZDC. The shower generated by incident particles in a dense absorber (the so-called *passive* material) produces Cherenkov radiation in quartz fibres (*active* material) interspersed in the absorber.

This technique fulfils two fundamental requirements. On one hand, due to the small amount of space available (particularly for the neutron calorimeter), the detectors need to be compact and therefore a very dense passive material must be used for the absorber to contain the shower. On the other hand, the ZDC will operate in a very high radiation environment (about $10^4 Gyday^{-1}$ is the estimated dose for the neutron calorimeter at a luminosity of $10^{27} cm^{-2} s^{-1}$): radiation hardness is guaranteed by the high radiation resistance of quartz fibres. In fact a quartz fiber calorimeter has been successfully used in the heavy ion fixed target experiment NA50 at the CERN SPS [6, 7], where the radiation damage is 10 times higher than the one expected at the LHC.

Furthermore, Cherenkov effect has two more advantages: it provides a very fast signal due to the intrinsic speed of the emission process and it shows a very low sensitivity to induced radioactivation thanks to its threshold behaviour [2, 5, 8].

1.3.4 Hadron calorimeters

Since the neutron ZDC (ZN) has to be placed between the two beam pipes, it has the most severe geometrical constraint and therefore the detector active transverse dimension should not be greater than 7 cm (1 cm is left for the box containing the detector). For this reason a very dense passive material must be used to maximize the containment of showers generated by spectator neutrons. The spectator nucleon momentum distribution is centered on the beam nucleon momentum (2.76 TeV), and its width is given by the Fermi motion.

For the proton calorimeter (ZP) there are no such stringent space constraints. Moreover, spectator proton distribution on the ZP front face is spread over the horizontal coordinate by the separator magnet D1 (of the LHC beam optics): 90% of the detected protons hit a $12.6 \times 2.8\ cm^2$ area [10, 5]. A larger detector made of a less dense material can therefore be used.

The energy resolution of the ZDCs is a fundamental parameter in the design of the devices. The physics performance of the detector for the measurement of the centrality of the collision is in fact directly related to the resolution on the number of spectator nucleons which hit the calorimeters front faces. For a reliable estimation of the centrality variables, the calorimeter energy resolution should be comparable to the spectator energy fluctuations at a fixed impact parameter. These fluctuations range from $\approx 20\%$ for central events to $\approx 5\%$ for peripheral ones, according to simulations that use HIJING as event generator [2, 8]. Moreover the detection of spectator nucleons on the two IP sides, with two symmetrically positioned sets of ZDCs, allows to increase the resolution on the spectator determination [4].

The ZDC response is very fast (of the order of few nanoseconds), thanks to the intrinsic speed of the emission process, making such a detector suitable for triggering purposes. Given the expected collision rate of 8 kHz for Pb-Pb hadronic collisions, we do not foresee any pile-up in the ZDCs. Even the much higher electromagnetic interaction rate, which is expected to be of the order of 0.1 MHz, should not pose any particular problem [2, 8].

The Tab. 1.1 contains a summary of the technical specifications for the ZN and ZP detectors. In the following further details on the detector main characteristics are reported.

Tab. 1.1: *Synopsis of ZDCs' parameters.*

Detector	ZN	ZP
Dimensions	$7.2 \cdot 7.2 \cdot 100$ cm^3	$22.8 \cdot 12 \cdot 150$ cm^3
Filling ratio	1/22	1/65
Absorber	W-alloy	brass
Density	17.6 g/cm^3	8.48 g/cm^3
Number of slabs	44	30
Slab's thickness	1.6 mm	4 mm
Number of fibres	1936	1680
Fibre spacing	1.6 mm	4 mm
Fibre diameter (silica core)	365 μm	550 μm
Numerical aperture	0.22	0.22
Number of PM	5	5
Type of PM	Hamamatsu R329-02	Hamamatsu R329-02

The neutron calorimeters

Each ZN is made by 44 grooved W-alloy slabs (93.5% of W), each of them 1.6 mm thick, stacked to form a parallelepiped of $7.2 \times 7.2 \times 100\,cm^3$. The active part of the detector is made of 1936 quartz fibers, embedded in the absorber with a pitch of 1.6 mm, corresponding to a filling ratio, i.e. the ratio between the active and the absorber volume, of 1/22.

The quartz fibers are of the HCG-M-365-U type (manufactured by SpecTran Specialty Optics Company, USA) and have a pure silica core, fluorinated silica cladding and a hard polymer coat with a diameter of 365, 400 and 430 μm respectively. The numerical aperture is 0.22[1].

The fibers, hosted in the slab grooves, are placed at 0° with respect to the incident particle direction and come out from the rear face of the calorimeter, directly bringing the light to the photomultipliers.
Although in these calorimeters the maximum light yield is obtained with the fibers oriented at 45° with respect to the incident particle direction [9], our choice of having the fibers placed at 0°, still leads to an acceptable energy resolution. In fact at the LHC energy the light yield is so large that the

[1]SpecTran Specialty Optics Company Specifications

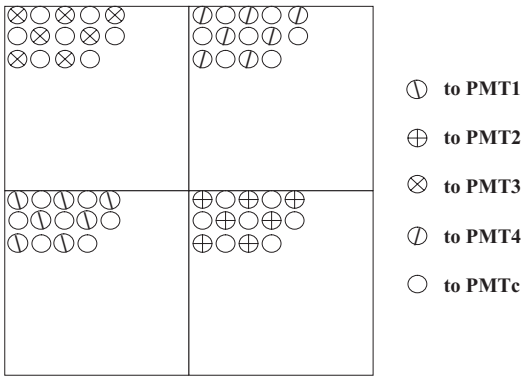

Fig. 1.4: *Schematic connections of the fibers to the PMTs for the ZN detector.*

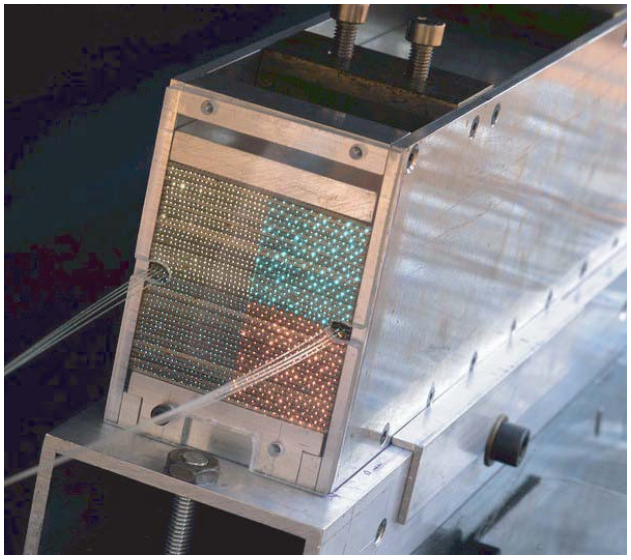

Fig. 1.5: *Front face of the ZN calorimeter; the quartz fibers connecting the laser diode to PMTs are visible.*

statistical fluctuation on the number of photoelectrons does not contribute significantly to the energy resolution of the detector.

One out of two fiber is sent to a common photomultiplier (PMTc), while the remaining fibers are collected in bundles and sent to four different photomultipliers (PMT1 to PMT4) forming four independent towers (as shown in Fig. 1.4). This segmentation allows to check the relative behaviour of the different towers. The information coming from the PMTc provides a complementary measurement of the shower's energy, in particular useful for calibration purposes. Moreover using the responses coming from the four ZN towers it is experimentally possible the estimate of the centroid of the spectator neutrons spot on the calorimeter front face. In this way it is possible to continuously monitor the beam crossing angle at IP2 [8] and to measure event by event the 1^{st}-order event plane [34], as discussed in Chap.6.

The photomultiplier type chosen for the detector is the Hamamatsu R329-02, a 12-stage PMT, with quantum efficiency around 25%. The stability of the gain of each PMT will be monitored by means of a laser diode, optically connected to each photomultiplier by means of quartz fibers.

The two final detectors (ZN1 and ZN2) have been assembled between June 2002 and June 2003. Their technical characteristics are identical and their performance comparable. Chapters 3 and 5 will refer to recent results obtained by testing ZN2.

Fig. 1.5 shows a photograph of the ZN calorimeter.

The proton calorimeters

The design of the proton calorimeters is conceptually similar to that of the neutron ones. Each proton calorimeter uses brass as absorber material and its dimensions are $22.8 \times 12 \times 150\ cm^3$. The calorimeter consists of 30 grooved brass plates, each of them 4 mm thick[5, 19] (see Fig. 1.6).

The grooves run parallel to the beam axis and host 1680 quartz fibres with a pitch of 4 mm corresponding to a filling ratio, i.e. the ratio of active volume to the absorber volume, of 1/65.

The fibres are of HCG-M-550-U type (manufactured by SpecTran Specialty Optics Company, USA). The pure silica core, the silica fluorinated cladding and the hard polymer coat diameters are 550, 600 and 630 μm, respectively. The numerical aperture is 0.22[2].

The fibres come out from the rear face of the calorimeter and, as for the neutron calorimeter, the optical redout has been divided into five PMTs. One of the PMTs collects the light of half of fibers uniformely distributed

[2]SpecTran Specialty Optics Company Specifications

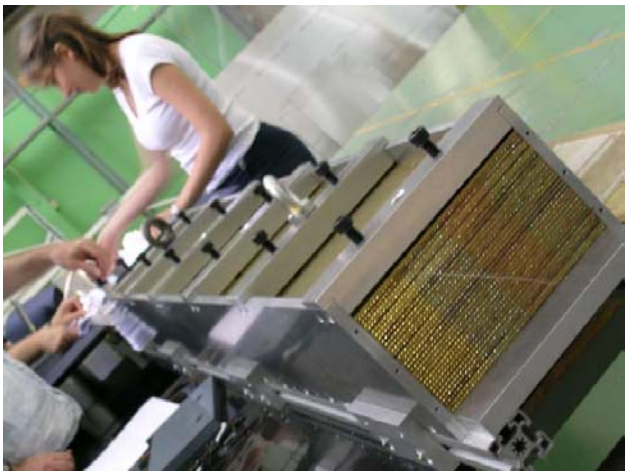

Fig. 1.6: *Photo of the ZP calorimeter at the end of the assembly phase.*

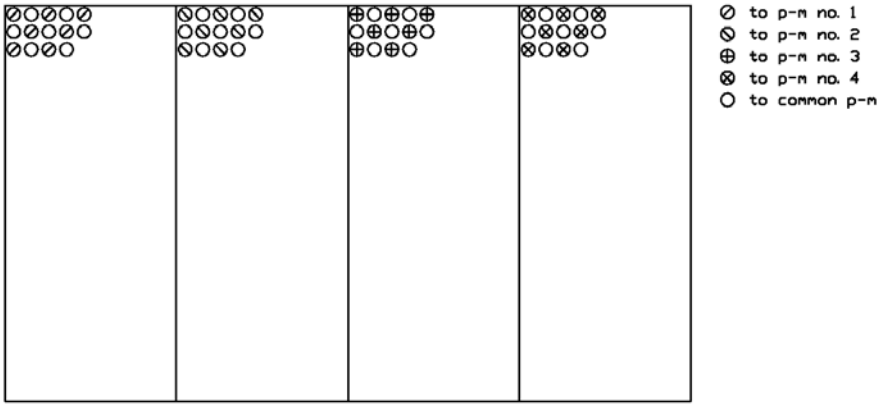

Fig. 1.7: *Schematic connections of the fibres to the PMTs for the ZP detector.*

inside the calorimeter. With the remaining fibers four towers, read out by four PMTs, are defined. The schematic arrangement of the fibers is shown in Fig. 1.7. This segmentation allows to check the relative behaviour of the different towers. Moreover the informations coming from the four ZP independent towers are helpful when the Zero Degree Calorimeters are used to measure the centrality in pA collisions, by means of the detection of the grey and black nucleons, i.e. the slow nucleons emitted in this kind of collisions. In fact, thanks to the ZP segmentation it is possible to separate the contribution of the grey and black protons which have different momenta [4].

As the signals from the PMTs of the proton calorimeters are of the same order of magnitude as those from the neutron ones, the same type of photodetectors have been used.

The two final proton detectors (ZP1 and ZP2) have been assembled between July 2004 and November 2005. Chapter 4 will refer on the recent results obtained by testing ZP1.

1.3.5 Electromagnetic calorimeters

To improve the centrality trigger, the ZDC project is complemented by a couple of forward electromagnetic calorimeters(ZEM). These detectors are designed to measure, event by event, the energy of particles emitted at forward rapidities, essentially photons generated from π^0 decays.

The detection technique employed for the electromagnetic calorimeter is the same as the one used for the hadronic calorimeters. The most important difference consists in the choice of the angle of the fibres relative to incoming particles. Fibres are oriented at 45°, while for the hadronic calorimeters they are at 0°. This choice maximizes the detector response, since Cherenkov light production has a pronounced peak around 45°. Each electromagnetic calorimeter is made of lead, with quartz fibres sandwiched in layers between the absorber plates. Two consecutive planes of fibres are separated by a lead thickness of 3mm which, due to the 45° inclination, results in a total thickness of 4.24mm seen by incident particles. Fibre cores have a diameter of 550 μm and the active to passive volume ratio is about 1/11. The resulting calorimeter dimensions are $7 \times 7 \times 21\, cm^3$, the total absorber length corresponding to about 30 radiation lengths. This condition assures the total containment of showers generated by participants [2].

In order to allow a detection of a significant number of particles produced in the interaction, the chosen position for the ZEM calorimeters is at about 7m from the IP, just before the coils of the first compensator dipole. Two devices will be placed on the same side relative to the IP, on the side opposite

to the dimuon arm. In this configuration the electromagnetic devices cover the pseudo-rapidity range $4.8 < \eta < 5.7$ [2].

1.3.6 Centrality determination using the ZDC

In ion-ion collisions, the determination of the variables that characterize the geometry of the collision is an essential prerequisite to the study of any physics observable. The impact parameter b and other quantities related to it by geometry (e.g. number of participant nucleons N_{part} or number of nucleon-nucleon collisions N_{coll}) can be extracted in a rather model-independent way from either charged-particle multiplicity or from zero-degree energy E_{ZDC}, corresponding to the energy carried by spectator nucleons detected in the Zero Degree Calorimeters.

As shown in Fig. 1.8, in a central collision almost all nucleons are involved in the collision and loose large amount of energy in a small volume [28]. It is in this excited hot region, called fireball, that one could expect to attain the conditions for QGP formations. Few nucleons survive the interaction and arrive to the ZDCs: hence a small amount of E_{ZDC} will be detected.

Fig. 1.8: *Schema of the geometry of a central collision.*

Fig. 1.9: *Schema of the geometry of a peripheral collision.*

In a peripheral collision, on the contrary, only few participants undergo a collision and release their energy in the fireball. Almost all other nucleons hold their direction, carrying the same energy as the beam nucleons(Fig. 1.9). Those nucleons fly towards the ZDC and a large E_{ZDC} will be detected.

Hence the measured energy E_{ZDC} is directly proportional to the impact parameter of the collision.

However, in heavy ion collisions nuclear fragments are produced and, unfortunately, at colliders they are lost in the beam pipes, owing to their magnetic rigidity, very close to that of the beam. Considering fragments production, the monotonic correlation between E_{ZDC} and the impact parameter is conserved only up to $\sim 11\ fm$, but it is destroyed for very peripheral events (Fig. 1.10). Therefore the detection of the spectator energy alone can not be used to unambiguously determine centrality. For that reason, the information provided by the forward electromagnetic calorimeters (ZEM) will be used to identify very peripheral collisions and to remove the ambiguity. As can be seen in Fig. 1.11, the energy detected in such calorimeters is anti-correlated with the impact parameter. The correlation between the total energy detected in the electromagnetic calorimeters and the energy measured by ZDC is shown in Fig. 1.12. It is clear that the central events can be identified choosing an appropriate threshold on the total energy detected by the e.m. calorimeters[5, 2, 4].

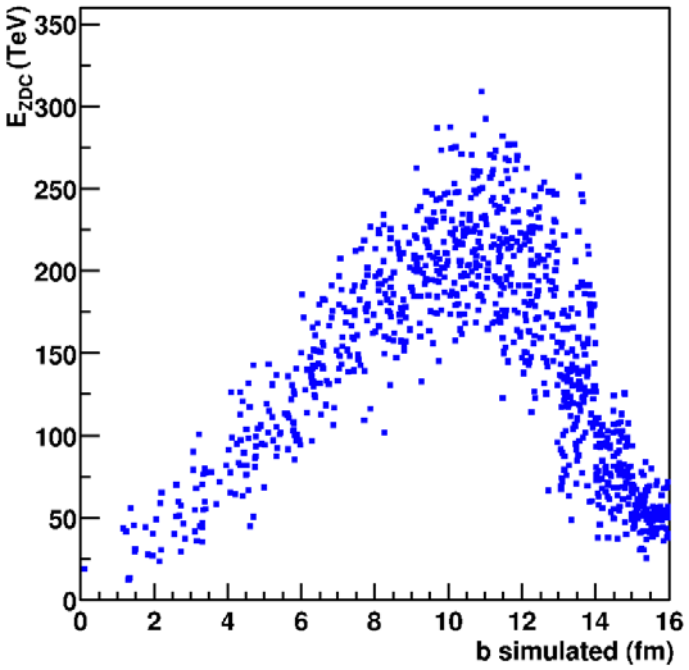

Fig. 1.10: *The total energy measured by the ZDCs as a function of the impact parameter.*

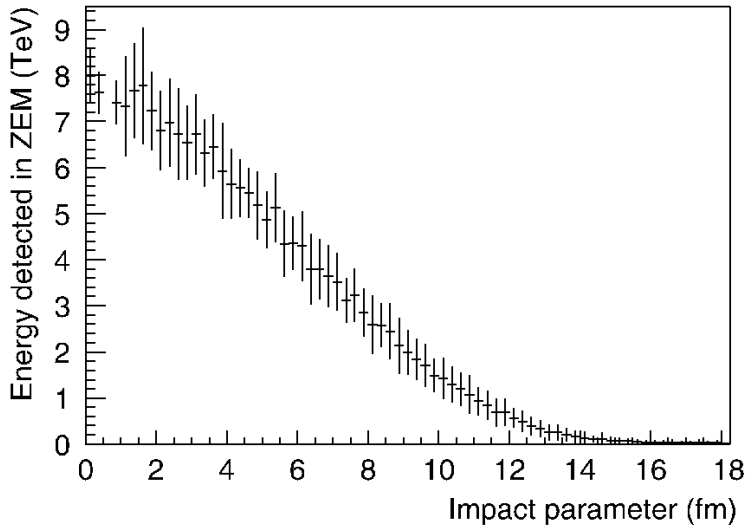

Fig. 1.11: *Energy detected by two zero-degree electromagnetic calorimeters as a function of the impact parameter.*

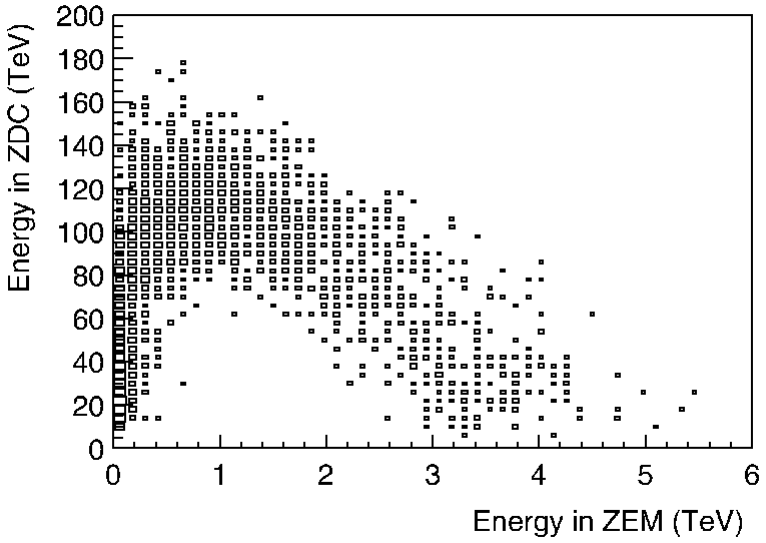

Fig. 1.12: *Correlation between the energy measured by the ZEM and the ZDC detectors.*

1.3.7 The ZDC as a luminosity monitor

During operation with heavy-ion beams, the LHC luminosity can be measured and monitored by means of the ZDCs [5].

The basic idea is to measure the rate of mutual electromagnetic dissociation in the neutron channel.

When two nuclei A and B collide at impact parameter b larger than the sum of the nuclear radii, the interaction is purely electromagnetic. At ultra-relativistic energies, each nucleus experiences the strongly Lorentz-contracted Coulomb field of the other nucleus. According to the Weizsacker-Williams method, this field can be expressed in terms of an equivalent virtual photon spectrum.

The virtual photons radiated by the nuclei can excite the Giant Dipole Resonance (GDR) in both of the colliding nuclei. Since the GDR decays mainly by emitting one neutron, the process can be identified by detecting simultaneously one neutron in each of the neutron calorimeters placed on both sides of the interaction point.

The measured rate dN^m/dt of mutual e.m. dissociations in the neutron channel is proportional to the luminosity L:

$$\frac{dN^m}{dt} = L \cdot \sigma^m. \tag{1.1}$$

Therefore, the luminosity can be immediately deduced since the cross-section for mutual e.m. dissociation in the neutron channel for Pb-Pb interactions at the LHC is known ($\sigma^m_{Pb} = 0.535\,b$).

Moreover the choice of this process for the luminosity measurement offer a further advantage: in fact this reaction is relatively background free and can be detected with full acceptance, implying a rather precise measurement of the reaction rate.

1.3.8 The ZDC and the ALICE trigger system

The ALICE trigger system is foreseen to work on three level (L0, L1, L2) [5, 2].

The information on the event centrality provided by the ZDC detector is used at the L1 level. The ZDC signals are transmitted through long low-loss coaxial cables ($\sim 200\,m$) from the photomultipliers to the lowest counting room, where the trigger logic is built. The signals from all the photomultipliers of all the hadronic calorimeters are summed, in order to obtain a signal proportional to the total number of spectators coming out from the interaction. Three levels of discrimination will be applied to provide three Level 1

(L1) triggers, defining different centrality intervals: the first will select the most central events (10% of the total inelastic cross section), the second the semi-central events (15% of the total inelastic cross section) and the third the minimum bias events.

The informations on the electromagnetic dissociation events, provided by the neutron calorimeter signals, are sent both at the L0 and L1 level. The electromagnetic dissociation usually gives a signal equivalent to one nucleon. Therefore for each ZN detector a threshold window (between the noise and the physical minimum bias signal, expected to be equivalent to a few nucleons at least) select the signal due to one neutron. The coincidence of two such signals for the two sides of the IP, implemented in a programmable logic unit, can be considered as the trigger for the mutual e.m. dissociation events, that is sent to the L1 level. Moreover, since the counting room where the trigger logic is built lies on the right side of the IP, the signal of the neutron calorimeter on this side can provide a fast information on the e.m. dissociation events, that is sent to the L0 level. This signal is transmitted through an air core coaxial cable with a very high signal velocity ($\sim 0.87c$).

Finally, each analogue signal from all the ZDC photomultipliers will be sent to commercial ADC modules. When a L0 trigger is issued, the ZDC electronics will start to convert the signals and make them available for the data acquisition system (DAQ) if a positive L1 trigger is received.

Chapter 2

ZDC integration into the LHC

2.1 Introduction

In order to extract the physics performance of the ZDC it is necessary to study the detector responses in the frame of the whole ALICE experimental setup. Therefore simulations with the complete geometry of the ALICE detector and of the LHC beam line up to the ZDCs location are needed.

The analysis of detector response in the overall ALICE environment can give indications on the accuracy that can be reached in determining the physical observables that will be studied by the ZDCs [10].

Furthermore these simulations allow to study also technical details as the detector acceptances taking into account the other detectors and the tight link with the parameters of the beam line elements.

2.2 The simulation framework

AliRoot [11], the ALICE offline framework for simulation, reconstruction and analysis, makes use of Object-Oriented programming techniques and C++ as the implementation language. It is based on the ROOT package [12], providing container classes, histogramming, data analysis and graphical user interfaces. The geometry description tools are provided by GEANT 3.21 code [26], which is used also as tracking engine. In fact it provides particle transport through the geometry and simulates the interaction between particles and the materials of detectors and structural elements.

Thanks to the C++ inheritance property, it is possible to develop base classes which contain virtual common methods and derived classes in which these methods can be implemented according to class requirements and more specific functions can be declared, preserving code modularity [10].

For example, each ALICE detector has to implement a detector simulation class derived from base classes. Therefore, for each detector code, common methods that are purely virtual in the base classes are implemented. Detector classes contains the geometry description, together with materials and tracking media definition. They also have to provide a *StepManager* to be processed at each transport step, methods to store informations from tracking and from detector response simulation. Finally also an algorithm for reconstruction has to be implemented.

2.3 Classes for geometry description

The base classe for ZDC detector is *AliZDC*, which inherits from *AliDetector*. In the official committed version of AliRoot there are two classes that derive from *AliZDC*. The first one (*AliZDCv1*) contains the geometry corresponding to the TDR design [5], while in the second one (*AliZDCv2*) there is a more updated geometry [10]. This latter geometry foresees only one hadronic ZDC system, even if the experiment will have two of them. This is due to the fact that the definition of both systems implies a mother volume (i.e. the volume that contains all the other volumes) more than 200 m long and this would considerably slow down AliRoot simulations. The hadronic ZDCs are placed on the same side of the dimuon arm relative to IP. In the following we will refer to this side as to the right side, because it is on the right of an observer who look at the experiment from the LHC center. Both the electromagnetic calorimeters are included in *AliZDCv2* geometry. They are both placed on the left side relative to IP.

However the beam line elements are not exactly the same on the two

sides with respect the the IP. In particular, as we will discuss in the next section, two collimators (TDI, TCDD), whose apertures have to be carefully controlled, lies exclusively on the left side of the beam line. Therefore, in a local user version of AliRoot, the new classe *AliZDCv3* has been created. This classe contains the same *AliZDCv2* description of the right side, but it includes also a detailed description of the beam line elements geometry of the left side, up to the second system of hadronic calorimeters (see Fig.2.1).

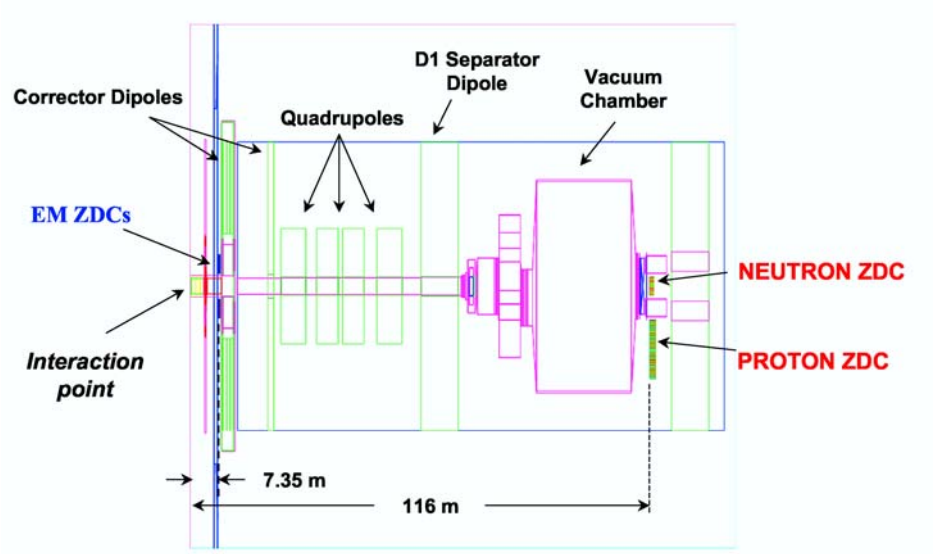

Fig. 2.1: *Representation of the left beam line from the interaction point to the ZDCs in the AliRoot framework. The picture is not to scale. In fact it is strongly compressed in the beam direction since from IP to the ZDCs the distance is 116 m, while, for example, the transverse dimention of the proton calorimeter is 22.8 cm.*

Naturally the description of the ALICE intersection region foresees the magnetic elements whose fields affect proton trajectories and consequently the ZP detector acceptances. The hadronic calorimeters are placed at 116 m from the IP; their position relative to the beam pipes is shown in Fig.2.2, where also the division in towers is schematically represented. The Fig.2.1 allows to see the location of the ZEM calorimeters. They lie at 7.35 m away from the IP, just before the first compensator magnet. In Fig.2.3 a front sketch of the two detectors is plotted to show their position relative to the beam pipe.

We used *AliZDCv3* esclusively to study the hadronic calorimeter acceptances. To performe this kind of study we switched off the shower develop-

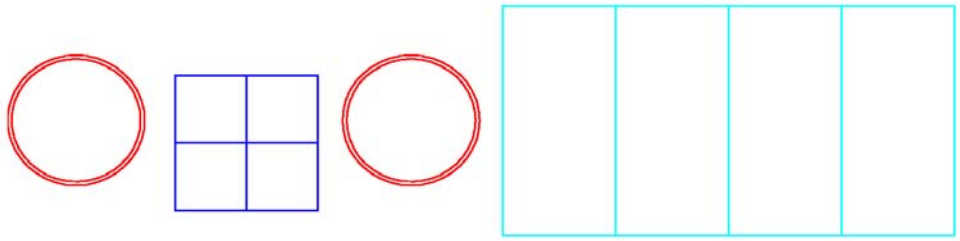

Fig. 2.2: *Front view of hadronic ZDCs at z=116.5 m from IP. The division in four towers can be seen for both detectors. Red circles represent beam pipes.*

Fig. 2.3: *Front view of the electromagnetic calorimeters placed on both sides of the beam pipe. The centers of the two detectors are 8 cm distant from the LHC axis.*

ment along the beam pipe and in the ZDC. In fact in this case the shower development, which is very time consuming, is not essential. To evaluate the effect on the detector acceptances of the various beam line elements we used as estimator simply the number of interacting nucleons in the structural elements. In this way we could work also with a mother volume 300 m long.

2.4 Collimation system at IP2

As can be seen Fig.2.4 the ALICE experiment is situated in a beam injection zone. For this reason along the left beam line a movable absorber (TDI) protects the immediately downstream LHC devices, in particular the superconducting dipole D1, from damages in case of injection kicker failures(see fig.2.5). A secondary collimator (TCDD) reduce damage risk, absorbing the scattered and secondary shower particles produced in the case of beam impact on the TDI[13].

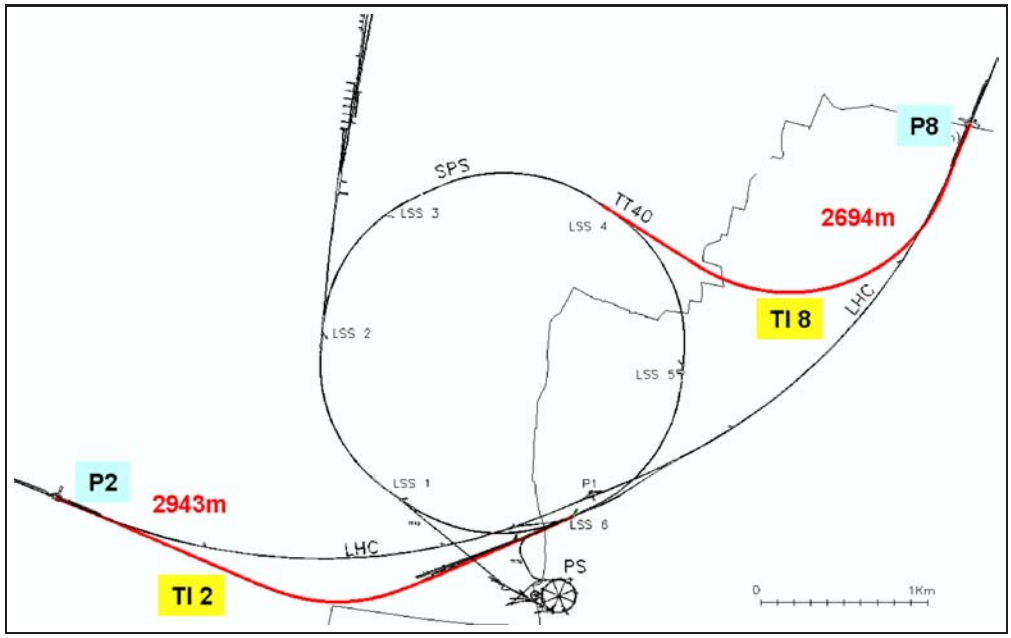

Fig. 2.4: *IP2 lies in a beam injection zone (LHC beam1).*

Moreover, as shown in fig. 2.6, the overall design of the LHC collimation system foresees tertiary collimators (TCTs and TCLIA) around the interaction points of the LHC, in order to protect the superconducting triplets against energy deposition of the beam halo (cleaning functionality) or possibly mis-kicked beam (machine protection functionality)[14, 15].

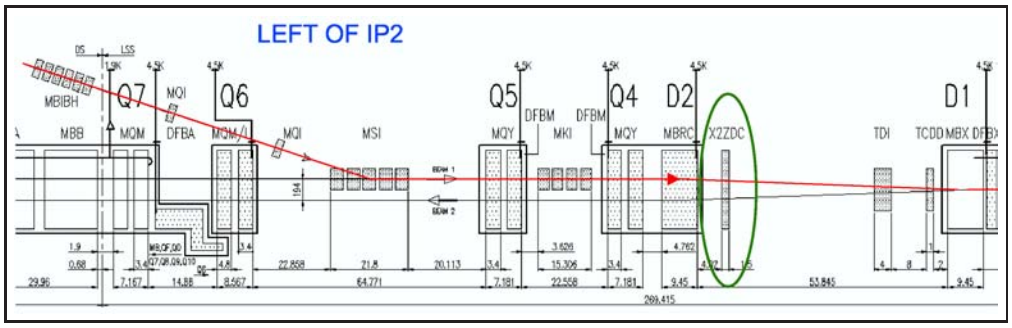

Fig. 2.5: *TDI and TCDD protects the LHC equipments in the injection zone.*

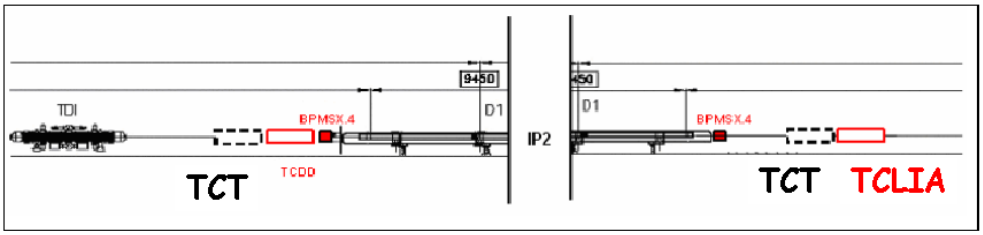

Fig. 2.6: *TCTs and TCLIA location.*

As discussed in the following the least apertures allowed at the location of these collimators by the ZDC acceptaces have been investigated by means of the simulation.

Finally it should be noticed that also the ZDCs lie in this injection zone and very close to circulating beams. Hence the detectors will be placed on remotely controlled movable tables and to protect the calorimeters from possible beam losses, they will be positioned about 20 cm below the beam level during the beam injection phase.

2.5 Tracking of spectator nucleons

In the simulation, spectator nucleons are generated at the IP, taking into account a beam crossing angle in the vertical plane of 100 μrad and the intrinsic beam divergence (30 μrad). The spectators are generated [10] with the nominal beam nucleon momentum of 2.76 TeV/c; also momentum broadening due to Fermi motion has been considered. The three components of the generated nucleon momentum are shown in Fig. 2.7. Being boosted by Lorentz trasformation, the longitudinal component of the Fermi momentum is crucial and it gives a spread of the order of 500 GeV/c for the longitudinal momentum of spectators.

Since any magnetic field encountered by protons gives a kick to their traiectories, the momentum spread of spectators protons results in a large horizontal dispersion after the separator dipole D1, and some of them are lost along the beam line. As can be seen in Fig. 2.8 the spectator proton distribution over ZP front face is enlarged: 90% of detected protons hit a $12.6 \times 2.8\ cm^2$ area.

For the spectator neutrons only the transverse component of the Fermi momentum plays a role in determining the size of the spot at the ZDC location, which is of the order of $0.6 \times 0.6\ cm^2$ at 1σ level (Fig. 2.9). Neutron losses are not expected along the beam line.

2.6 Spectator proton losses

As shown by the simulation, there are different parameters that affect proton calorimeter acceptance.

First of all the displacement in the horizontal plane of the closed beam orbit is very significant. In fact an I.P. displacement of 1 mm in the horizontal transverse direction can deteriorate of the 20% the ZP acceptance.

Other relevant LHC parameters are the apertures of the radio-frequency

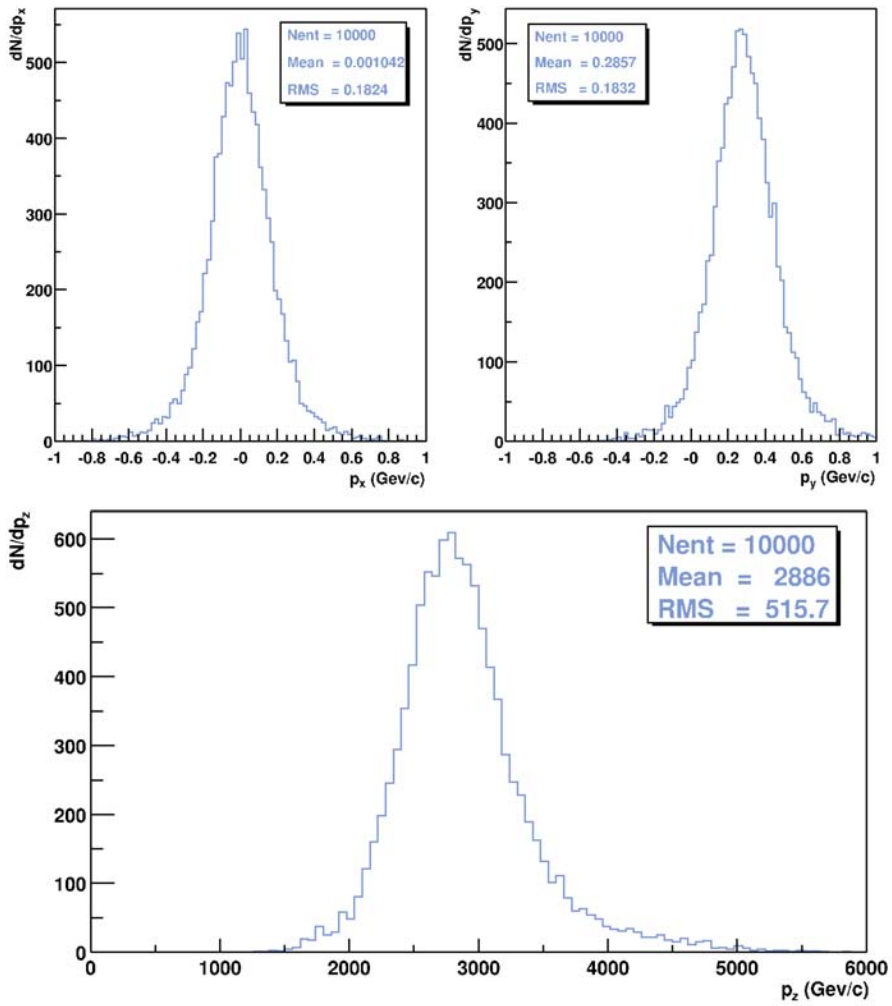

Fig. 2.7: *Components of nucleon momentum generated taking into account Fermi motion, beam divergence and crossing angle.*

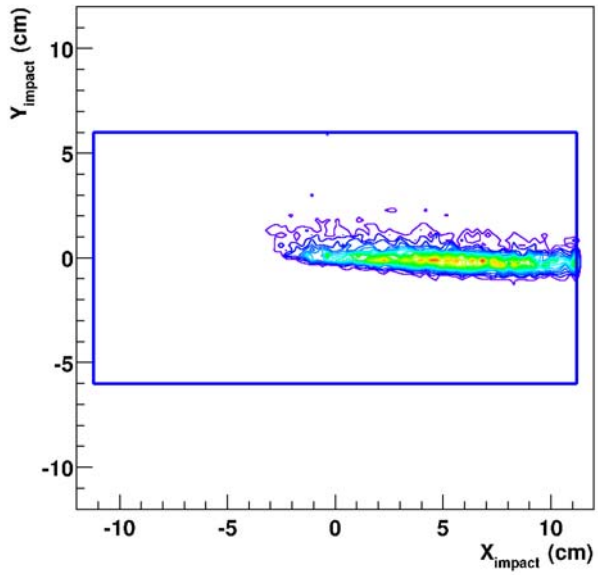

Fig. 2.8: *Spectator protons spot over the ZP front face, schematically represented by the blue box.*

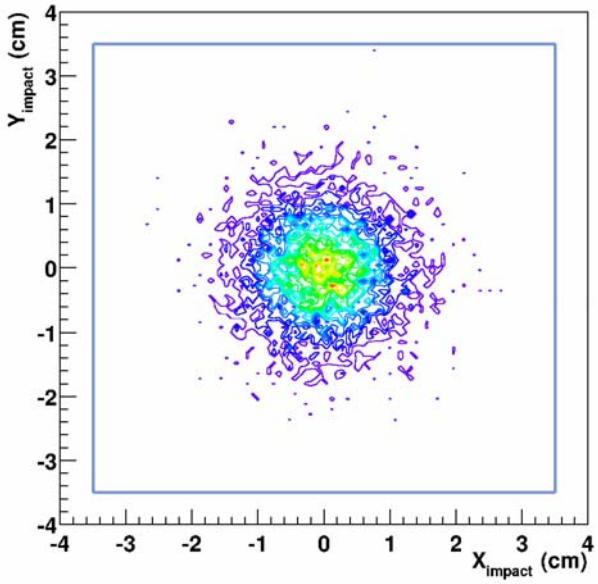

Fig. 2.9: *Spectator neutrons spot over the ZN front face, schematically represented by the blue box.*

screen in the collimators and in magnetic elements. Also the apertures of the others beam pipe components (straight sections, bellows, flanges) are important. Moreover it is needed to take into account the technical characteristics of the critical transition cone before recombination chamber, which is the element where the single beam pipe coming from the IP split into two separate beam pipes. These parameters have been carefully controlled with simulation and optimized, in a close interaction with LHC engineers, in order to reduce spectator proton losses.

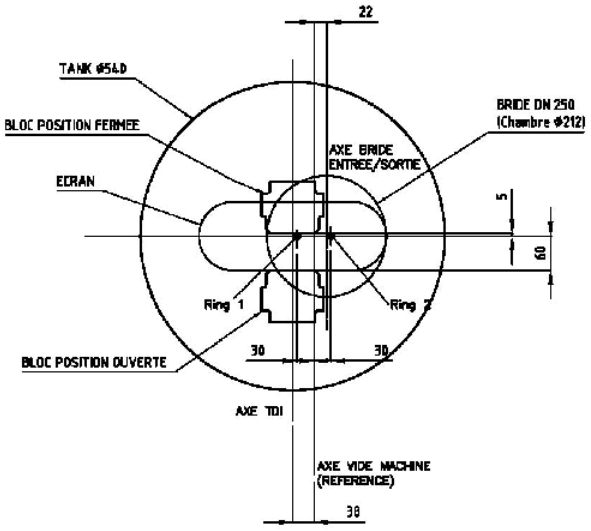

Fig. 2.10: *Technical specifications of the TDI.*

The TDI design (Fig.2.10) has been finalized, with new sizes and positions to fulfill both machine and ALICE ZDC aperture requirements. Last modifications to the TDI geometry have been evaluated and spectator proton losses are not expected in the radio-frequency beam screens of this collimator.

Looking at the spectator protons distributions at the entrance and at the exit of the zones reserved to the others collimators (see an example in Fig.2.11), we evaluated the aperture required in that regions to maximize the ZP acceptance. The results are shown, as a function of the distance from IP, in Fig.s 2.12 and 2.13, respectively for the left and for the right side of the beam line. In the same figures are represented also the apertures proposed by the LHC engineers in order to satisfy both ZP requirements and some standardization exigencies of the LHC assembly. We can see that the proposed apertures satisfy the ZDC needs.

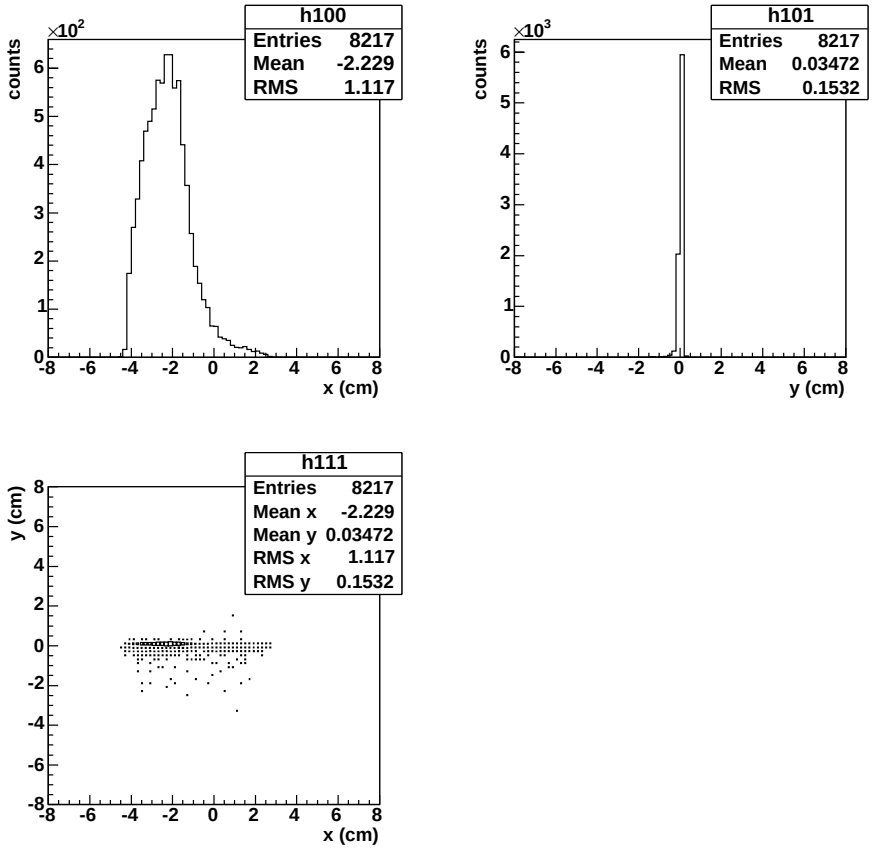

Fig. 2.11: *Spectator protons distribution in the transverse plane at the TCDD entrance.*

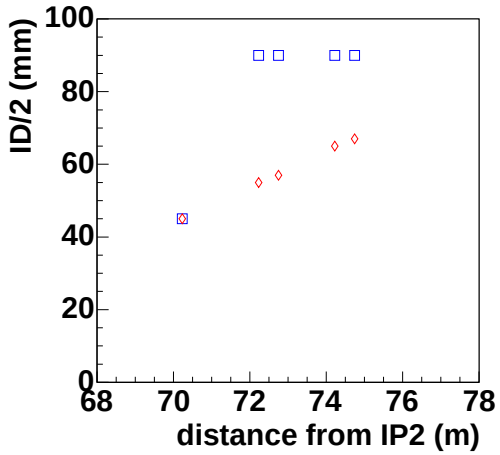

Fig. 2.12: *Comparison between ZP requirements (red symbols) and machine proposal (blue squares) for the apertures at the entrance and at the exit of TCDD and TCT collimators (left side of the beam line).*

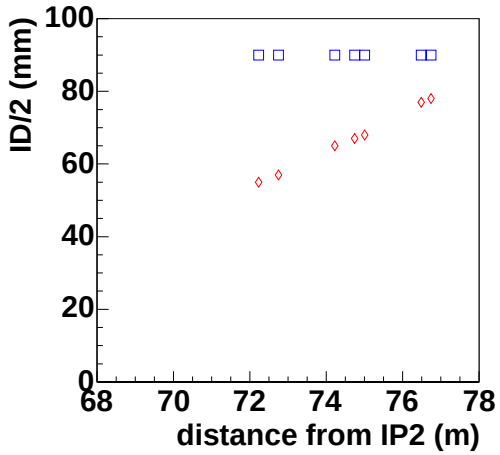

Fig. 2.13: *Comparison between ZP requirements (red symbols) and machine proposal (blue squares) for the apertures at the entrance and at the exit of collimators TCT and TCLIA (right side of the beam line).*

As can be seen in fig.2.14, all spectator protons cross the transition cone before the recombination chamber; for this reason the possibility of making a thin window in the transition cone region involved by ZP acceptance has been evaluated. Table 2.1 shows that the window has to be as thin as possible and the opening angle α of the cone has to be maximum, even if a technical constraint ($\alpha_{max} = 15°$) has to be taken into account.

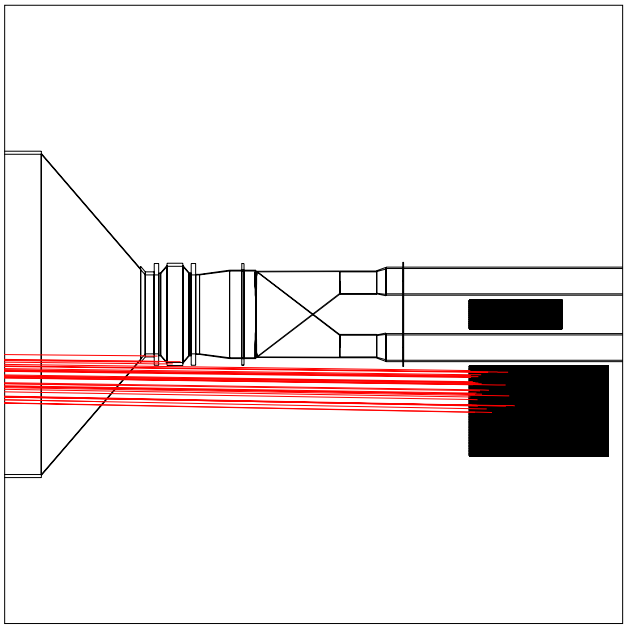

Fig. 2.14: *Spectator protons crossing the transition cone before recombination chamber.*

	α=12°	α=15°
8 mm	21.8%	17.7%
3 mm	9.3%	7.7%
2 mm	6.5%	4.8%

Tab. 2.1: *Spectator protons interacting in the transition cone window for different values of cone opening angle and window thickness.*

The Tab.2.2 summarizes the estimates of the spectator protons interacting in various elements of the beam line. It is clear that D1 aperture is the main limitation on the acceptance for spectator protons. Some protons arrive at the ZP location but are outside of its geometrical acceptance. Finally it

should be noticed that most of the particles produced in the protons interaction with the transition cone before recombination chamber release energy in the proton calorimeter; therefore the energy of those protons is not entirely lost. Spectator protons accepted in the proton zero degree calorimeter without interacting along the beam line are of the order of 66%.

Volume	interacting protons(%)
Inner Triplet	1.8%
D1 separator magnet	15.2 %
Transition cone before R.C.	8.4%
Flanges and straight sections	6.%
Outside ZP acceptance	2.6 %

Tab. 2.2: *Spectator protons interacting along the beam line.*

Chapter 3

Test of the ZN2 calorimeter with π^+ and e^+ beams

3.1 Introduction

This chapter reports on the results of the test performed on the second neutron zero degree calorimeter with positive hadron and positron beams with momenta ranging from 50 to 150 GeV/c. The test has been carried out in September 2003 at H6 beam line of CERN SPS. The main purpose of the beam test was to study the response and resolution of the detector as a function of the beam energy. The localizing capability, the response uniformity and the transverse profile of the detectable hadronic shower have also been studied [8].

3.2 Experimental set-up

The detector has been mounted on a table with remote x-y positioning in the plane transverse to the beam.

A MWPC, installed in front of the calorimeter, allowed an accurate reconstruction of the beam impact point, with a spatial resolution of ~ 200 μm.

A schematic view of the experimental set–up is shown in Fig. 3.1. The trigger has been provided by a plastic scintillator telescope S1 - S4. Two different triggers could be selected defining a beam spot of 1×1 cm^2 or 2×2 cm^2 on the detector front face. Muons are detected by means of two plastic scintillators MU1 and MU2, placed beyond an iron wall.

The charge of the signals from PMTs has been digitized using a Lecroy 2249W ADC module.

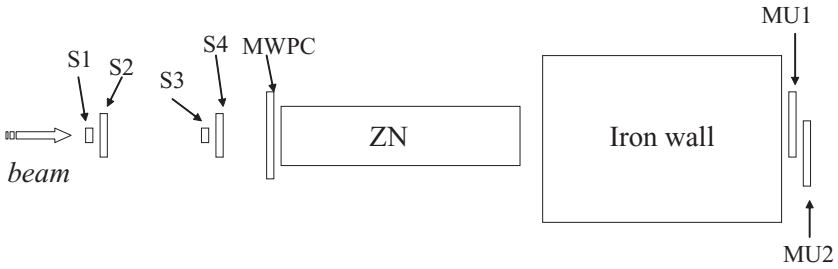

Fig. 3.1: *Schematic view of the experimental set–up. S1, S2, S3, S4: trigger scintillators; MU1, MU2: scintillators for muon detection; MWPC: chamber for beam impact point definition.*

At the beginning of the test the ZN towers have been equalized by using a 100 GeV/c positive hadron beam, which has been sent to the center of each tower. The high voltage of the PMTs of each tower has been tuned, in order to obtain the same mean value of the ADC spectrum. The PMTc high voltage has been set in order to get a response equal to the sum of the signals of the others four PMTs, when the beam hits the center of the calorimeter front face. In fact the PMTc is connected to a number of fibers four times larger than the other photodetectors.

A fine tuning of the calibration has then been performed in the offline analysis.

3.3 Test results

3.3.1 ADC spectra analysis

The ZN2 response has been calculated by summing, for each event, the five PMT's ADC values, after pedestal subtraction and applying the corresponding calibration coefficient.

The resulting ADC spectra were fitted with a gaussian–like function:

$$f(x) = Ne^{\frac{-(x-\mu)^2}{2\sigma^2(x)}}. \tag{3.1}$$

The term

$$\sigma(x) = \sigma_0 + \sigma_1 \frac{x-\mu}{\mu} \tag{3.2}$$

allows to take into account the asymmetry of the spectra.

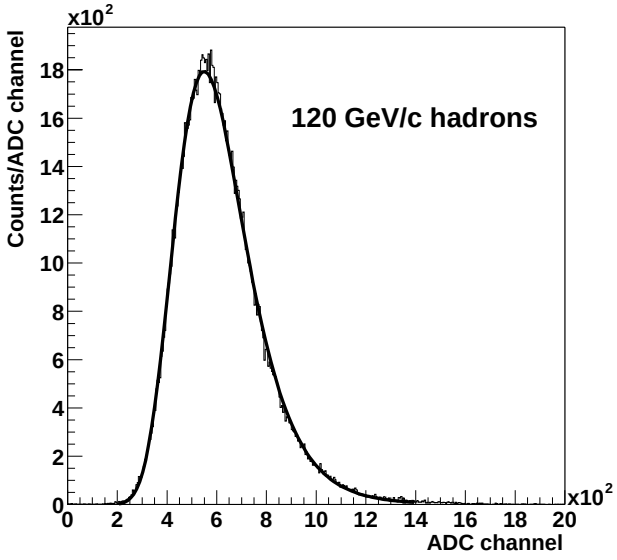

Fig. 3.2: *ZN2 response to a 120 GeV/c positive hadron beam impinging on the centre of the calorimeter.*

Fig. 3.2 shows the ZN2 response to a 120 GeV/c positive hadron beam impinging on the centre of the calorimeter.

The quartz fiber calorimeter is essentially sensitive to the e.m. component of the hadronic shower, due to the π^0 produced in the initial interactions.

The energy fluctuations of this e.m. component and the Poisson fluctuation on the number of the produced π^0 are responsible of the non Gaussian shape of the spectrum.

The ZN2 response to a 120 GeV/c positron beam, which hits the center of the calorimeter front face, is shown in Fig. 3.3. Since the positron beam has a small hadronic contamination, the ADC spectra have been fitted with the superposition of two functions (see Eq. 3.1).

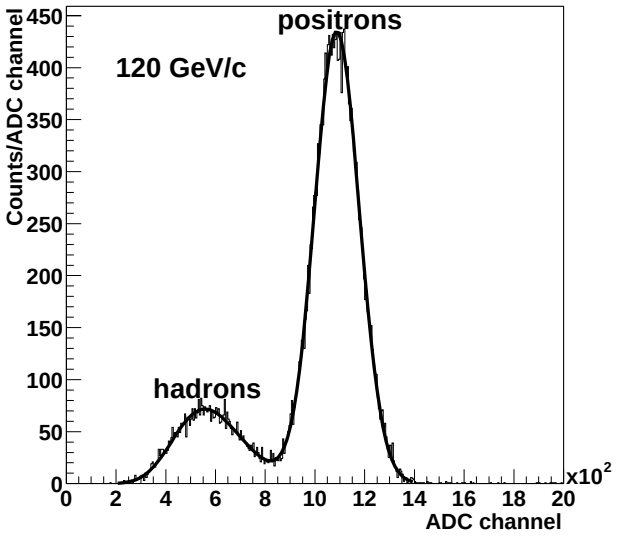

Fig. 3.3: *ZN2 response to a 120 GeV/c positron beam impinging on the centre of the calorimeter.*

3.3.2 Response to hadrons and electrons

The response of the ZN2 as a function of the beam energy has been studied for both hadron and positron beams.

A 1.5 x 0.5 cm^2 beam spot, centered on the front face of the calorimeter, has been selected by means of the MWPC.

The spectra have been fitted with the function given in Eq. 3.1. In Fig. 3.4 the value of the μ parameter is represented as a function of the energy.

The response to positrons shows a linear behaviour; a saturation effect can be seen at the two highest momenta. We attribute this fact to the lack of linearity of the Lecroy 2249W ADC module for signal amplitudes greater than 2 V.

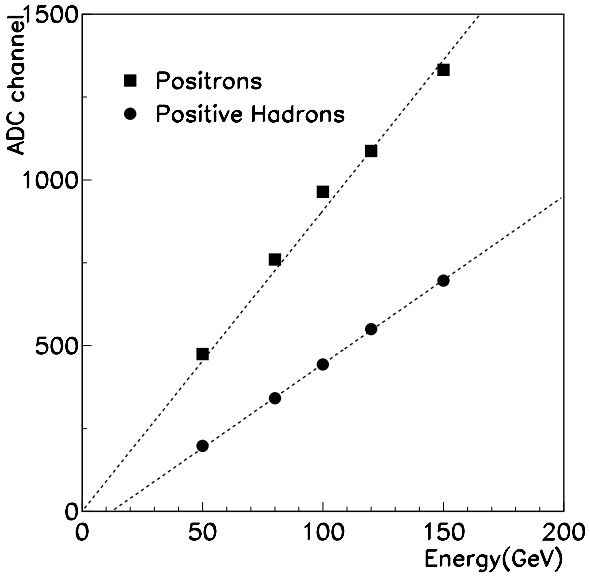

Fig. 3.4: *ZN2 response to positrons and positive hadrons as a function of beam energy. The error bars are not visible since they are smaller than the symbols.*

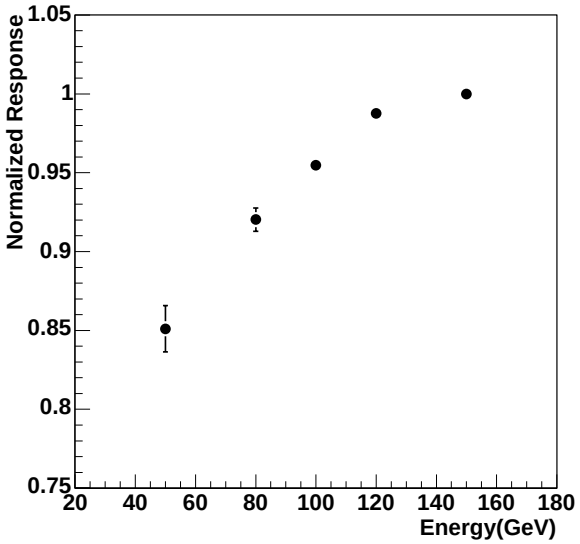

Fig. 3.5: *ZN2 normalized response to hadrons as a function of beam energy.*

On the contrary, the response to hadrons is not linear with respect to the beam energy. The effect is evident in Fig. 3.5, where the ADC response has been divided by the corresponding beam energy and the ratio has been normalized to the highest energy.

The conversion factor between the ADC channel and the number of photoelectrons has been obtained considering muon events, in which only few photoelectrons are produced. The light yield for hadron beams is of the order of 0.9 photoelectrons per GeV, while for positron beams is 2 photoelectrons per GeV.

3.3.3 e/π ratio

In Fig. 3.6 we present the ratio between the response of the calorimeter to positron and hadron beams (full circles) as a function of the beam energy. The e/π ratio ranges from 2.4 at 50 GeV/c to 1.9 at 150 GeV/c.

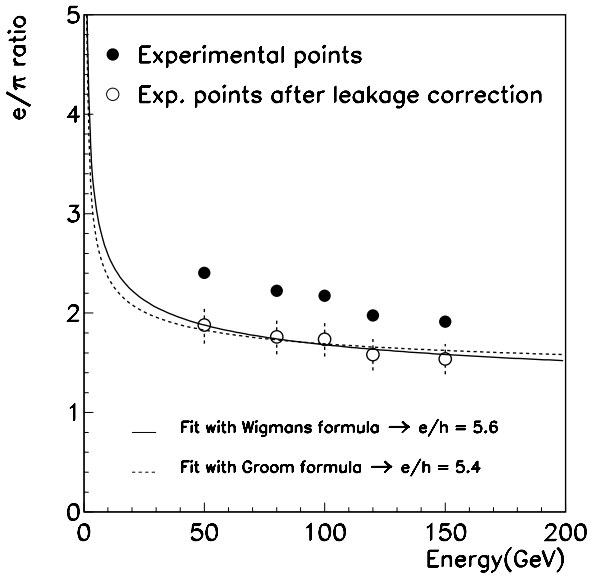

Fig. 3.6: *e/π ratio as a function of beam energy.*

The measured e/π response has been corrected for the lateral leakage (open circles) and then fitted using the function:

$$e/\pi = \frac{e/h}{1-(1-e/h)f_{\pi^0}(E)} \tag{3.3}$$

in order to extract the e/h value, namely the ratio of the calorimeter responses to the e.m. and non–e.m. components of the hadronic showers.

Assuming for $f_{\pi^0}(E)$ the Wigmans' parametrization[16]:

$$f_{\pi^0}(E) = 0.11 \cdot ln(E) \tag{3.4}$$

(with E in GeV) the fit gives e/h = 5.6 (solid line), while using the Groom's parametrization[17]:

$$f_{\pi^0}(E) = 1 - (E/E_0)^{m-1} \tag{3.5}$$

(with E_0 = 1 GeV and m = 0.85) we find e/h = 5.4 (dashed line).

We conclude that the ZN2 calorimeter is highly non–compensating (e/h $\geq$ 5). However, this fact will not lead to any detection problem in the ALICE experiment, since the spectator neutrons entering in the calorimeter will have the same energy as the beam nucleons. Therefore, ZN will be used as a multiplicity detector, measuring the number of spectator neutrons. Moreover the separator magnet D1 will remove all charged particles with momentum lower than 1.6 TeV and the background will be due only to γ's. Simulations [5] showed that this last contribution will be around 10% of the energy released in central events in the detector: this represents the most unfavorable situation (lowest value of the energy in the calorimeter).

3.3.4 Energy resolution

The energy resolution σ/E has been evaluated as the ratio σ_0/μ, where σ_0 is the width at $x = \mu$ and μ is the peak position (see Eq. 3.1 and 3.2). The contribution due to the σ_1 term to the width of the distribution is negligible. In fact the relationship between the FWHM of the ADC spectra and σ_0 is $FWHM \simeq 2.41 \cdot \sigma_0$ for all the energies, very close to that of a Gaussian distribution.

The results for both hadron and positron beams are plotted in Fig. 3.7 as a function of $1/\sqrt{E(GeV)}$.

The experimental points are fitted with the standard function:

$$\frac{\sigma}{E} = \frac{a}{\sqrt{E(GeV)}} \oplus b. \tag{3.6}$$

We get $a = (256.6 \pm 2.9)$ % $GeV^{1/2}$, $b = (10.3 \pm 0.6)$ % for positive hadrons and $a = (89.9 \pm 0.7)$ % $GeV^{1/2}$, $b = (0.0 \pm 2.9)$ % for positrons. By extrapolating the fit to 2.7 TeV, the energy of the spectator neutrons in Pb–Pb interactions at LHC, we obtain an energy resolution of $\sim$ 11.4 %, in agreement with the design performance, estimated through a Monte Carlo simulation based on the GEANT 3.21 code[5].

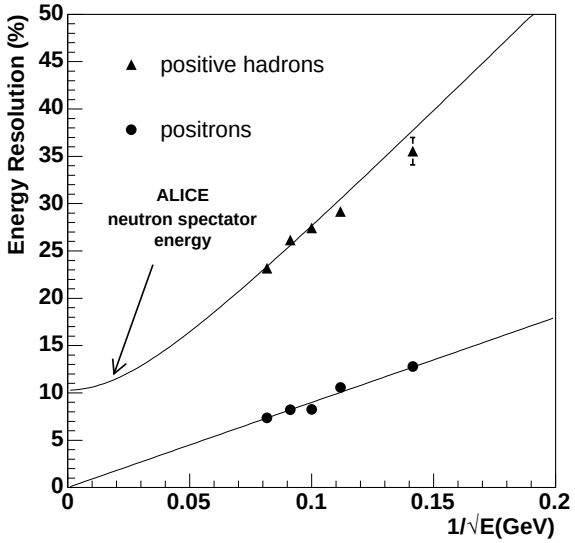

Fig. 3.7: *ZN2 energy resolution for positrons and positive hadrons as a function of* $1/\sqrt{E(GeV)}$.

3.3.5 Shower's transverse profile

The ZN is mainly sensitive to the central part of the shower, thanks to its principle of operation based on the detection of the Cherenkov light. In order to estimate the transverse size of the detectable hadronic shower we have studied the response of a single ZN2 tower as a function of the beam impact point on the front face of the calorimeter, as measured by means of the MWPC. In Fig. 3.8 the response of the single ZN2 tower T2 (full squares) is plotted as a function of the horizontal coordinate of the beam impact point, for a 100 GeV/c positive hadron beam. The solid line is a fit with an arctangent function to the experimental data.

The shower's transverse profile is obtained as the derivative of the data (open circles). The fit with the derivative of the arctangent function (dashed line) shows a width of the order of 8 mm.

Similar results have been obtained for the other ZN2 towers.

3.3.6 Uniformity of the response and fiber spacing

We have verified the uniformity of the calorimeter's response as a function of the beam impact point on the front face of the detector with respect to fibers' position. The fraction of light seen by the PMTc over the total signal

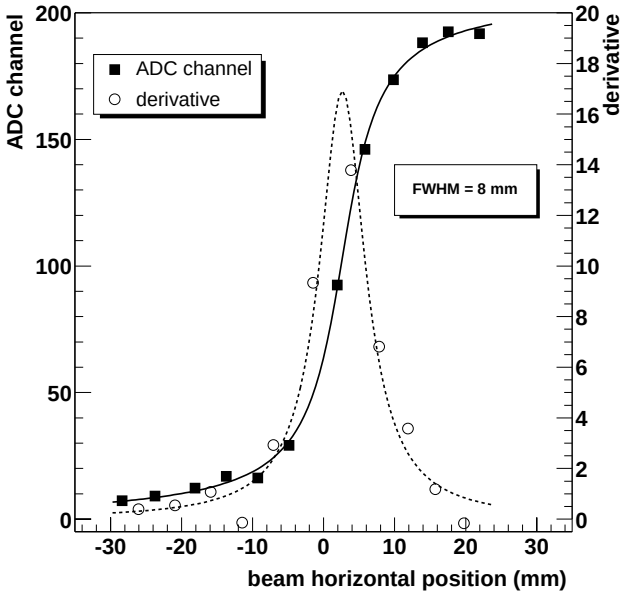

Fig. 3.8: *Response of a single ZN2 tower (full squares) as a function of the horizontal coordinate of the beam impact point, for a 100 GeV/c positive hadron beam. The detectable shower size is obtained as the derivative of the data (open circles).*

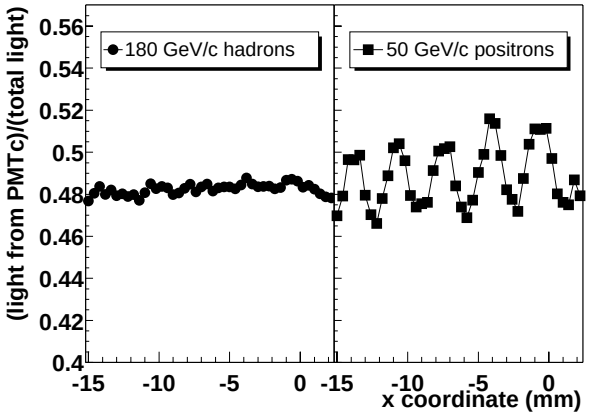

Fig. 3.9: *Fraction of light seen by the PMTc over the total signal collected by the five PMTs as a function of the horizontal coordinate of the beam impact point.*

collected by the five PMTs as a function of the horizontal coordinate of the beam impact point, measured by the MWPC, is plotted in Fig. 3.9. The results for 180 GeV/c hadrons and 50 GeV/c positrons are shown on the left and on the right side respectively. The plot refers to events selected within a horizontal window 1.2 mm high; in this way we consider particles impinging on a single fiber plane. While no appreciable structure is visible for the hadron beam, a clear oscillation of the order of 5 % can be seen for the positron beam. This is due to the sampling fraction; in fact the shower induced by the positrons has a detectable transverse size stongly peaked near the shower axis, which makes the detection sensitive to the distance between fibers going to the same PMT (3.2 mm).

The absence of any structure for hadron beams clearly shows that the ZN fiber spacing is adequate for hadronic calorimetry, as required by the ALICE experiment.

3.3.7 Spatial resolution

Thanks to the four tower segmentation, the ZN calorimeter can be considered as a rough position sensitive device. In the ALICE experiment this localizing capability will allow to reconstruct, event by event, the centroid of the spectators neutrons spot on the calorimeter front face. This measurement can be used to monitor the beam crossing angle at IP2 and to reconstruct the 1^{st}-order event plane, as shown in the chapter 6.

For the beam test analysis, the impact position of the beam on the detector has been estimated by means of the relations [18]:

$$x = \frac{\sum_{i=1}^{4} x_i w_i}{\sum_{i=1}^{4} w_i} \qquad y = \frac{\sum_{i=1}^{4} y_i w_i}{\sum_{i=1}^{4} w_i} \qquad with \qquad w_i = ADC_i^{\alpha} \tag{3.7}$$

where x_i and y_i are the coordinates of the centre of the $i-th$ tower and ADC_i is the digitized value of the corresponding PM signal. α is a free parameter introduced in order to get an accurate reconstructed impact coordinate. In fact, taking as weight simply the energy detected by each tower, the impact point is systematically shifted towards the center of the tower hit by the particle[37]. The value α=0.5 has been obtained from simulation for 100 GeV/c positive hadrons, considering only particles hitting the device in a region of 8 mm radius around the ZN2 centre: the position reconstruction is accurate essentially near the intersection of the four towers. In the analysis we imposed the same event selection.

In Fig. 3.10 the difference between the impact coordinate reconstructed by the ZN2 and the one measured by the MWPC is plotted for the 100 GeV/c positive hadron beam.

The width of the distribution is $\sim$ 3 mm, demonstrating that a good reconstruction of the impact point of the spectator neutron spot on the ZN front face can be achieved, despite the low granularity of the calorimeter.

This feature will surely be used in the ALICE experiment, since the expected transverse spread of the spectator neutron's spot on the front face of ZN is quite small (6 x 6 mm^2 at 1 σ level)[5].

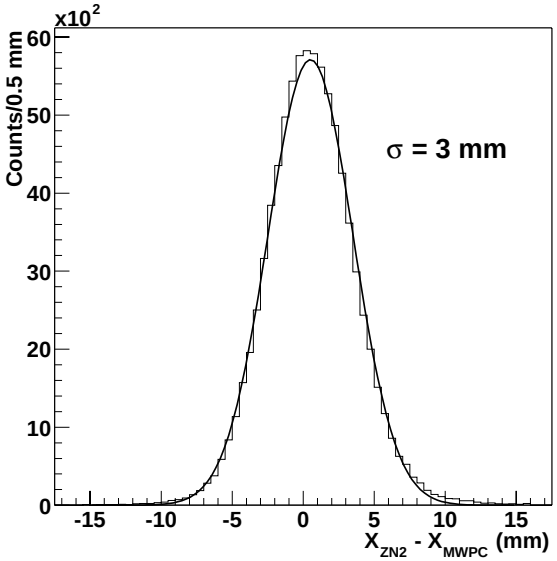

Fig. 3.10: *Spatial resolution of ZN2 calorimeter for a 100 GeV/c positive hadron beam. Only events in a central region of about 8 mm radius around the centre have been taken into account in the analysis.*

Chapter 4

Test of the ZP1 calorimeter with hadron and electron beams

4.1 Introduction

The performance of the first Proton Calorimeter (ZP1) has been studied at the H6 beam line of the CERN SPS in July 2004. The detector has been irradiated with secondary and tertiary hadron and electron beam of momentum ranging from 50 to 200 GeV/c, the latter being the highest beam energy available on this beam line.

The test allowed to investigate the calorimeter response and energy resolution in the considered range of beam energies. Also the e/h ratio has been determined. Moreover we could study the uniformity of the response, the sampling fraction and the transverse profile of the hadronic and electromagnetic shower.

Finally the differences in the calorimeter responses to pions and protons have also been observed taking into account that the positive hadron beams had a not negligible proton contamination [19, 20, 21].

4.2 The test beam experimental setup

A schematic layout of the test set-up is shown in Fig. 4.1. A plastic scintillator telescope S1-S4 provided the trigger. A MWPC has been installed in front of the calorimeter to localize the incident beam particles on the ZP front face. Two plastic scintillators MU1 and MU2, placed beyond an iron wall, allowed to detect muons. To be able to scan the whole calorimeter front face, the calorimeter has been mounted together with the MWPC on a movable platform.

A Lecroy 2249W ADC module has been employed to digitize the analogical signals from the PMTs of the calorimeter.

The PMTs high voltages were equalized at the beginning of the test by sending the beam in the centre of each tower and of the calorimeter front face. A fine tuning of the ADC signals for each channel was made offline to compensate possible small differences.

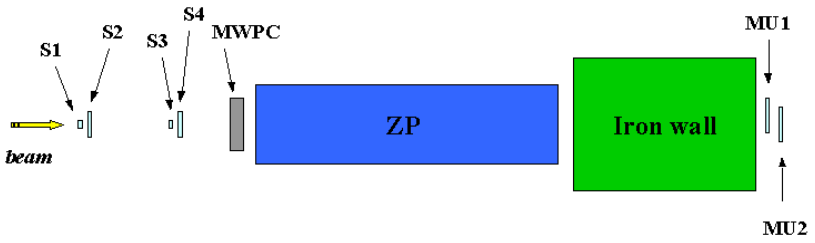

Fig. 4.1: *Schematic view of the experimental set-up.*

4.3 Experimental results

4.3.1 Response to hadrons and electrons

Fig. 4.2 shows an example of ADC spectrum obtained as the sum of the signals from the 5 PMTs when a 120 GeV/c pion beam hits the centre of the calorimeter's front face. In the Fig. 4.3, instead, the calorimeter's response to a 120 GeV/c electron beam can be seen, with a clear hadronic contamination.

The non Gaussian shape of the calorimeter's response to hadrons has already been discussed for the ZN calorimeter (see Sec. 3.3.1). In order to take into account the hadron spectra asymmetry, the data have been fitted with the gaussian-like function described by the Eq.s (3.1) and (3.2).

The muons deposite a very low amount of energy in the calorimeters, producing a very low signal. Selecting muons events by means of MU1 and

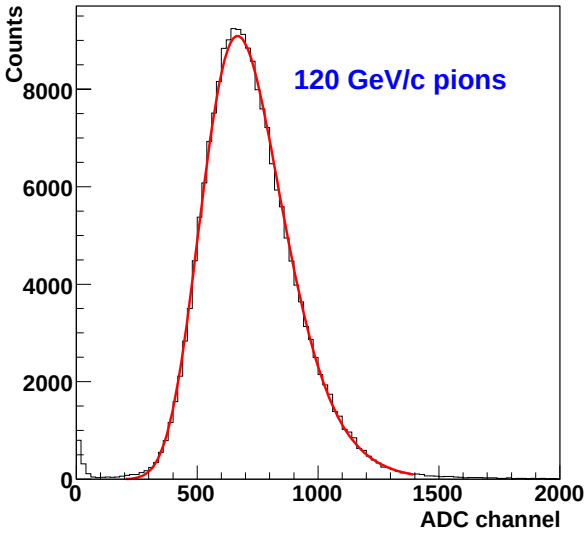

Fig. 4.2: *ZP response to 120 GeV/c pion beam.*

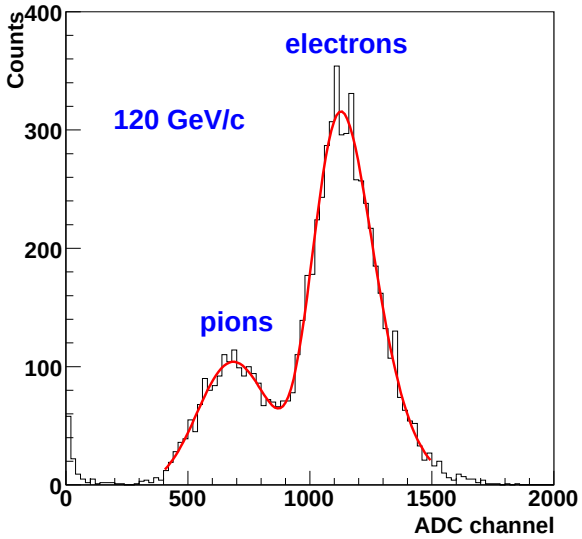

Fig. 4.3: *ZP response to 120 GeV/c electron beam. A clear hadronic contamination can be seen.*

MU2 scintillators, we could determine the amplitude of the single photoelectron peak, and therefore the conversion factor between ADC channels and photoelectrons. We obtained a light yield of about 1.1 phe/Gev for hadrons and 1.8 phe/GeV for electrons, for an 120 GeV/c beam momentum.

During the test the ZP1 detector response has been studied as a function of the beam energy both for hadron and electrons. In Fig. 4.4 the value of the μ parameter (Eq. (3.1)) is plotted as a function of the energy.

Fig. 4.5 and 4.6, respectively for hadrons and electrons, show, as a function of the beam energy, the ratio between the ADC response and the corresponding beam energy, normalized to 120 Gev/c. ZP response to electrons is linear within 3%, while the response to hadrons is not linear. In fact, being the calorimeter not compensating, it is sensitive to the electromagnetic component of the hadronic shower, which increases with the beam energy. However, in the ALICE experiment, the ZP will measure the number of spectator protons which all have the same fixed energy, as the beam nucleons. The charged particles produced at IP will be bent by D1 separator magnet outside ZP acceptance and the energy due to neutral particles hitting the calorimeter is found to be negligible with respect to the energy carried by spectator protons. Therefore, as already observed for the ZN detector, the fact that the calorimeter is not compensating will not create any problem in ALICE.

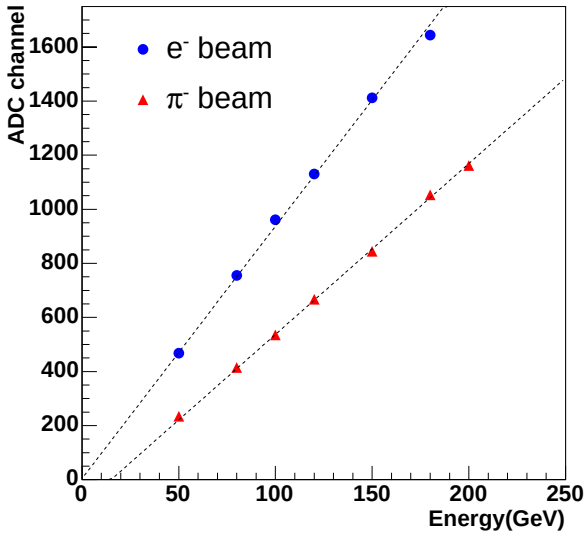

Fig. 4.4: *ZP response to hadrons and electrons as a function of the beam energy. The error bars are not visible since they are smaller than the symbols.*

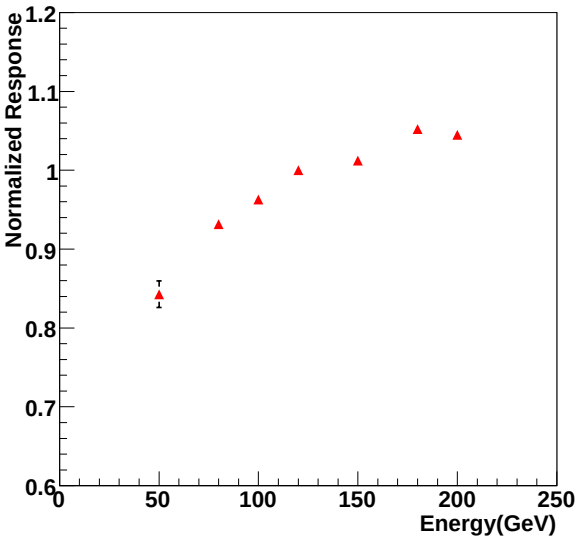

Fig. 4.5: *ZP normalised response to hadrons as a function of the beam energy.*

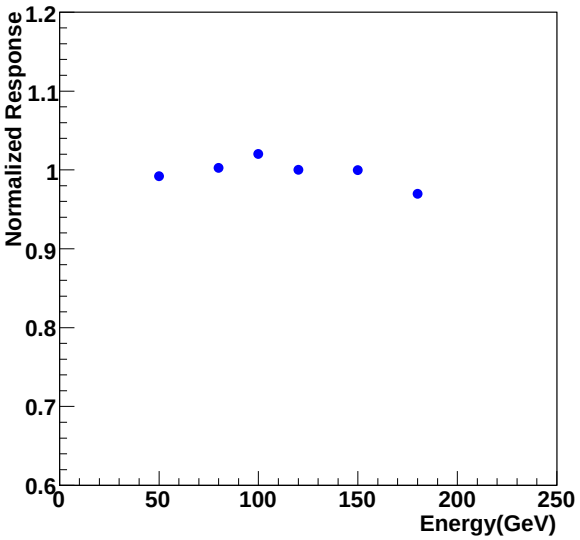

Fig. 4.6: *ZP normalised response to electrons as a function of the beam energy.*

4.3.2 e/π ratio

The measured e/π ratio, i.e. the ratio between the calorimeter's responses to electrons and pions is represented in Fig. 4.7 as a function of the beam energy. The e/π ratio depends on the beam energy and ranges from $\sim$ 2.0 at 50 GeV/c to $\sim$ 1.6 at 180 GeV/c.

The electromagnetic shower is completely contained in the calorimeter, while for the hadronic shower we estimated, from the simulation, a lateral leakage of about 15%. Taking into account this correction factor for the experimental data, we could evaluate e/h, the ratio of the calorimeter's responses to the e.m. and non-e.m. components of the hadronic shower, by fitting the corrected data with the function described in the Eq. (3.3).

According to the fact that the calorimeter is not compensating, we found an e/h value of 3.0, using for the π^0 fraction the Wigmans parametrisation [16] (Eq. (3.4)), and a value of 2.9, using the Groom's parametrization [17] (Eq. (3.5)).

The ZP e/h value results lower than that of the ZN detector($e/h \sim 5.5$). In fact since the ZP filling ratio (1/65) is smaller than the ZN one (1/22), in the proton calorimeter the shower electrons suffer a greater absorption in the passive material.

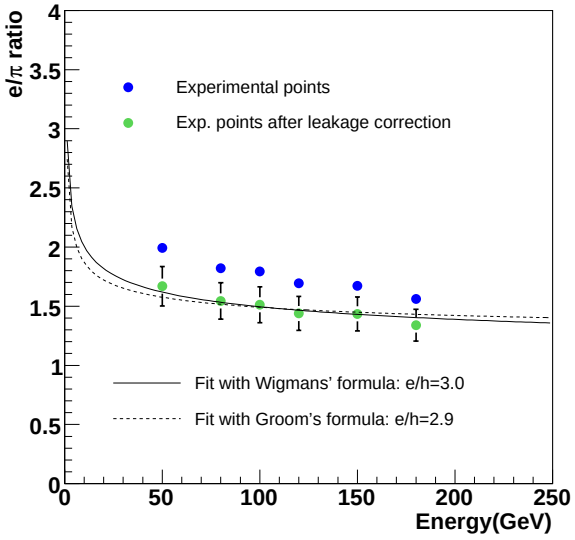

Fig. 4.7: *e/π ratio versus beam energy.*

4.3.3 Energy resolution

The test allowed to measure the calorimeter's energy resolution as a function of the energy, for both hadron and electron beams; the results are shown in Figure 4.8.

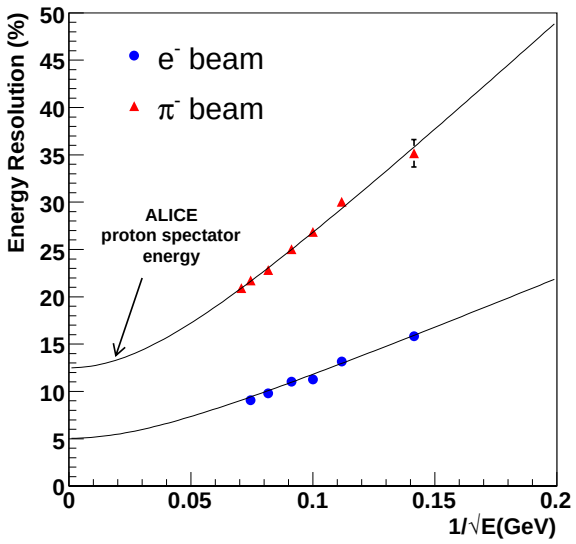

Fig. 4.8: *ZP energy resolution as a function of* $1/\sqrt{E(GeV)}$.

The energy resolution σ/E has been calculated as the ratio σ_0/μ (see Eq.s (3.1) and (3.2)), as for the ZN case.

The data have been fitted with the usual function of the Eq. (3.6).

We obtained $a = (237. \pm 2.)$ % $GeV^{1/2}$, $b = (12.5 \pm 0.2)$ % for pions and $a = (106.8 \pm 0.9)$ % $GeV^{1/2}$, $b = (5. \pm 0.3)$ % for electrons. By making an extrapolation to the ALICE single spectator proton energy (2.76 TeV) we find a resolution value of about 13%, in agreement with the ALICE experiment requirements [5].

4.3.4 Response's uniformity

With a 120 GeV/c hadron beam we have performed a complete horizontal scanning with the vertical beam coordinate fixed at the centre of the calorimeter front face, in order to study the uniformity of the response. In Fig. 4.9 the responses of the four adjacent towers as a function of the beam impact horizontal coordinate, are represented. It is interesting to note that

only the towers 3 and 4 can see the quartz fiber periodicity. This is due to the fact that the sampling fraction is slightly higher when the beam particles hit the calorimeter in a fiber plane than when they hit the absorber [22]. The vertical beam position was not the same during the whole scan, as can be seen in Fig. 4.10, where we plot the vertical coordinate of the beam particles detected by the MWPC. This beam displacement is due to the fact that the complete scanning was done in two different periods and we couldn't reproduce exactly the same beam conditions.

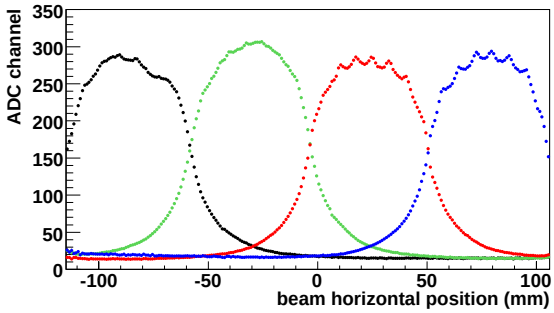

Fig. 4.9: *Signals of the four ZP towers T1, T2, T3, T4 (from left to right) as a function of the beam impact horizontal coordinate.*

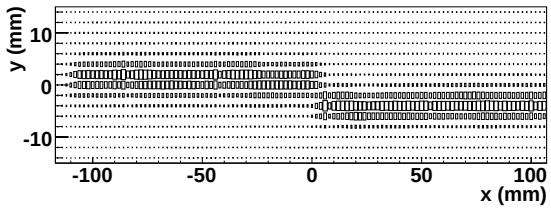

Fig. 4.10: *Beam impact point on the calorimeter front face defined using the MWPC.*

We can see that the sampling fraction is slightly dependent on the particle impact point, even if we look at the ratio between the signal of the common photomultiplier PMTc and the total signal versus the horizontal coordinate of the beam impact point (Fig. 4.11). In this study we considered events within a thin window centered on a single fiber plane. It possible to see the periodicity of fibers going to the same PMT (8 mm). For positron beams we observe clear oscillations, of the order of $\sim 15\%$, due to the electromagnetic shower, strongly peaked near its axis, which makes the detection sensitive to the distance between fibers going to the same PMT. Less important variations

($\sim$ 2.5%) for hadrons induced signals show that the ZP fiber spacing is adequate for hadronic calorimetry.

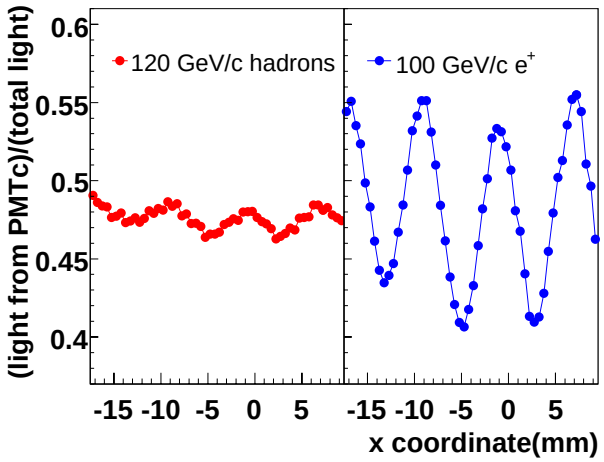

Fig. 4.11: *Signal of the PMTc over the calorimeter's total signal as a function of the particle impact horizontal coordinate.*

4.3.5 Detectable shower's transverse profile

Taking the derivative of a single ZP tower response as a function of the beam impact point in a boundary region between two towers, we can estimate the transverse size of the detectable shower.

The FWHM of the derivative is $\sim$ 13 mm for a scan performed with a 120 GeV/c positive hadron beam (Fig. 4.12), while an analogous study performed with a 100 GeV/c positron beam(Fig. 4.13) gives a value of $\sim$ 6 mm for the electromagnetic shower.

4.3.6 Difference in the response to p and π

During the test, for three beam momenta (100, 120, 150 GeV/c) the calorimeter behaviour has been investigated with both negative and positive hadron secondary beams.

While the negative beams are composed almost enterely by pions, the positive beams are a mixture of pions and protons. As can be seen in Table 4.1, the fraction of pions depends on the beam energy and on the selected production angle on the target [23]. The plot in Fig. 4.14 shows that, being the fraction of pions known, it is possible to separate the π^+ and proton

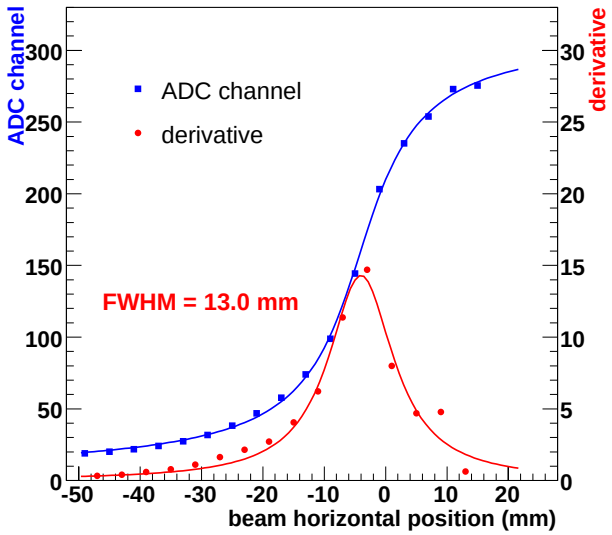

Fig. 4.12: *Response of a single ZP tower (blue square) as a function of horizontal beam impact point, for a 120 Gev/c positive hadron beam. The derivative of the data (red circles) gives an estimation of the detectable shower size.*

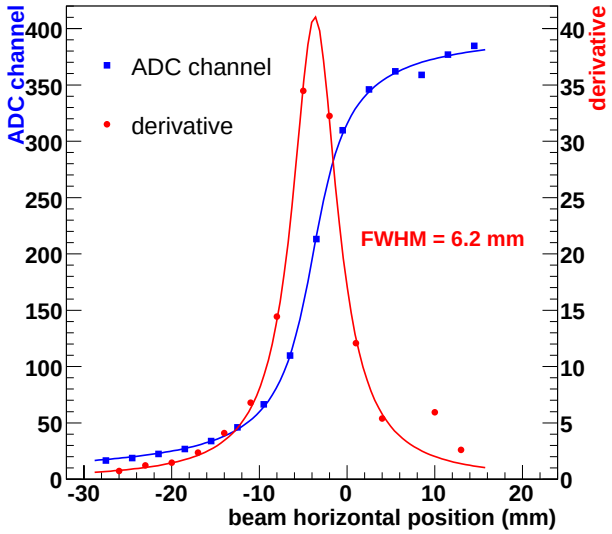

Fig. 4.13: *Response of a single ZP tower (blue square) as a function of horizontal beam impact point, for a 100 Gev/c positron beam. The derivative of the data (red circles) gives an estimation of the detectable shower size.*

Beam momentum (GeV/c)	Production angle ($mrad$)	Fraction of π
100	-5.46	61%
120	-0.2	61%
150	5.	31%

Tab. 4.1: *Pions' fraction in positive beams, for the investigated beam momenta (CERN SPS data).*

contributions in the positive beam spectra, assuming that the shape of π^+ spectra is equal to that of π^-, scaled by a proper factor. Subtracting from the positive hadron spectrum the π^+ contribution, we could obtain the calorimeter's response to protons. An example, for the 120 GeV/c momentum, is shown in Fig. 4.15.

In Fig. 4.16, for both pions and protons, we plot the normalized response, i.e. the ratio between the ADC response and the corresponding beam energy, normalized to the 150 Gev/c pion beam. From this plot the ZP response to protons is found to be, on average, $\sim 9\%$ lower than the response to pions of the same energy. In fact, due to the baryon number conservation law, the proton interactions have a smaller fraction of energy going into π^0's, and therefore into the e.m. component of the shower, than pion interactions [24]. The ZP calorimeter, being non-compensating, is sensitive to this different e.m. component in the shower development.

Finally, in Fig. 4.17 we show the calorimeter resolution for pions and protons as a function of the beam energy; it can be noticed that the energy resolution for protons is better than for pions, despite the fact that the ZP response to protons is lower than the response to pions. This effect can be explained by the large non-Gaussian energy fluctuations of the e.m. component of the pion shower, caused by the leading neutral pions produced by the charge exchange mechanism [21].

The data relative to proton resolution have been fitted with the function described in Eq. (3.6). For the fit parameters we get $a = (185.\pm 4.)$ % $GeV^{1/2}$ and $b = (14.3 \pm 0.4)$ % for protons, while the curve describing the points relative to pion resolution is the one shown in Fig. 4.8.

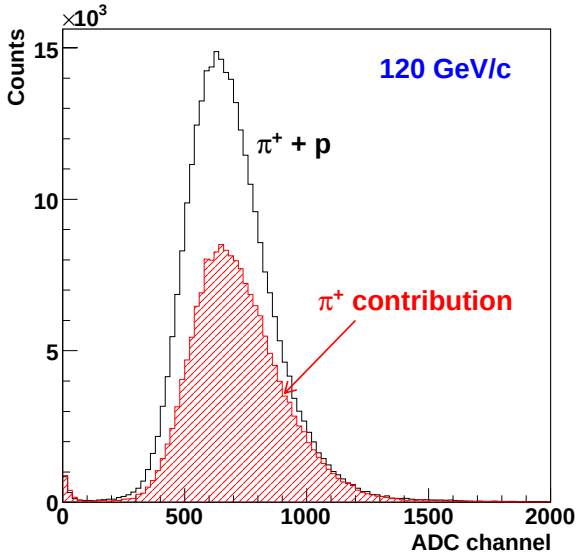

Fig. 4.14: *Calorimeter's response to a 120 GeV/c positive hadron beam: the π^+'s contribution can be seen.*

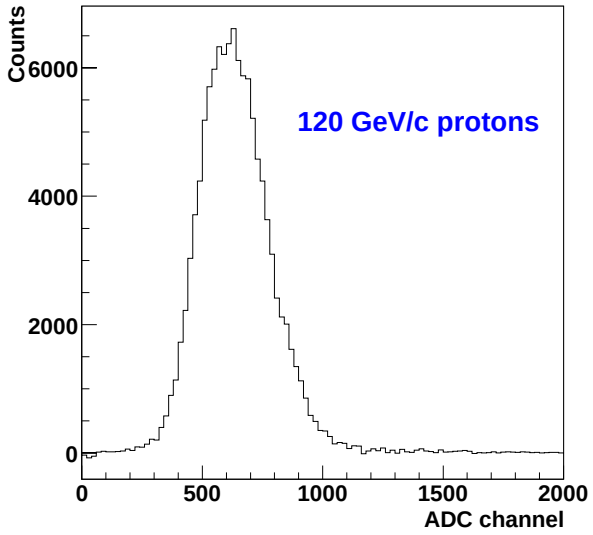

Fig. 4.15: *ZP response to 120 GeV/c protons.*

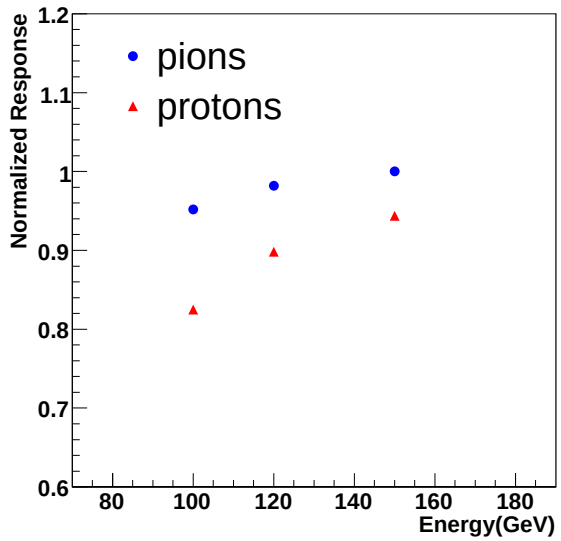

Fig. 4.16: *Normalized ZP response to pions and protons.*

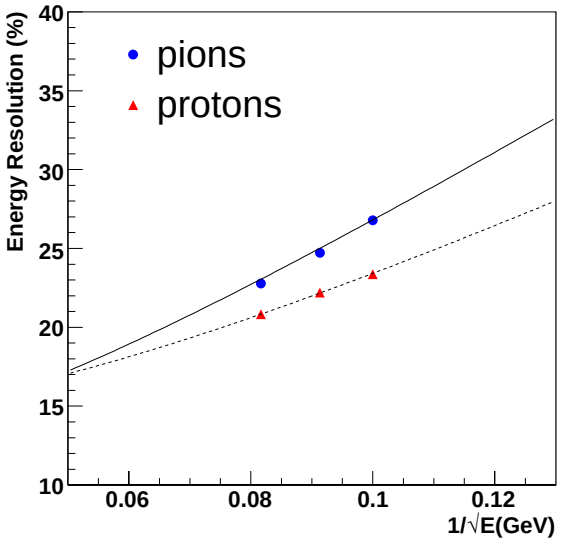

Fig. 4.17: *ZP resolution for pions and protons as a function of* $1/\sqrt{E(GeV)}$.

Chapter 5

Test of the ZN2 calorimeter with an ^{115}In beam at 158 AGeV/c

5.1 Introduction

The second neutron calorimeter (ZN2) was tested at the H8 beam line of the CERN SPS in autumn 2003 with an ^{115}In beam at 158 AGeV/c. This test was very important because it allowed to check the response of the calorimeter to the ion beam, whose energy ($\sim$18.2 TeV) is equivalent to that carried to the neutron calorimeter by 6-7 spectator neutrons, that are expected in a central Pb-Pb collision at the LHC.

Moreover inserting several targets on the beam, we could measure the spectator nucleons energy and so we could verify the linearity of the calorimeter response with the number of spectator nucleons entering its front face, as described in the following.

In addition, a more detailed analysis of the test in the frame of the Glauber theory of the nucleus-nucleus collisions has been performed. Since this work is essentially based on a linear relation between the number of spectator and participant nucleons and the energy experimentally detected in the Zero Degree Calorimeters, it allows a further check of the calorimeter response linearity.

5.2 Test experimental setup

During the test, the calorimeter was put on a platform which could move on a plane normal to the beam.

As shown in fig. 5.1, a system of two 2 mm thick scintillators (S_1, S_2) provided the trigger.

A further scintillator (S_3), 2 mm thick, with a transverse section of 70 x 100 mm^2 was put in front of the calorimeter and it was used to select the In ions, which did not interact in the target or in the other materials upstream of the calorimeter.

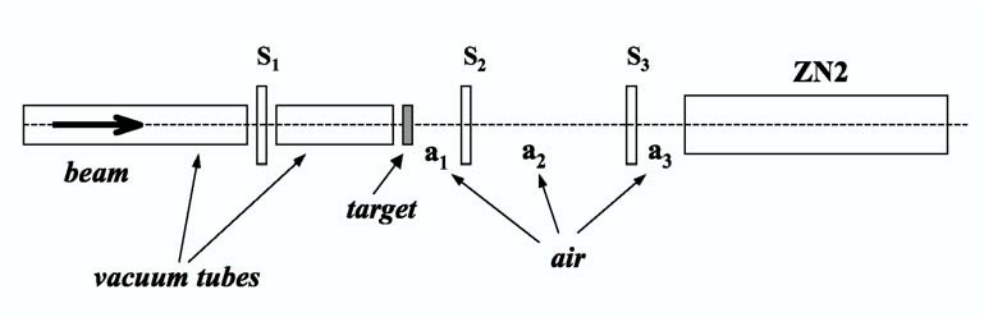

Fig. 5.1: ^{115}*In beam test experimental setup.*

The beam was sent on various targets placed at 10.71 m from the calorimeter. The scintillators S_2 and S_3 lay between the target and the detector in a space filled with air. In Tab. 5.1 the density, the thickness and the number of interaction lengths for all the used targets are reported. The values of the same parameters for the materials crossed by the beam between the target and the detector are reported in Tab.5.2.

material	density (g/cm^3)	thickness (mm)	thickness (λ)
^{119}Sn	7.31	3.4	0.0544
^{63}Cu	8.96	4.5	0.132
^{27}Al	2.70	14.8	0.234
^{12}C	1.70	17.8	0.318

Tab. 5.1: *Parameters for the various targets used in the test.*

The PM output signals were readout by a LeCroy 2249W ADC; the CAMAC bus was connected to the PCI of the DAQ computer by means of the

	material	density (g/cm^3)	thickness (mm)	thickness (λ)
a_1	air	0.0012	7319	0.07984
a_2	air	"	2878	0.03139
a_3	air	"	509	0.00555
s_2	scint.	1.032	2	0.02294
s_3	scint.	"	2	0.02294

Tab. 5.2: *Parameters for the materials crossed by the In beam between the target and the calorimeter.*

MXI-3 Interface developed by National Instrument. The data acquisition software DATE [25] was used.

At the beginning of the test the ZN towers have been equalized. First of all, the In beam was sent to the centre of each tower; then, the high voltage has been tuned in order to obtain the same mean value of the ADC spectrum, after pedestal subtraction. Moreover, since the common photomultiplier is connected to a number of fibers four times larger than the other photodetectors, the PMTc high voltage has been set in order to get a response equal to the sum of the signals of the others four PMTs, when the beam hits the center of the calorimeter front face.

A fine tuning of the ADC signals for each channel has been then performed in the offline analysis.

5.3 Beam test Monte Carlo simulation

A Monte Carlo simulation of the beam test has been performed using the GEANT 3.21 code [26].

The nucleus-nucleus interaction is simulated using the Fritiof code [27]. The produced particles are then stored into the GEANT stack, while the spectator nucleons are passed to a routine which put toghether protons and neutrons to eventually form nuclear fragments.

To simulate the detector response, the Cerenkov light production and transport along the fibres are evaluated using a separate program, which produces the distribution of Cerenkov light yield in optical fibres as a function of particle velocity, distance from the fibre axis and incident angle of the particle trajectory with respect to the fibre's axis. The results produced are written as tables in ASCII format. The data tables take into account the numerical aperture of the fibres, the attenuation in the fibres and the quantum efficiency of the photocatode of the photomultipliers. A shower

particle is tracked by GEANT in the calorimeter absorber until it crosses a fibre, then the photon yield is directly read from the tables [7].

In the following the experimental energy resolution has been evaluated and compared to the results of the simulation. A comparison between the experimental and the simulated data has also been done for the study of the linearity of the calorimeter's response as a function of the number of spectator nucleons.

5.4 Energy resolution

The response of the ZN calorimeter to In beam, which doesn't interact in any material along the beam line, is shown in fig. 5.2.

The slightly non-gaussian shape is due to the fact that the calorimeter is not compensated, but, as we discussed in Chap.3, this fact does not cause any problems for using the detector in ALICE.

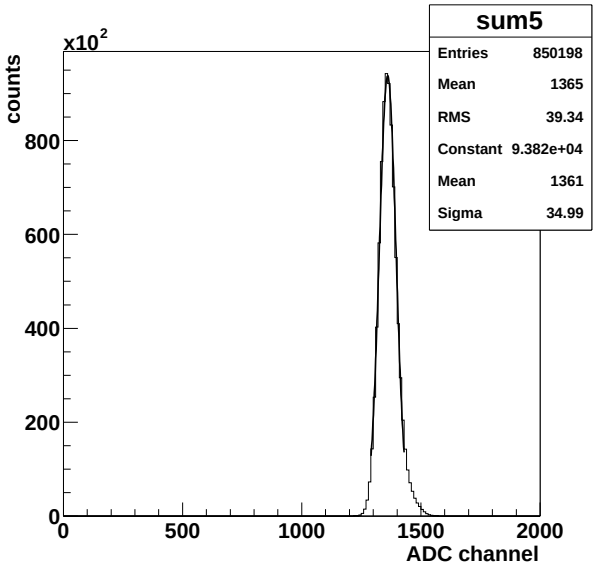

Fig. 5.2: *Response of the calorimeter to the In beam.*

The energy resolution, 2.6±0.05%, was determined as the ratio $R = \sigma/\mu$, σ being the width and μ the mean value of the gaussian fit of the spectrum.

Assuming that the shower induced by the ^{115}In ion is equivalent to 115 independent showers each one induced by a 158 GeV/c nucleon, we could estimate the resolution of the calorimeter dividing the value of the resolution

for 150 GeV/c pions, measured from a previous test (see Chap.3), by the square root of the number of ^{115}In nucleons:

$$\frac{\sigma_E}{E} = \frac{\sqrt{N\sigma_n^2}}{NE_n} = \frac{\sigma_n}{\sqrt{N}E_n} \approx 2\%$$

where N=115 and $\frac{\sigma_n}{E_n}|_{E_n=150} = (23.17 \pm 0.06)\%$ comes from beam test results.

Then the expected resolution in the independent nucleons model would be $\simeq 2\%$, not too far from the measured value. The resolution obtained with the simulation program is $\simeq 3.3\%$.

5.5 Linearity as a function of spectator number

In the ALICE experiment the ZDCs will provide the centrality of the ion collisions by measuring the number of spectator nucleons; therefore it is very important to check that the calorimeter response is linear as a function of the number of nucleons entering the detector.

To prove this linearity, the ^{115}In beam was sent on various targets: ^{12}C, ^{27}Al, ^{63}Cu, ^{119}Sn with mass number smaller or almost equal to the projectile one.

If the colliding nuclei are approximated to rigid spheres with a uniform nucleon distribution, the number of spectator nucleons coming out from central collisions (*impact parameter b=0*) is given by (see Appendix A):

$$N_{spec} = A\left[\left(\frac{B}{A}\right)^{\frac{2}{3}} - 1\right]^{\frac{3}{2}} \tag{5.1}$$

where B is the projectile nucleus and A is the target one[3]. The numbers of spectators in central collisions, as calculated by the previous formula, are summarized in Table 5.3 for all target nuclei used in the test.

Since, during the test, the ZDC has been placed on the beam axis, all the spectators nucleons hit its front face and release their energy by producing a particle shower. In addition, also some participant nucleons and produced particles are emitted within the angular acceptance of the calorimeter, contributing to the energy measured in the detector (E_{ZDC}).

Target	^{119}Sn	^{63}Cu	^{27}Al	^{12}C	*void*
N_{spec}	0	21.8	56	79	115

Tab. 5.3: *The number of spectator nucleons, when $b = 0$, for all the used targets.*

Therefore, for each value of the impact parameter b and in particular for $b = 0$, we can express E_{ZDC} as a sum of two terms, one proportional to the number of spectator N_S, the other proportional to the participant nucleons N_P:

$$< E_{ZDC}(b) >= 158 \times N_S(b) + \alpha N_P(b) \tag{5.2}$$

where 158 AGeV is the beam energy per nucleon and α is the equivalent energy per participant[28].

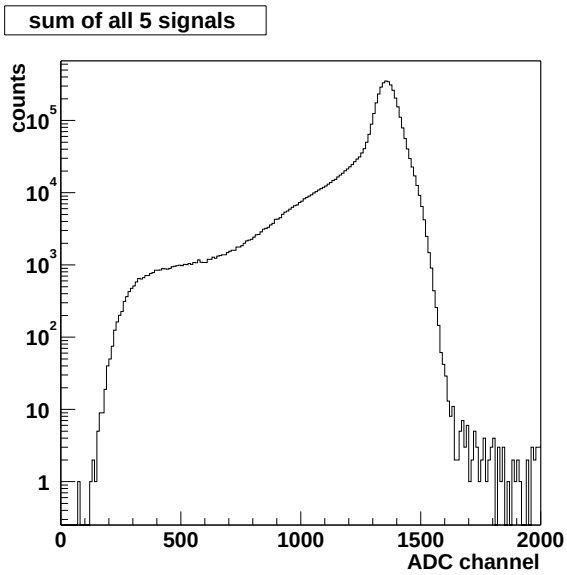

Fig. 5.3: *ADC spectrum corresponding to In-Sn collisions.*

5.5.1 Interacting In ions selection

Fig. 5.3 shows an example of ADC spectrum obtained from the collisions between ^{115}In ions and ^{119}Sn nuclei. A peak corresponding to 18.17 TeV indium ions entering the ZN without interacting along the beam line is clearly seen. The events on the left of the In peak are produced by indium ions interacting in the target, in the air or in the scintillators upstream of the calorimeter and the low-energy end point of the ADC spectrum corresponds to the most central collisions.

Since in the analysis we were interested in the minimum bias spectrum for all the used targets, we had to remove from the spectrum shown in Fig. 5.3 the In ions which did not interact in the target or in any material upstream of the calorimeter. The non-interacting In ions have been selected using the ADC spectrum of the scintillator S3 placed in front of ZN (Fig. 5.4). In order to reject the events in the peak on the right, this peak has been fitted with a gaussian function and a sharp cut has been imposed at 3σ from the mean value. The calorimeter ADC spectrum corresponding to In-Sn collisions and the empty target spectrum, both after the removal of non-interacting ions, are shown in Fig. 5.5.

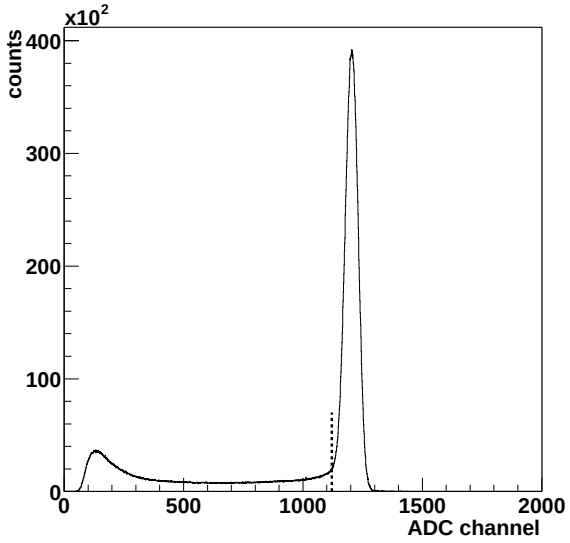

Fig. 5.4: *ADC spectrum of S3 scintillator for In-Sn runs.*

5.5.2 Empty target subtraction

As can be seen in Fig. 5.1, the In beam after the target can interact with the scintillators S2 and S3 and on the air surrounding them. In order to obtain a clean sample of minimum bias events the contribution of these interactions has to be evaluated and subtracted, although the effect is important only for peripheral events. For this reason special "empty target" runs have been performed during the data taking, moving the target holder away from the beam line. In these runs the resulting E_{ZDC} spectrum contains both the non interacting In beam and the In ions which have interacted with the air or the scintillators.

The peak of the non interacting ions has been removed with the cut on the ADC spectrum of the scintillator S3 as in the case of full target runs.

Then the empty-target spectrum has been normalized to the total number of incident ions for each full-target sample. More precisely the normalisation factor K, is obtained as the ratio between the events in the full-target spectrum and the events in the empty-target spectrum, without rejecting the contribution of those ions which have not taken part in the collisions.

Moreover a correction factor for the normalisation of empty target contribution has to be introduced to take into account that the In beam in empty-target runs has a greater probability of interacting with the air and the scintillators lying on the beam line than in full-target [28]. We have calculated this factor, called F/E, by means of a simple model based on the interaction probability. We consider the target thickness, the two scintillators and the surrounding air from the target to the calorimeter front face(see Fig. 5.1). The Tab.5.2 reports the useful parameters for each material crossed by the beam after the target. The data for the target used in the test are reported in Tab.5.1.

For each generic thickness x encouterd by the beam, we indicate the survival probability in x as:

$$S_x = e^{-\frac{x}{\lambda}} \tag{5.3}$$

where λ is obviously the In ion interaction length in the considered material.

Hence the interaction probability in x will be:

$$I_x = 1 - S_x = 1 - e^{-\frac{x}{\lambda}} \tag{5.4}$$

Using these definitions it is possible to calculate the probability F of In ions interaction with the air and the scintillators in full-target runs:

$$F = S_t(I_{a_1} + S_{a_1}(I_{s_2} + S_{s_2}(I_{a_2} + S_{a_2}(I_{s_3} + S_{s_3}I_{a_3})))) \tag{5.5}$$

where t, a_i and s_i are respectively the thickness of the target, the air and the scintillators crossed by the beam (Fig. 5.1).

Similarly, if we neglect the target thickness t occupied by the air when the target is removed from the beam line, the probability E of In ions interaction with the air and the scintillators in empty-target runs is given by the relation:

$$E = I_{a_1} + S_{a_1}(I_{s_2} + S_{s_2}(I_{a_2} + S_{a_2}(I_{s_3} + S_{s_3}I_{a_3}))). \tag{5.6}$$

Therefore the normalisation correction factor F/E can now be evaluated as:

$$\frac{F}{E} = S_t = e^{-\frac{t}{\lambda_{In-target}}}. \tag{5.7}$$

This factor relies on the In ions survival probability in the target. The values for this correction factor are shown, for the various used targets, in Table 5.4, where it is clear that the correction is important for the thickest targets.

Target	^{119}Sn	^{63}Cu	^{27}Al	^{12}C
F/E	0.95	0.88	0.79	0.73

Tab. 5.4: *Correction factors for the various target used in the test.*

The error on the F/E ratio is of the order of 2% and it is due to the fluctuations of the geometrical nucleus-nucleus cross-section, from which the interaction length values, used in the calculation of the normalisation correction factor, depend.

In Fig. 5.5 the spectrum relative to the Sn target is shown together the normalized spectrum corresponding to empty target.

Finally the empty target E_{ZDC} spectrum is subtracted from the full target one, according to:

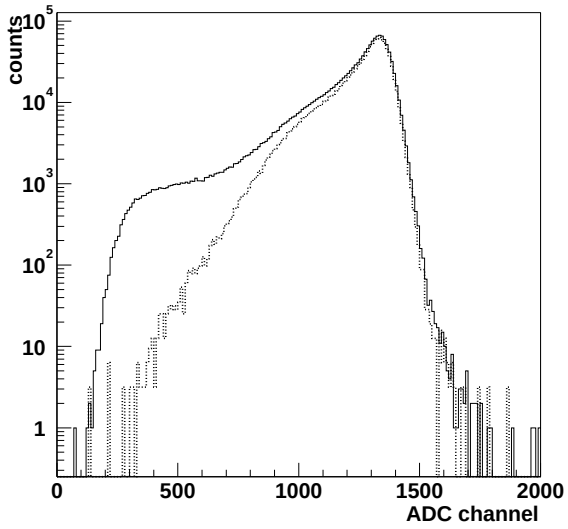

Fig. 5.5: *ADC spectrum corresponding to In-Sn collisions (full line) with the normalized empty target spectrum (dotted line) superimposed.*

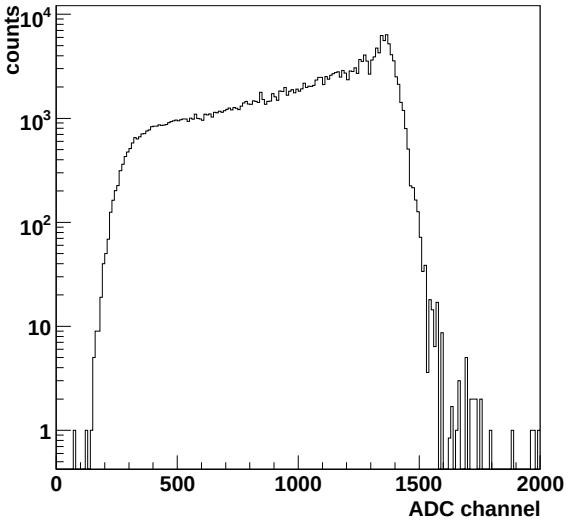

Fig. 5.6: *ADC spectrum for In-Sn collisions after the normalized empty target spectrum subtraction.*

$$\frac{dN^{MB}}{dE_{ZDC}} = \frac{dN^{MB}}{dE_{ZDC}}(FullT.) - \frac{dN^{MB}}{dE_{ZDC}}(EmptyT.) \times K \times \frac{F}{E} \tag{5.8}$$

where $\frac{dN^{MB}}{dE_{ZDC}}$ is the E_{ZDC} spectrum after the empty target subtraction; $\frac{dN^{MB}}{dE_{ZDC}}(FullT.)$ is the E_{ZDC} spectrum in full target run, $\frac{dN^{MB}}{dE_{ZDC}}(EmptyT.)$ is the E_{ZDC} spectrum in the empty target sample and $K \times \frac{F}{E}$ is the whole normalisation factor.

The result of the procedure of empty target spectrum normalisation and subtraction is shown in Fig.5.6 for the In-Sn collisions ADC spectrum.

5.5.3 Spectrum end-point determination

The minimum bias spectrum can be thought as the sum of an infinite number of gaussian functions with a width that takes into account the intrinsic fluctuations on the number of spectators at a fixed impact parameter, folded with the energy resolution of the detector.

Therefore the minimum bias spectrum for all the targets has been fitted with the sum of a finite number of gaussian distributions, whose mean values and widths are free parameters of the fit. The number of the gaussian distributions used in the fit was chosen to minimize the chi-squared and vary with the target. As an example we show in Fig. 5.7 the fit to the In-Al spectrum, obtained folding four gaussian distributions.

We checked that a different choice of the initial parameters of the various gaussians did not lead to a different minimum and to different values of the fit's parameters.

The end-point of the spectrum at low energies, i.e. the ADC channel corresponding to the central collisions, was then taken as the mean value of the gaussian corresponding to the lowest energy. The Fig. 5.8 shows the result of the fitting procedure on the minimum bias spectrum for In-Sn collisions; the end-point of the spectrum at low energies is highlighted.

5.5.4 Calorimeter linearity

As can be inferred from the Eq. 5.2 for $b = 0$, the low energy end-point of the ZDC spectrum can be expressed as:

$$E_{ZDC}^{end-point} = E_{spec}(b = 0) + \alpha N_P(b = 0) \tag{5.9}$$

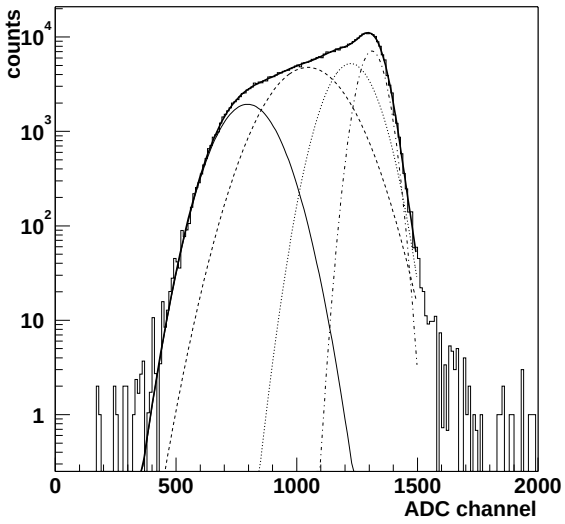

Fig. 5.7: *The spectrum corresponding to the Al target fitted with the sum of four gaussian distributions (full line); each gaussian curve is also shown (dashed line).*

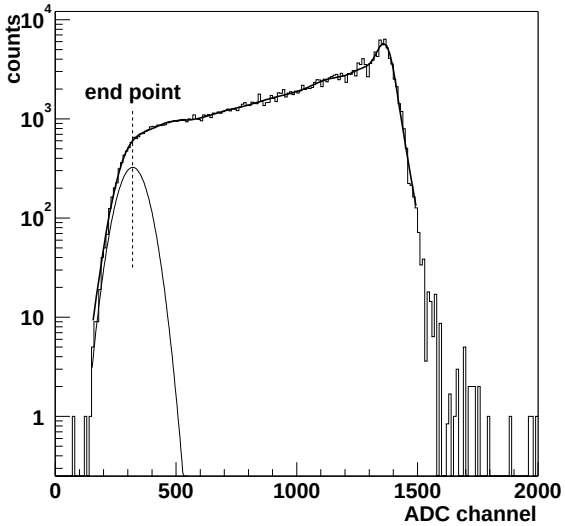

Fig. 5.8: *The spectrum corresponding to the Sn target fitted with the sum of four gaussian distributions (full line); the mean value of the most left gaussian defines the end point of the spectrum.*

where $E_{spec}(b = 0)$ is the energy due to spectator nucleons in a central collision, $N_P(b = 0)$ is the participant number in a central collision and α is the equivalent energy per participant.

In ^{115}In - ^{119}Sn central collisions all nucleons are participants, since the mass numbers of the two colliding nuclei are almost the same. In this case, the low energy end-point of the spectrum provides the detected energy due to the 115 participant nucleons. Therefore the mean energy α per participant nucleon detected by the calorimeter can be deduced as:

$$\alpha = \frac{E_{ZDC}^{end-point}(In - Sn\,collisions)}{115} \tag{5.10}$$

For all the different colliding systems we determined $E_{ZDC}^{end-point}$ and then we could calculate the ZN response to spectator nucleons in central collisions $E_{spec}(b = 0)$, subtracting the energy due to participant nucleons:

$$E_{spec}(b = 0) = E_{ZDC}^{end-point} - \alpha N_P(b = 0). \tag{5.11}$$

The results are summarized in Fig. 5.9 where this last quantity is plotted as a function of the number of spectator nucleons, as indicated in Tab. 5.3. Despite the rough approximations used in this study, the fit of the experimental data shows a linear behavior of the calorimeter response.

5.5.5 Comparison with the simulation

The same analysis was done on the simulated data. As an example, in Fig. 5.10 we plot the experimental spectrum for the Cu target, rescaled in energy, compared with the simulated spectrum. The rescaling factor from experimental ADC values to energy values was obtained simply looking at the non-interacting In beam. The simulated spectrum is slightly narrower than the experimental one; this means that the event generator used in the simulation underestimates the intrinsic fluctuations on the number of spectator nucleons or rather that the fluctuations due to the experimental detector resolution are underestimated. Nevertheless, plotting the energy corresponding to the spectator nucleons in central collisions estimated from the simulation on the same plot as the experimental points, a remarcable agreement can be seen (Fig. 5.11).

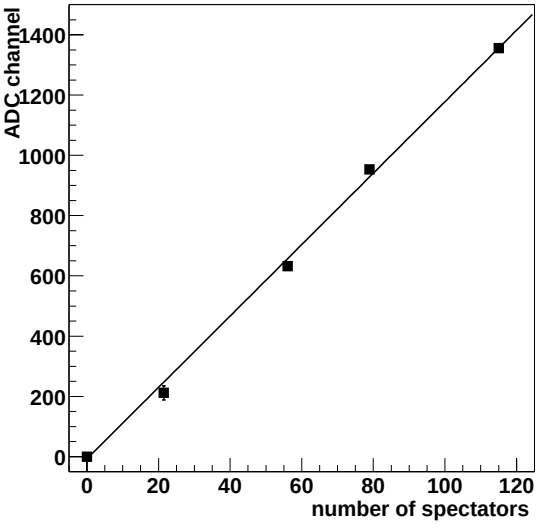

Fig. 5.9: *Response of the calorimeter as a function of the number of spectator nucleons entering on its front face.*

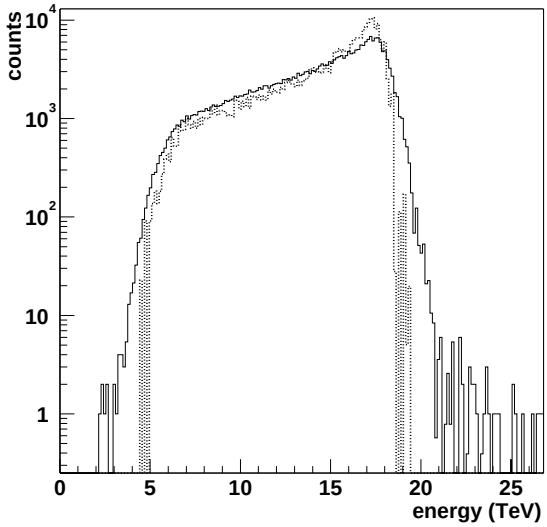

Fig. 5.10: *Comparison of the experimental minimum bias spectrum corresponding to the Cu target (full line) with the simulated one (dashed line).*

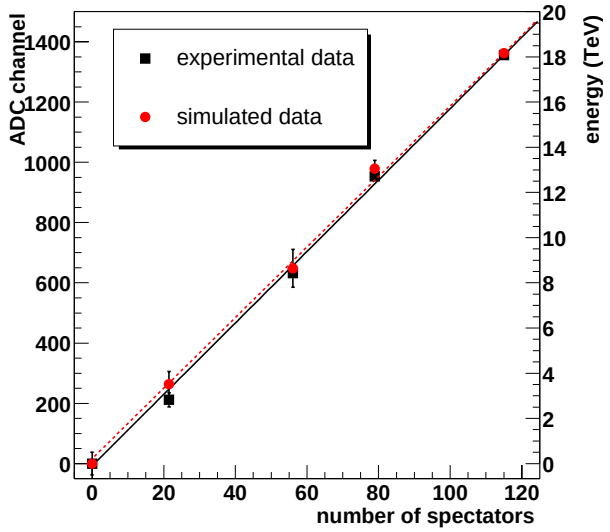

Fig. 5.11: *Comparison of the linearity of the ZN as a function of spectator nucleons between experiment and simulation.*

5.6 Beam test analysis in the Glauber model frame

The centrality of the collisions between heavy ions is characterized by the impact parameter $\overrightarrow{b}$, defined as the distance between the geometric centers of the two nuclei in the plane transverse to the projectile direction.

Central collisions are characterized by small impact parameter, while peripheral ones have large b, up to an impact parameter of the order of the sum of the projectile and targert radii: $b \sim R_{proj} + R_{target}$.

However the impact parameter is a theoretical variable that can not be measured directely. Therefore it has to be deduced, by means of a model, from experimental measurements of other variables, directly related to the collision centrality, like the zero degree energy E_{ZDC}.

The link between the zero degree energy E_{ZDC} and the centrality of the collision can be extracted by means of a geometrical model, which makes use of the Glauber theory [28].

In the framework of this theory the nucleus-nucleus collision is decribed as a superimposition of nucleon-nucleon collisions.

The model is based on a geometrical decription of the collision processes:

the projectile nucleons traverse the target nucleus following straight line trajectories and can undergo several collisions with the nucleons of the target.

The only physical inputs are the elementary inelastic baryon-baryon cross-section and the density distribution inside the nuclei.

The Glauber model assumes the basic baryon-baryon cross-section doesn't change during the passage of the baryon through the other nucleus. This is an approximation because a baryon of one nucleus can be excited and may have different cross-section when it passes through the other nucleus.

5.6.1 Model formalism

We consider the collision between two nuclei of mass number A (projectile) and B (target). A schematic view of the geometry of the collision and of the variables used in the following is shown in Fig.5.12 and Fig.5.13.

The probability of finding a baryon in the volume element $dV = d\overrightarrow{s}dz_A$ at the position $(\overrightarrow{s}, z_A)$ is given by $\rho_A(\overrightarrow{s}, z_A)d\overrightarrow{s}dz_A$, where ρ_A is the nuclear density in the $(\overrightarrow{s}, z_A)$ position normalized to the total number of nucleons of the nucleus.

Therefore the surface probability density of finding a barion at the position $\overrightarrow{s}$ in the transverse plane perpendicular to the collision axis is:

$$T_A(\overrightarrow{s}) = \int_{-\infty}^{+\infty} \rho_A(\overrightarrow{s}, z_A)dz_A \tag{5.12}$$

An analogous formula gives for the nucleus B:

$$T_B(\overrightarrow{b} - \overrightarrow{s}) = \int_{-\infty}^{+\infty} \rho_B((\overrightarrow{b} - \overrightarrow{s}), z_B)dz_B \tag{5.13}$$

which is related to the probability of finding a target baryon in the volume element $d(\overrightarrow{b} - \overrightarrow{s})dz_B$ at the position $((\overrightarrow{b} - \overrightarrow{s}), z_B)$.

$T_A(\overrightarrow{s})$ and $T_B(\overrightarrow{b} - \overrightarrow{s})$ are named *nucleus thickness functions*. $T_A(\overrightarrow{s})$ and $T_B(\overrightarrow{b} - \overrightarrow{s})$ are two normalized functions when the integration runs over all the transverse plane:

$$\int T_A(\overrightarrow{s})d^2s = \int d^2s \int_{-\infty}^{+\infty} \rho_A(\overrightarrow{s}, z_A)dz_A = 1 \tag{5.14}$$

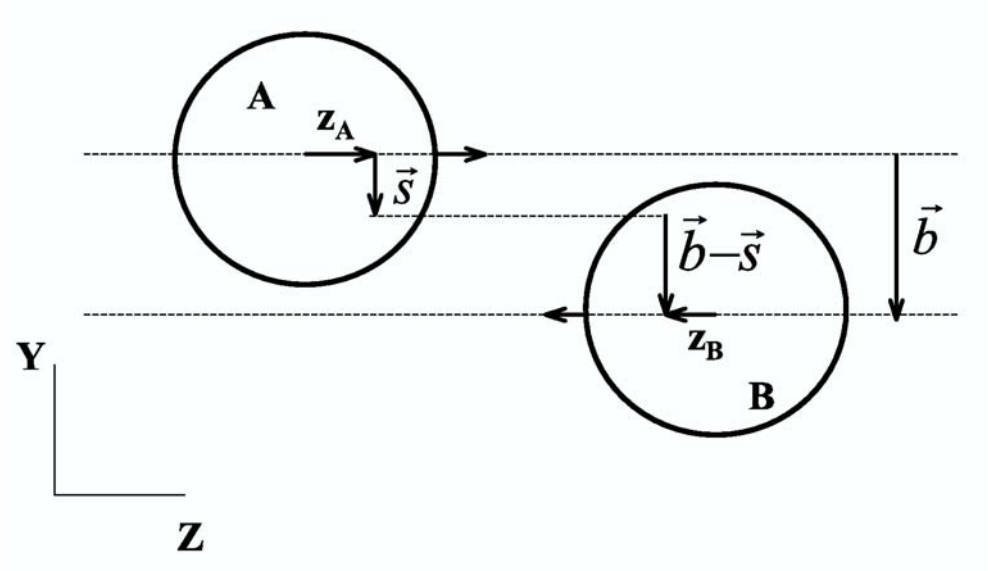

Fig. 5.12: *Longitudinal view of a nucleus-nucleus collision, with a projectile nucleus A on a target nucleus B.*

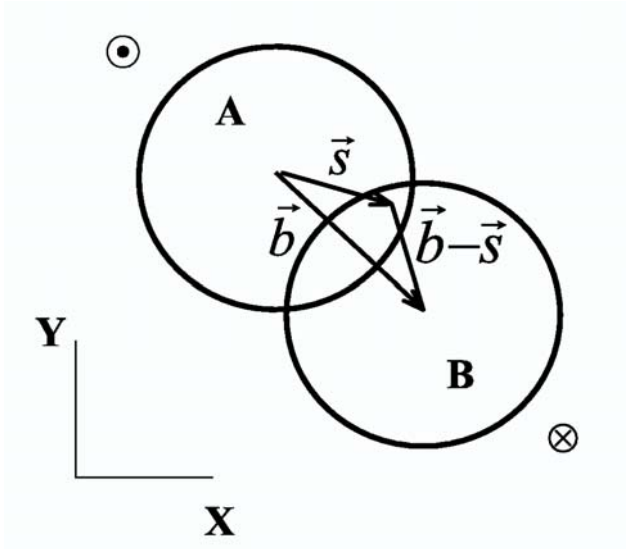

Fig. 5.13: *Transverse view of the collision between the ions A and B.*

$$\begin{aligned}\int T_B(\overrightarrow{b}-\overrightarrow{s})d^2(b-s) &= \int d^2(b-s)\int_{-\infty}^{+\infty}\rho_B((\overrightarrow{b}-\overrightarrow{s}),z_B)dz_B \\ &= 1. \end{aligned} \tag{5.15}$$

Therefore the probability for the occurence of a baryon baryon collision when the nuclei A and B are situated at a distance equal to the impact parameter $\overrightarrow{b}$ is:

$$P(1,\overrightarrow{b}) = \int d^2s T_A(\overrightarrow{s})T_B(\overrightarrow{b}-\overrightarrow{s})\sigma_{in} \equiv T_{AB}(\overrightarrow{b})\sigma_{in} \tag{5.16}$$

where σ_{in} is the inelastic nucleon-nucleon cross section of the order of 30 mb. T_{AB} is called the *nucleus-nucleus thickness function*. Also T_{AB} is normalized to unity if integrated over all the impact parameters:

$$\int T_{AB}(\overrightarrow{b})d\overrightarrow{b} = 1. \tag{5.17}$$

If nuclei are not deformed or oriented $T_{AB}(\overrightarrow{b})$ depends only on the magnitude of $\overrightarrow{b}$ and hence $T_{AB}(\overrightarrow{b})$=$T_{AB}(b)$.

Now it is possible to calculate the probability for the occurrence of n inelastic baryon-baryon collision at an impact parameter $\overrightarrow{b}$, which is given by the binomial law:

$$P(n,\overrightarrow{b}) = \left(\begin{array}{c} AB \\ n \end{array}\right)(T_{AB}(\overrightarrow{b})\sigma_{in})^n[1-T_{AB}(\overrightarrow{b})\sigma_{in}]^{AB-n} \tag{5.18}$$

where the first factor on the right-hand side represents the number of combinations for finding n collisions out of AB possible nucleon-nucleon encounters, the second factor gives the probability of having exactly n collisions and the third factor gives the probability of having exactly $AB-n$ misses.

The total probability for the occurrence of an inelastic event in the collision of the nuclei A and B, at an impact parameter $\overrightarrow{b}$, is given by the sum of Eq.5.18 from n=1 to n=AB, i.e. summing the probability $P(n,\overrightarrow{b})$ over all the nucleon couples:

$$\frac{d\sigma_{in}^{AB}}{d\overrightarrow{b}} = \sum_{n=1}^{AB} P(n,\overrightarrow{b}) = 1 - P(0,\overrightarrow{b}) \tag{5.19}$$

where

$$P(0, \overrightarrow{b}) = [1 - T_{AB}(\overrightarrow{b})\sigma_{in}]^{AB} \tag{5.20}$$

is the probability of having no baryon-baryon collisions. The probability of a nucleon-nucleon collision is one up to very peripheral collision and start to be different from unity only when the tails of the nuclear density distributions superimpose.

Finally, from Eq.5.19, the total inelastic cross secton σ_{in}^{AB} for an AB collision is:

$$\sigma_{in}^{AB} = \int d\overrightarrow{b} \left\{ 1 - \left[1 - T_{AB}(\overrightarrow{b})\sigma_{in} \right]^{AB} \right\}. \tag{5.21}$$

5.6.2 Number of Participants, Spectators and Collisions as a function of b

In the frame of the Glauber model it is possible to find the relations between the impact parameter b of the collision and other variables, like the number of participant N_p and spectator nucleons N_s or the number of collisions N_{coll}.

$N_p(b)$ at fixed b is obtained from the following equation:

$$N_p(\overrightarrow{b}) = N_p^{proj}(\overrightarrow{b}) + N_p^{target}(\overrightarrow{b}) \tag{5.22}$$

where the number of projectile participants $N_p^{proj}(\overrightarrow{b})$ and the number of target participants $N_p^{target}(\overrightarrow{b})$ are calculated respectively as:

$$N_p^{proj}(\overrightarrow{b}) = \int d^2s \left\{ AT_A(\overrightarrow{s}) \left[1 - (1 - \sigma_{in} T_B(\overrightarrow{b} - \overrightarrow{s}))^B \right] \right\} \tag{5.23}$$

$$N_p^{target}(\overrightarrow{b}) = \int d^2s \left\{ BT_B(\overrightarrow{b} - \overrightarrow{s}) \left[1 - (1 - \sigma_{in} T_A(\overrightarrow{s}))^A \right] \right\}. \tag{5.24}$$

We define *participant nucleons* all the nucleons of the projectile and of the target which have undergone at least an inelastic collision with the surrounding nucleons. The centrality dependence of the number of participants is shown in Fig. 5.14: the number of the projectile and target nucleons involved in the collision increases with the collision centrality.

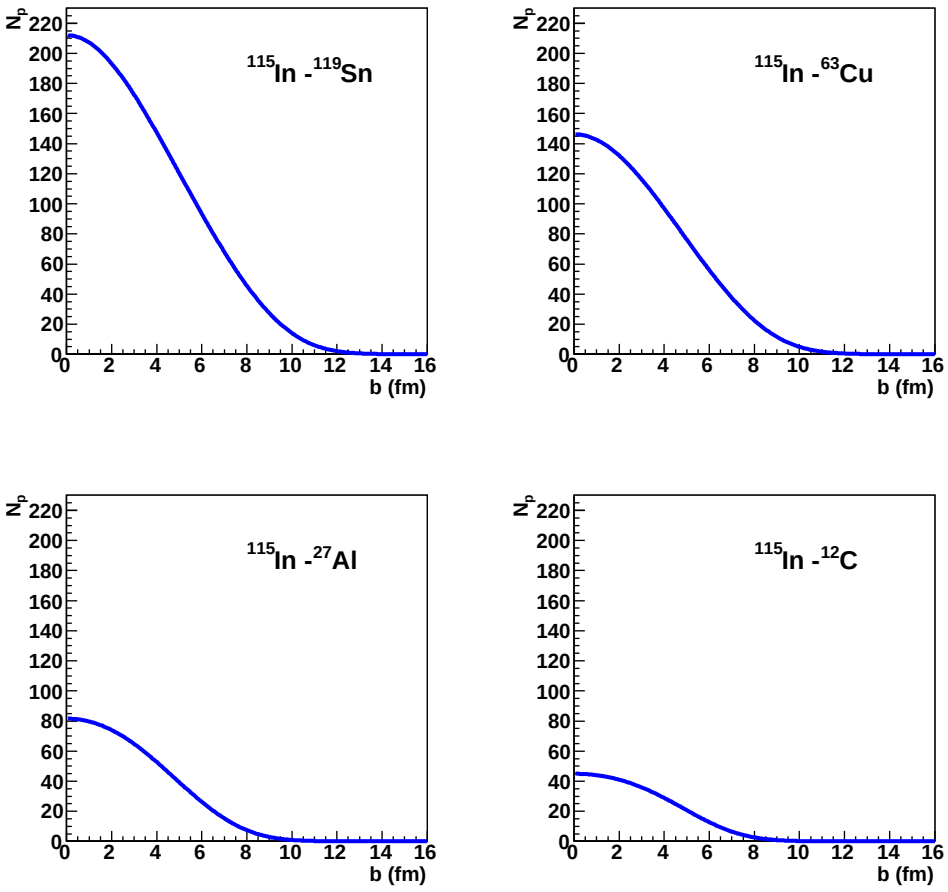

Fig. 5.14: *Participant number as a function of the impact parameter b, for the four colliding systems investigated.*

If the projectile mass number A is equal to the target mass number B, i.e. the collision is symmetric, then $N_p^{proj} = N_p^{target} = N_p/2$. In this case the number of projectile *spectators* is obtained, once the number of participants is known, from the relation:

$$N_s = A - \frac{N_p}{2}. \tag{5.25}$$

Of course, when $A \neq B$, i.e. for non-symmetric collisions, $N_p^{proj} \neq N_p^{target}$ and the number of projectile *spectators* is given by:

$$N_s = A - N_p^{proj}. \tag{5.26}$$

The centrality dependence of N_s, for the different colliding systems studied, is shown in Fig. 5.15.

The mean number of baryon-baryon collisions at fixed $\overrightarrow{b}$, $N_{coll}(\overrightarrow{b})$, is obtained from Eq.5.27:

$$N_{coll}^{AB}(\overrightarrow{b}) = \sum_{n=0}^{AB} nP(n, \overrightarrow{b}) = ABT_{AB}(\overrightarrow{b})\sigma_{in} \tag{5.27}$$

The Fig. 5.16 allows to appreciate the correlation between the number of collisions and the impact parameter b.

These results have been obtained assuming for the nuclear density the distributions plotted in Fig. 5.17 and Fig. 5.18, for the projectile nucleus and for the target nuclei respectively. When the nucleus mass number is greater or equal to 17, the nuclear density is well described by a Saxon-Woods distribution:

$$\rho(r) = k \cdot \frac{\rho_0}{1 + e^{\frac{r-c}{z}}} \tag{5.28}$$

where $\rho_0 = 0.16\, nucleons/fm^3$, r is the position relatively to the center of the nucleus, while the parameters c and z have been obtained from electron-nucleus scattering experiments[29, 30]. The normalisation factor k has been evaluated requiring that the nuclear density integral over the whole nucleus volume is equal to the nucleus mass number $\mathcal{A}$:

$$\int \rho(r) dV = \mathcal{A}. \tag{5.29}$$

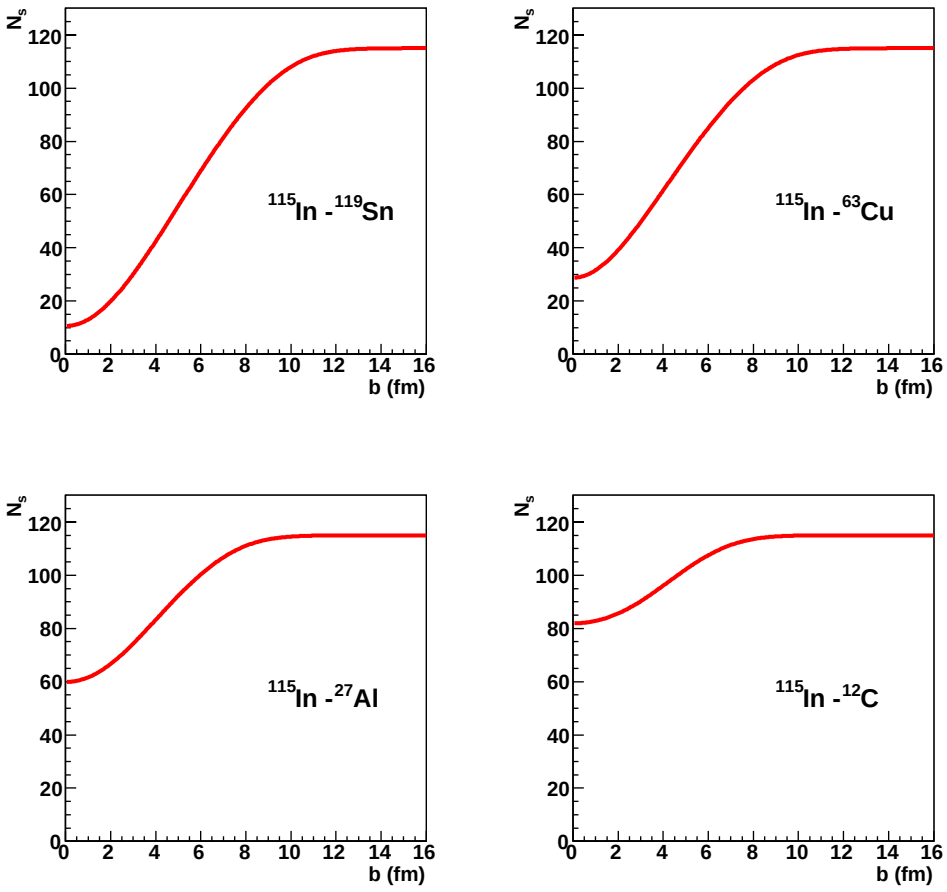

Fig. 5.15: *Spectator number as a function of the impact parameter b, for the four colliding systems investigated.*

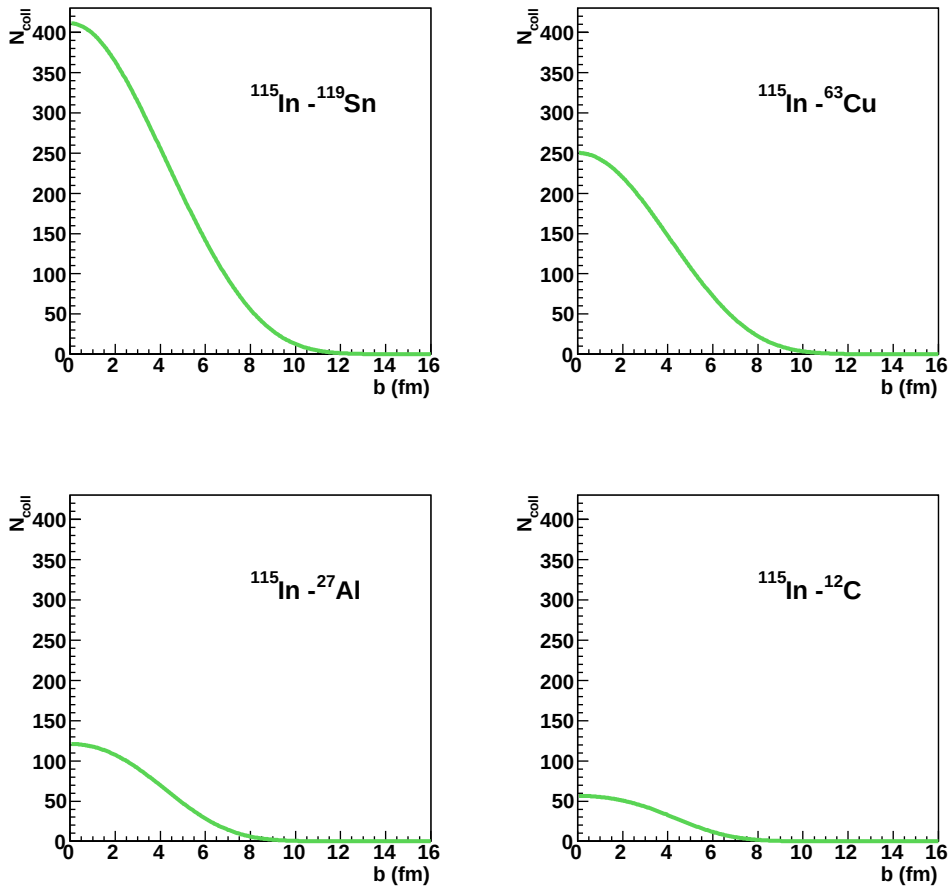

Fig. 5.16: *Number of collisions as a function of the impact parameter b, for the different colliding systems studied.*

In our study, the Saxon-Woods nuclear density description is suitable for the projectile ^{115}In and for the three heaviest targets (^{119}Sn, ^{63}Cu, ^{27}Al). In Tab. 5.5 the nuclear density parameters for these nuclei are shown.

For the light target ^{12}C, the nuclear density is given by a harmonic oscillator shell model [31]:

$$\rho(r) = k \cdot (\pi R^2)^{-3/2} e^{-\frac{r^2}{R^2}} \tag{5.30}$$

where $k = 12.0$ is the normalisation factor, calculated requiring the condition described in the Eq. 5.29, while $R^2 = 0.8133 \mathcal{A}^{2/3}\, fm^2$.

Nucleus	$c\,(fm)$	$z\,(fm)$	k	*Parametrisation reference*
^{119}Sn	5.32	0.575	1.057	[30]
^{115}In	5.357	0.563	1.005	[29]
^{63}Cu	4.163	0.606	1.078	[29]
^{27}Al	2.84	0.569	1.259	[29]

Tab. 5.5: *Saxon-Woods nuclear density distribution parameters.*

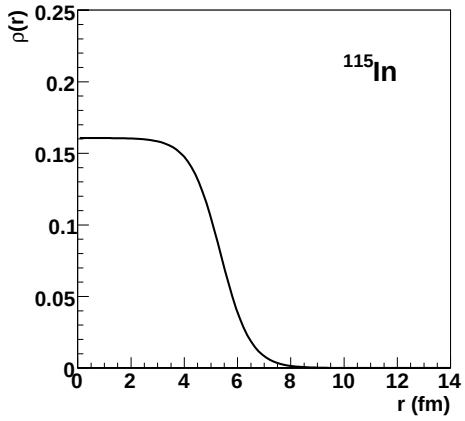

Fig. 5.17: *Saxon-Woods distribution for the nuclear charge density as a function of the distance r from the nucleus center, for the projectile nucleus.*

5.6.3 Theoretical shape of the E_{ZDC} spectrum

In order to find the link between the experimental variable E_{ZDC} and the centrality of the collision it is necessary to take into account also the characteristics of the detector.

As discussed in section 5.5, the mean energy detected by the ZDC in ion-ion collisions at 158 AGeV/c incident momentum can be written, for each impact parameter b, as the sum of the energy due to the spectator and the energy due to the participant nucleons:

$$< E_{ZDC}(b) >= E_{spec}(b) + E_{part}(b) = 158 \times N_s(b) + \alpha N_p(b) \qquad (5.31)$$

where N_s is the number of spectator nucleons and N_p is the number of participant nucleons. The relation between N_s (or N_p) and the impact parameter b is obtained in the Glauber model frame, by means of the Eq. 5.26 (or Eq. 5.22). The parameter α, which accounts for the equivalent energy per participant, depends mainly on the rapidity range where the produced secondaries are measured. The participant contribution to the measured E_{ZDC} energy is important only for very central collisions.

The estimation of the E_{ZDC} spectrum in the frame of the Glauber theory goes through the calculation of the probability $P(E_{ZDC}, b)$ of measuring the value E_{ZDC} in a collision with a fixed impact parameter b. Such a probability follows a gaussian distribution around the mean value $< E_{ZDC}(b) >$. The

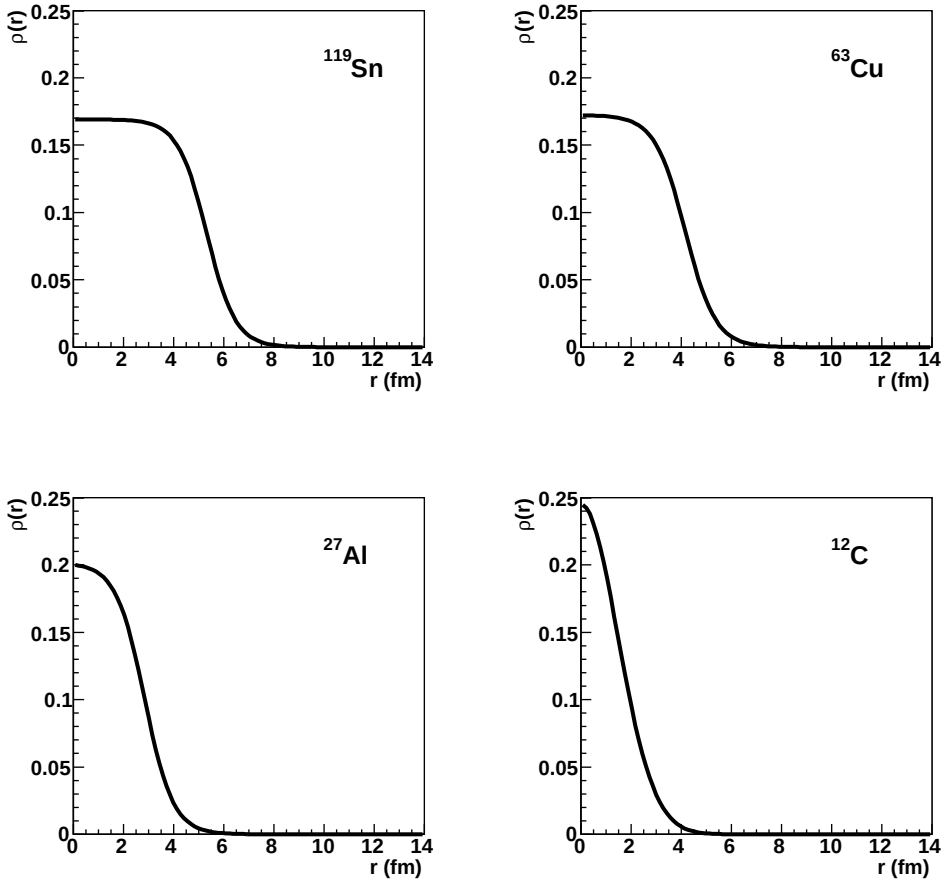

Fig. 5.18: *Nuclear charge density profile as a function of the distance r from the nucleus center, for the target nuclei.* ^{119}Sn, ^{63}Cu, ^{27}Al *are described by a Saxon-Woods distribution, while for the* ^{12}C *the nuclear density is given by a harmonic oscillator shell model.*

width of the gaussian curve reflects both the enlargement due to the detector experimental resolution ($\sigma_{detector}$) and the physical fluctuations ($\sigma_{physics}$) on the number of the nucleons involved in the collision:

$$\sigma_{E_{ZDC}}(b) = \sigma_{detector}(b) \oplus \sigma_{physics}(b). \tag{5.32}$$

$\sigma_{detector}$ is decribed by two terms which take into account the calorimeter resolution:

$$\sigma_{detector}(b) = \sigma_{spec}(b) \oplus \sigma_{part}(b). \tag{5.33}$$

The term relative to the experimental fluctuations on the spectator energy measurement can be evaluated from the independent nucleons model (see Sec. 5.4):

$$\sigma_{spec}(b) = E_{spec}(b) \cdot \frac{\sigma_n}{E_n} \cdot \frac{1}{\sqrt{N_s(b)}} \tag{5.34}$$

where $\frac{\sigma_n}{E_n} = 0.229$ is the resolution on a single $158\,GeV/c$ nucleon, extrapolated from the experimental data of the previous pions beam test (see Chap. 3).

Using the informations of the same beam test we have determined the parameters $\beta = 0.081\,TeV^{1/2}$ and $\gamma = 0.10$ of the usual calorimeter resolution, involved in the description of the second term in the detector experimental resolution:

$$\sigma_{part}(b) = E_{part}(b) \cdot \left(\frac{\beta}{\sqrt{E_{part}(b)}} \oplus \gamma \right). \tag{5.35}$$

In the following study the parameters β and γ have been kept fixed.

For a given value of the impact parameter b the number of spectator nucleons fluctuates around the mean value $< N_s >$, inducing a fluctuations around the corresponding $< E_{ZDC}(b) >$. Since this kind of fluctuations is not taken into account by the Glauber model we have introduced the physical fluctuations $\sigma_{physics}(b)$ evaluated separately by means of a Monte Carlo simulation. The Fig.5.19 shows, for the different colliding systems considered, the energy resolution contribution σ_{N_s}/N_s, due exclusively to the physics fluctuations on the spectator number, obtained using the HIJING event generator.

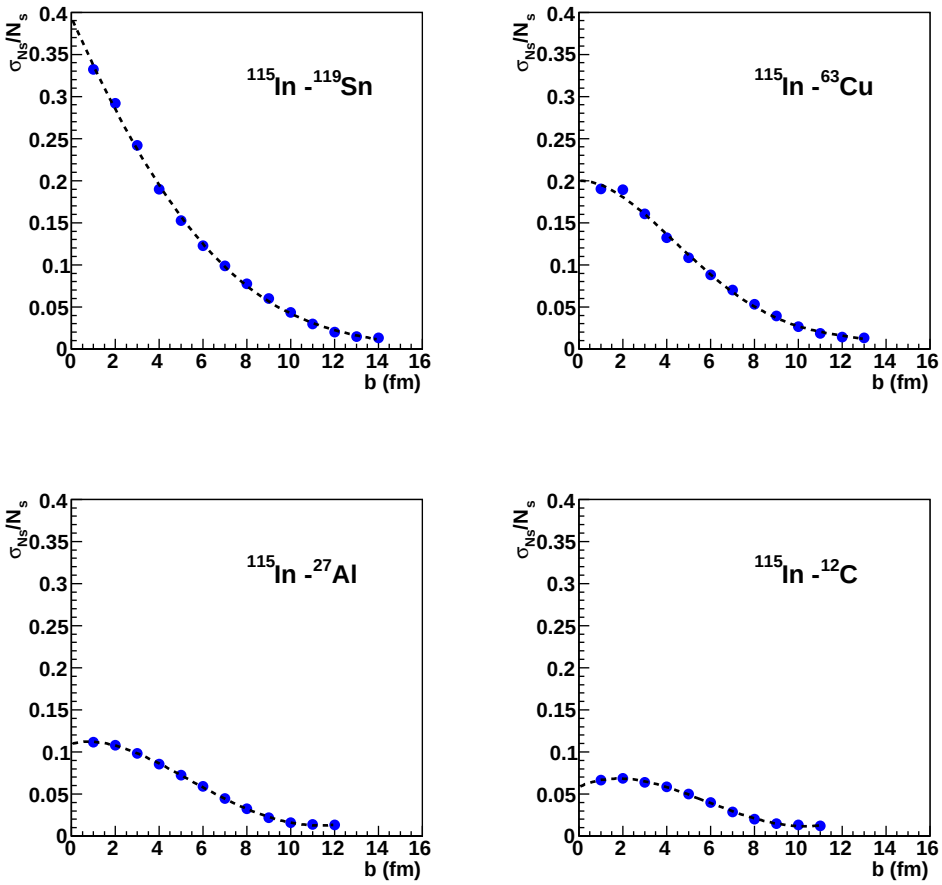

Fig. 5.19: *Energy resolution contribution due esclusively to the physics fluctuations on the spectator number. For all the colliding systems, the plot have been obtained from a HIJING simulation. The dashed line represent a 4^{th} order polinomial fit of the data, used to parametrize this contribution as a function of the centrality.*

This contribution has been parametrized as a function of the centrality of the collision and the corresponding enlargement has been calculated as:

$$\sigma_{physics}(b) = E_{spec}(b) \cdot \frac{\sigma_{N_s}}{N_s}(b). \tag{5.36}$$

When $< E_{ZDC}(b) >$ and $\sigma_{E_{ZDC}}(b)$ have been calculated, the probability $P(E_{ZDC}, b)$ of measuring the value E_{ZDC} in a collision with a fixed b value, can be expressed as:

$$P(E_{ZDC}, b) = \frac{1}{\sqrt{2\pi}\sigma_{E_{ZDC}}(b)} exp\left(-\frac{(E_{ZDC} - < E_{ZDC}(b) >)^2}{2\sigma^2_{E_{ZDC}}(b)}\right). \tag{5.37}$$

The minimum bias theoretical shape of the E_{ZDC} spectrum is given by:

$$\frac{dN}{dE_{ZDC}} = \delta \cdot \int 2\pi b[1 - P(0, b)]P(E_{ZDC}, b)db \tag{5.38}$$

where δ is a normalisation free parameter and $P(E_{ZDC}, b)$ has been weighted with the impact parameter probability. In fact, as can be seen in Fig. 5.20, the minimum bias impact parameter distribution is not uniform, but it is distributed according to the realation:

$$dN = 2\pi b[1 - P(0, b)]db \tag{5.39}$$

where $2\pi bdb$ comes from the collision geometry and $P(0, b)$ (see Eq. 5.20) is the probability for no nucleon-nucleon interactions. Hence $[1 - P(0, b)]$ requires at least a nucleon-nucleon inelastic collision and cuts off the integral at large b, when nuclear interactions become impossible. It is important to note that weighting the Eq. 5.38 with the impact parameter probability, the non interacting ions are eliminated from the theoretical E_{ZDC} spectrum.

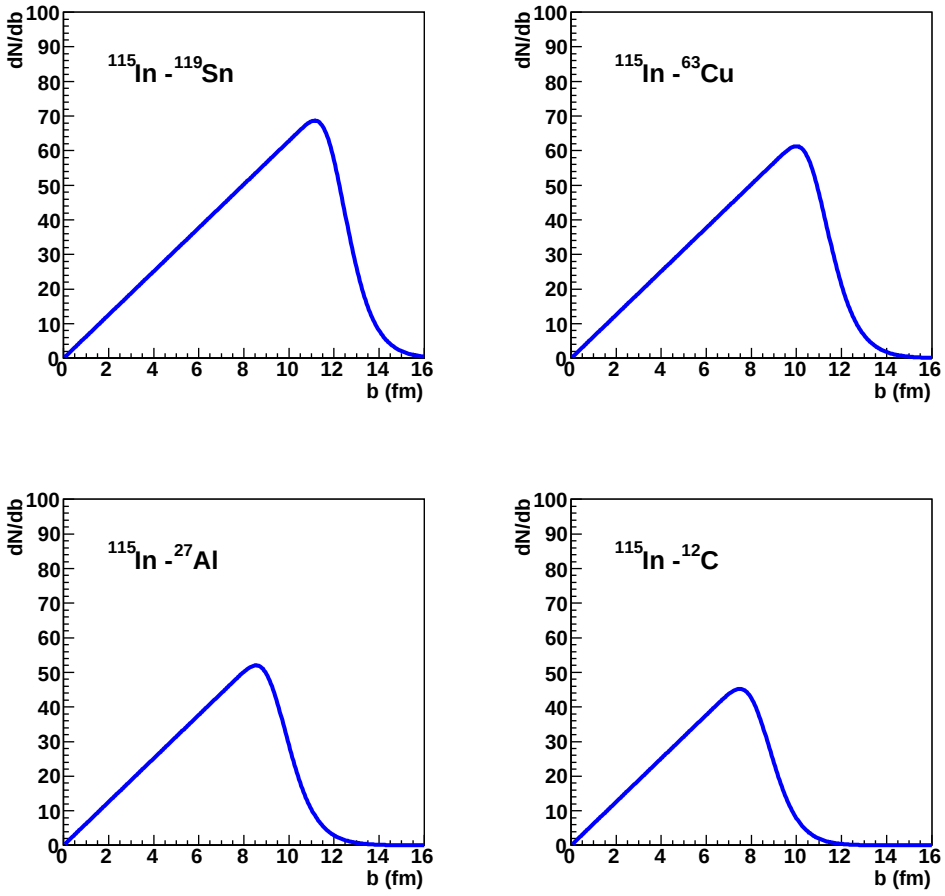

Fig. 5.20: *Minimum bias impact parameter distributions, for all the colliding systems studied.*

5.6.4 Glauber fit to the experimental minimum bias E_{ZDC} spectra

The theoretical expression for dN/dE_{ZDC}, described by the Eq. 5.38, contains the four parameters α, β, γ, and δ that, in principle, can be determined directly fitting the experimental spectrum. However, since the parameters β and γ have been obtained experimentally by means of a previous dedicated beam test, these two parameters have been kept fixed in the fit procedure.

The Glauber fit has been performed on the minimum bias E_{ZDC} spectra, after the removal of the non interacting ions and the empty target spectrum subtraction, as discussed in Sec. 5.5. These spectra have also been rescaled from experimental ADC values to energy values simply looking at the non-interacting In ion peak position.

The results of the fit are shown in Fig.s 5.21-5.24, for the different colliding systems studied. The Tab. 5.6 reports the minimization status and the value of the α parameter which takes into account the equivalent energy per participant.

Even if there are only two free parameters, i.e. the parameter α and the overall normalisation, the experimental data for $^{115}In -^{119} Sn$, $^{115}In -^{63} Cu$ and $^{115}In -^{27} Al$ collisions are well described by the theoretical minimum bias spectrum obtained in the frame of the Glauber model, particularly for the most central events. The discrepancy that can be noticed for the most peripheral events is probably due to the effect of the cut imposed on the signal of the scintillator S3 in order to remove the non interacting beam (see Sec. 5.5.1).

With this approach all the experimental spectra (except the one corresponding to $^{115}In -^{12} C$ colliding system) are well reproduced; this means that the relation between the centrality variables N_s, N_p and the experimentally measured quantity E_{ZDC} has been correctly chosen. Since this relation (Eq. 5.31) is intrinsically linear as a function of the number of spectator and participant nucleon, this analysis, based on the Glauber model frame, represents a further check of the calorimeter response linearity.

Unfortunately for the case of the most light target (^{12}C) the Glauber fit of the experimental spectrum does not converge. It is rather diffucult to understand this behavior, however we suppose that a possible reason could be the reinteraction in air of the nuclear fragments produced in the collision. In fact, even if for peripheral collisions this effect is always present, also for the more heavy targets, for the central events more light is the target more the reinteraction effect becomes important. In effect if we look at the Tab. 5.6, we can see that the α parameter value for the light target ^{27}Al is

Target	α *parameter (GeV)*	*Minimization status*
^{119}Sn	10.71	*Converged*
^{63}Cu	10.47	*Converged*
^{27}Al	1.18	*Converged*
^{12}C	-	*Not converged*

Tab. 5.6: *Results of the Glauber fit performed on the minimum bias E_{ZDC} spectra. The errors on the free parameter α are negligible.*

already significantly different from the ^{119}Sn and ^{63}Cu ones, indicating that the model has some limitation for the light targets.

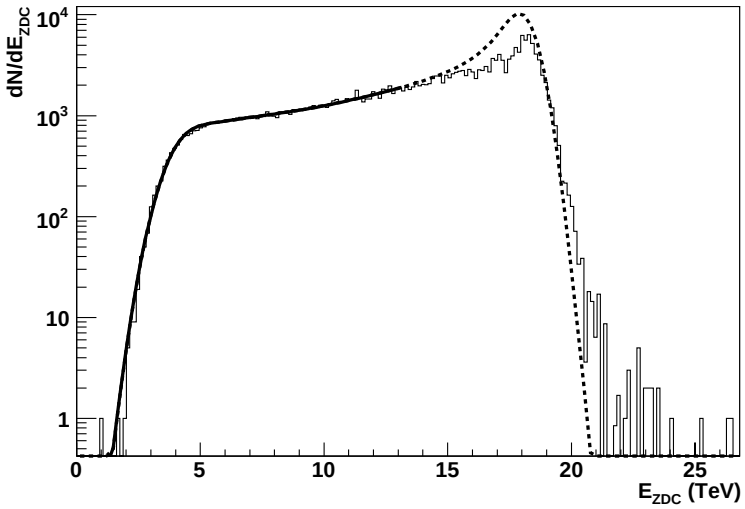

Fig. 5.21: *Experimental E_{ZDC} minimum bias spectrum for $^{115}In -^{119}Sn$ collisions. The full line represents the Gluber fit to the data, while the dashed line is the extension of the function beyond the range of the fit.*

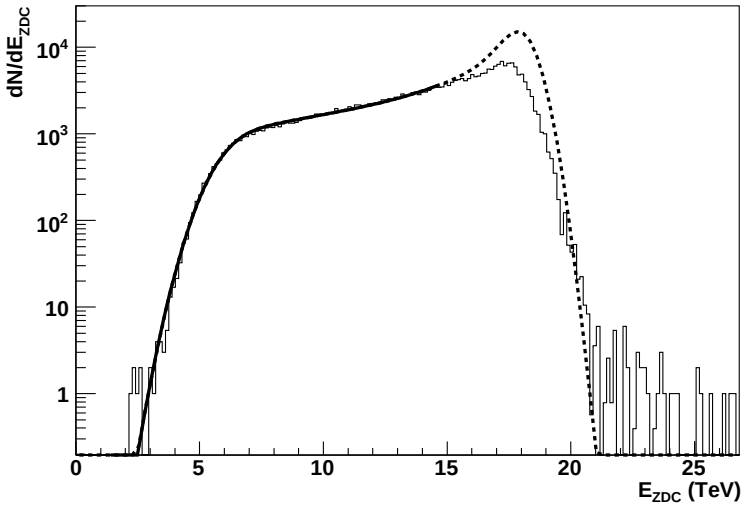

Fig. 5.22: *Experimental E_{ZDC} minimum bias spectrum for $^{115}In -^{63}Cu$ collisions. The full line represents the Gluber fit to the data, while the dashed line is the extension of the function beyond the range of the fit.*

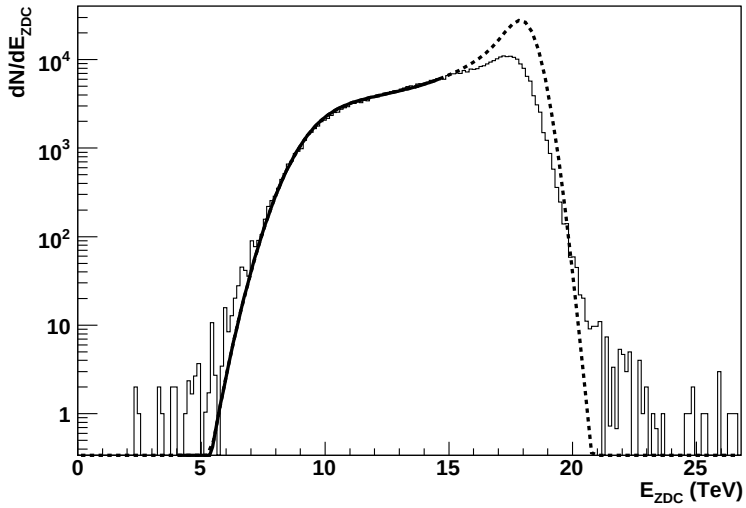

Fig. 5.23: *Experimental E_{ZDC} minimum bias spectrum for $^{115}In-^{27}Al$ collisions. The full line represents the Gluber fit to the data, while the dashed line is the extension of the function beyond the range of the fit.*

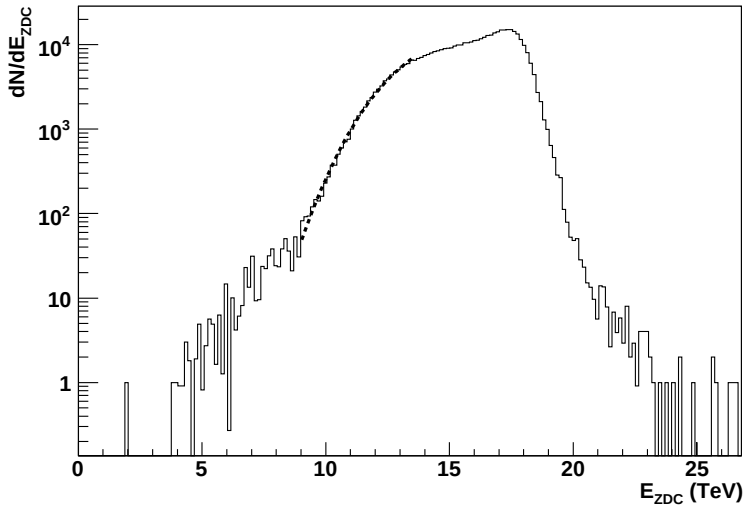

Fig. 5.24: *Experimental E_{ZDC} minimum bias spectrum for $^{115}In-^{12}C$ collisions. The dashed line represents the Gluber fit to the data, although in this case there is not convergence.*

Chapter 6

Reaction plane determination with ALICE ZDCs

6.1 Introduction

6.1.1 Flow

The generic term *flow* refers to a phenomenon always present in nucleus-nucleus collisions, which is expected to be observed also at the LHC. Flow is a collective motion of particles, due to the expansion of the hot and compressed nuclear matter created in the collision [32, 35]. The notion of flow should be understood as a phenomenological description of the expansion, without any reference to a specific theoretical interpretation. In particular, it doesn't necessarily imply any hydrodynamic behavior, although the underlying physics is conveniently pictured in terms of pressure gradients. Since the flow is a collective phenomenon which affects all, or almost all, particles in a given event, it indicates the presence of multiple interactions between the outgoing particles which contribute to the appearence of an overall pattern, while in nucleon-nucleon collisions such effects are absent.

Depending on collision energy, flow reflects different collective aspects of the interacting medium. At low energies, where relatively few new particles are created, flow effects are mostly caused by the nucleons from the incoming nuclei. At high energies the number of newly created particles is so large that it is their behavior which dominates the observable flow effects. The primordial nucleons are expected to make only minor contributions to the dynamical process inside the reaction volume, in particular in the region near mid-rapidity. The usual theoretical tools to describe flow in that regime are hydrodynamic or microscopic transport (cascade) approaches. Flow depends in the latter models on the interaction cross section, be it partonic or

hadronic. Hydrodynamics, on the other hand, is valid only when the mean free path of particles is much smaller than the system size and relies on a description of the system in terms of macroscopic quantities [33].

In the following subsections we introduce the possible different patterns of collective flow: there can be an isotropic expansion (radial flow), in central collisions, as well as, in non-central collisions, a non isotropic component (anisotropic flow). In particular, the definition of the reaction plane will be given and an approach to the study of anisotropic flow which uses the Fourier expansion of azimuthal distributions will be summarized.

In the subsequent sections we will discuss the localizing capability of the ALICE neutron zero degree calorimeter. This is an essential detector feature because it allows to reconstruct the first order event plane. Then we will illustrate the results of a simulation performed in order to evaluate the resolution on the event plane reconstructed by means of the ZN calorimeter, studying its dependence on different parameters as the directed flow v_1 value, the neutron multiplicity, the LHC beam parameters and the detector granularity.

6.1.2 Radial flow

In central collisions between spherical nuclei, the initial state is symmetric in azimuth. This impies that the azimuthal distribution of the final state particles is isotropic as well. Under such conditions, any pressure gradient will cause an azimuthally symmetric collective flow of the outgoing particles which is called *radial flow*. The relevant observables to study such effects are the transverse momentum distributions of the various particle species. For a given particle type, the random thermal motion is superimposed onto the collective radial flow velocity which may or may not depend on space and time. Correspondingly, the invariant transverse-momentum distribution of a specific particle type depends on the temperature at freeze-out, the particle mass and the velocity profile in space-time. Furthermore, particles originating from resonance decays may follow different trends and thereby introduce modifications of the spectral shapes [33].

6.1.3 Anisotropic flow

In non-central collisions the pressure gradients will, in general, not be azimuthally symmetric. The impact parameter **b** defines a direction in the plane perpendicular to the beam, relative to which the net pressure gradient may be probed (Fig. 6.1). These pressure gradients establish a correlation between configuration and momentum space. The initial anisotropy in the

transverse configuration space translates into an anisotropy of the transverse momentum distribution of outgoing particles, which is referred to as *anisotropic flow*. The anisotopic flow pattern depends on the collision energy, the phase-space region under consideration (rapidity, tranverse momentum) and on the particle species [33].

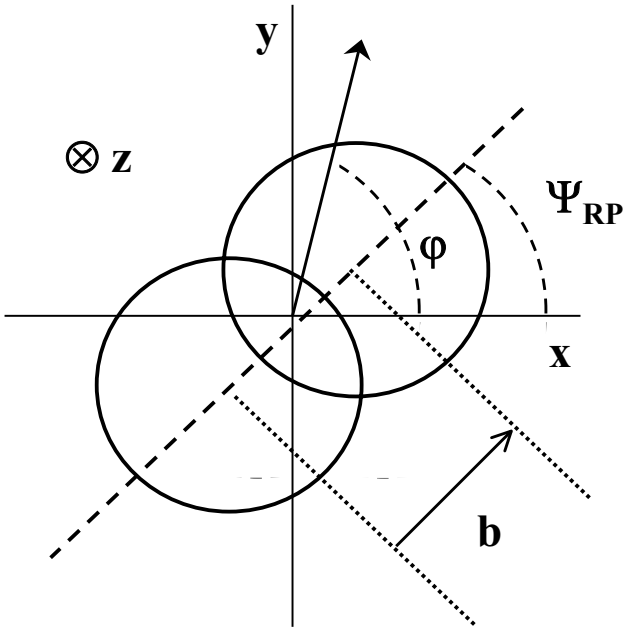

Fig. 6.1: *Definition of the coordinate system in the tranverse plane:* φ *and* Ψ_{RP} *are respectively the particle and the (true) reaction-plane azimuthal angles in the laboratory frame.*

A convenient way of characterizing the various patterns of anisotropic flow is to use a Fourier expansion of azimuthal particle distribution [39]. The essence of the method is to first estimate the *reaction plane*, the plane determined by the impact parameter and the beam axis. The estimated reaction plane is called *event plane*. The method allows to determine the event plane independently for each harmonic of the anisotropic flow. The Fourier coefficients in the expansion of the azimuthal distribution of particles with respect to this event plane are evaluated.

The dependence on the particle emission azimuthal angle measured with respect to the reaction plane can be written in a form of Fourier series:

$$\frac{dN}{d(\varphi - \Psi_{RP})} \propto 1 + 2v_1 cos(\varphi - \Psi_{RP}) + 2v_2 cos[2(\varphi - \Psi_{RP})] + ... \qquad (6.1)$$

where φ and Ψ_{RP} are respectively the particle and the (true) reaction-plane azimuthal angles in the laboratory frame. The sine terms in such an expression vanish due to the reflection symmetry with respect to the reaction plane.

The Fourier coefficients in Eq.6.1 are given by:

$$v_n = < cos[n(\varphi - \Psi_{RP})] > \qquad (6.2)$$

where the angular brackets denote an average over all particles in all events.

Different kinds of anisotropies correspond to different harmonics of Fourier expansion. In particular, anisotropic flow corresponding to the first two harmonics plays a very important role and special terms are used for them: directed and elliptic flow, respectively.

The word *directed* comes from the fact that such flow has a direction (Fig. 6.2)[32]. The directed flow arises from a build-up of the pressure between the two nuclei during the time of overlap. In such a case the flow of the nucleons from the projectile nuclei must have its maximum in the reaction plane. Furthermore, the flow of particles originating from one of the nuclei is equal in magnitude but opposite to the flow of particles from the other nucleus. In fixed target experiments the directed flow of the projectile remnants is defined as positive. In collider experiments it is desirable to adopt an equally arbitrary (but consistent) convention that directed flow of *forward-going* nucleons is taken to be positive. Directed flow is large at low energies but it is significantly reduced at high energies. In fact the velocity of the incoming nuclei at ultra-relativistic energies is such that most of the available energy flows in the longitudinal direction rather than in the transverse plane.

As said above, the second harmonic of Fourier expansion corresponds to the anisotropic pattern known as *elliptic flow*. This term is due to the fact that in polar coordinates the azimuthal distribution with nonzero second harmonic represents an ellipse (Fig. 6.3). A positive v_2 coefficient corresponds to an *in plane* particle emission excess, while a negative v_2 value implies an *out of plane* overmuch emission (Fig. 6.4).

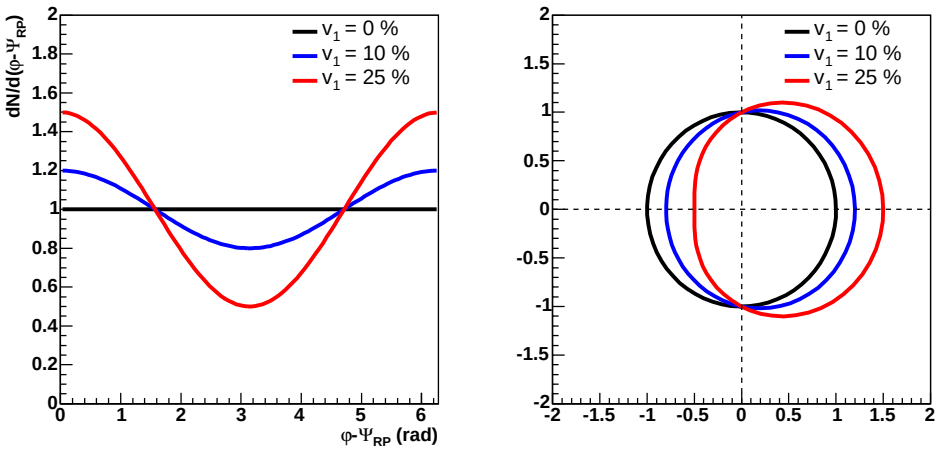

Fig. 6.2: *The left plot shows the normalized azimuthal particle distributions when we take into account the first harmonic of the Fourier expansion, for three different v_1 values; v_1=0 refers to the isotropic case. The same distributions are represented on the right, in a polar coordinate system (R,θ), with $R = dN/d(\varphi - \Psi_{RP})$, and $\theta = \varphi - \Psi_{RP}$. It is clear that a directed flow coefficient $v_1 \neq 0$ implies a preferential direction, in the reaction plane, for the particle emission.*

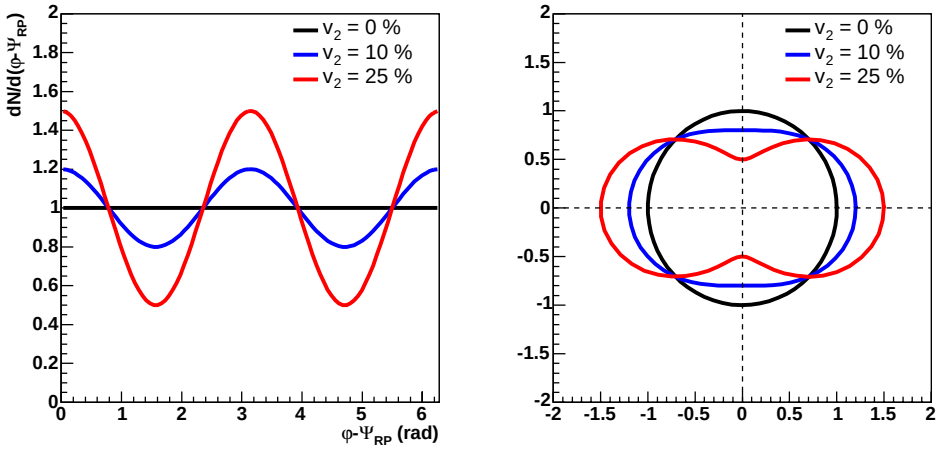

Fig. 6.3: *The left plot shows the normalized azimuthal particle distributions when we take into account the second harmonic of the Fourier expansion, for three different v_2 values. The same distributions are represented on the right, in a polar coordinate system, with a radius $R = dN/d(\varphi - \Psi_{RP})$, and an angle $\theta = \varphi - \Psi_{RP}$. For $0 < v_2 \leq 10\%$ the azimuthal distribution represent an ellipse. For greater v_2 values the ellipse is deformed, as can be seen for v_2=25%.*

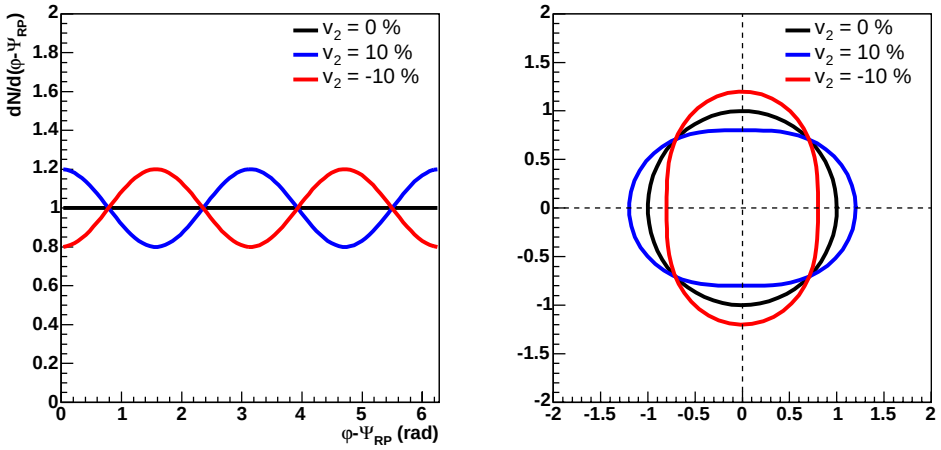

Fig. 6.4: *Positive and negative values of v_2 correspond, respectively, to an in plane elliptic flow and to an out of plane elliptic flow.*

6.2 ZN localizing capability

The ZDCs can provide information not only on the magnitude of the impact parameter vector, and therefore on the centrality of the collisions, but also on its direction [34].

The four tower segmentation of the neutron-zero degree calorimeter (Chap.1) makes this detector a rough position sensitive device. In fact the responses coming from the four towers allow to reconstruct, event by event, the centroid of the spectator neutrons spot on the ZN front face.

To evaluate the resolution on the centroid reconstructed coordinates a GEANT-based simulation has been performed. The spectator neutrons have been generated with the beam nucleon energy (2.76 TeV) and with a momentum distribution taking into account Fermi momentum and a transverse Pb beam divergence at the interaction point of 30 μrad. The simulation code tracks the neutrons in the calorimeter, where the hadronic shower deposits light in the four towers.

6.2.1 Optimization of the centroid coordinate reconstruction

The most natural way to estimate the coordinates of the centroid of the spectator neutron spot on the ZN front-face is simply to calculate the weighted mean of the coordinates x_i and y_i of the center of the i-th tower

$$x = \frac{\sum_{i=1}^{4} x_i w_i}{\sum_{i=1}^{4} w_i} \qquad y = \frac{\sum_{i=1}^{4} y_i w_i}{\sum_{i=1}^{4} w_i} \qquad with \qquad w_i = E_i \tag{6.3}$$

where E_i is light in the i-th tower.

Unfortunately, for a single neutron hitting the calorimeter front face, taking as weight simply the energy detected by each tower, the reconstructed impact point is not accurate, but is systematically shifted towards the center of the tower hit by the particle [8]. Actually, since the tower size is comparable to the shower size, most of the energy is contained in the tower hit by the neutron. In this way the position calculation is dominated by this tower if the coordinates of the tower center are weighted linearly with the energy [37]. The result is a saturation effect shown in Fig. 6.5, where the reconstructed coordinate is plotted as a function of the true one, known from the simulation. It can be seen that there are small fluctuations in the reconstructed coordinate for a given incidence position. However the systematic errors in the reconstructed coordinate relative to the true incident

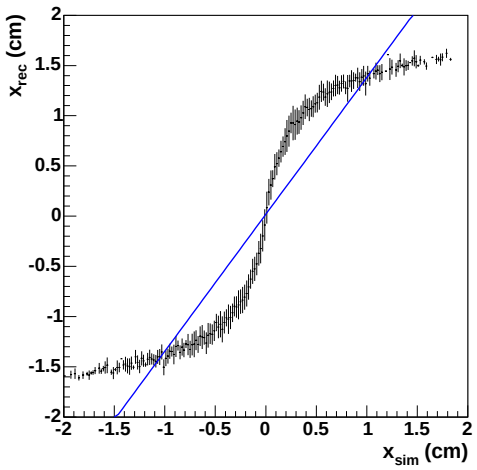

Fig. 6.5: *The average of the coordinate x_{rec}, reconstructed with a simple weighted mean (eq. 6.3), is plotted against the true incident coordinate, known from the simulation, for a single neutron hitting the calorimeter front-face. The blue line represents a linear least square fit of the distribution.*

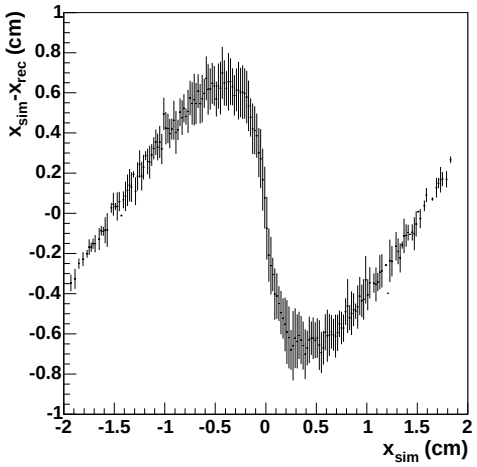

Fig. 6.6: *The average of the difference between the true position and the position calculated with the equation 6.3, is represented as a function of the true position, for a single neutron hitting the calorimeter front-face.*

coordinate are large, as shown in Fig. 6.6, where the average of the difference between the true position and the position calculated with the equation 6.3, is represented as a function of the true position [37]. The saturation effect is obviously less important for higher neutron multiplicity, when the centroid is closer to the calorimeter center (Fig. 6.7).

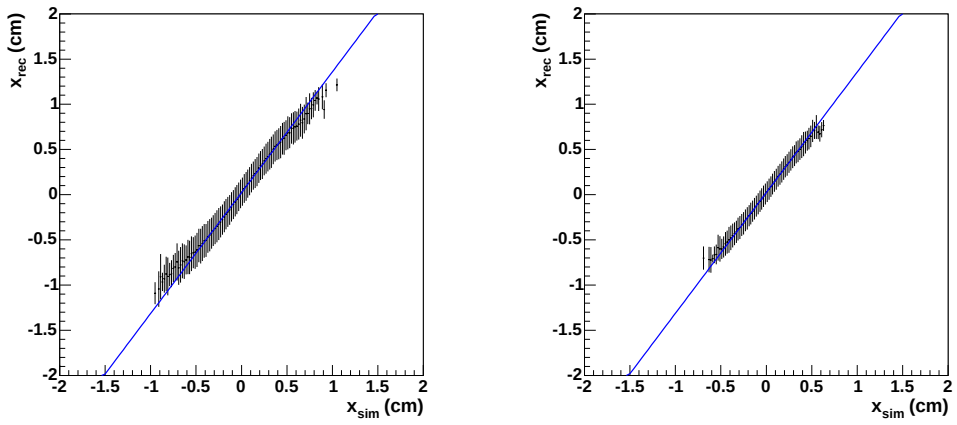

(a) (b)

Fig. 6.7: *The average of the coordinate x_{rec}, reconstructed with a simple weighted mean (eq. 6.3), is plotted against the true incident coordinate, known from the simulation, for 10, in (a), or 20, in (b), neutrons hitting the calorimeter front-face. The blue line represents a linear least square fit of the distribution.*

In order to get an accurate reconstructed impact coordinate two correction parameters, α and c, have been introduced in two subsequent steps. In a first step we redifined the weights as $w_i = E_i^{\alpha}$. For the most critical case of a single neutron hitting the calorimeter, we imposed a cut on the x coordinate considering only the events within 1 σ of the neutron spatial distribution,from the ZN center. Then we determined the best value of α which minimize the difference between the reconstructed coordinate and the true coordinate. We obtained an α value of 0.395, that provides an accurate reconstructed coordinate, in the cut region, also for higher neutron multiplicity. In the second step the cut on the x coordinate was released and the α parameter fixed at the previous value. For each considered neutron multiplicity, a fit of the x reconstructed versus x simulated distribution has been performed with the linear least square technique to evaluate the slope of the

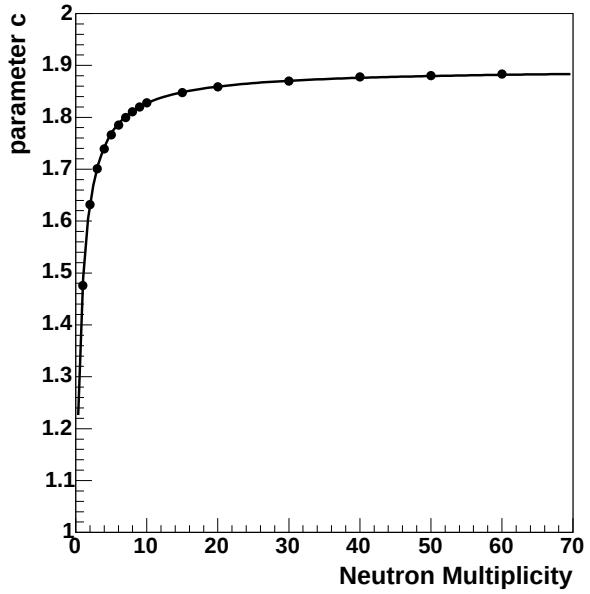

Fig. 6.8: *The correction parameter* **c** *is plotted as a function of the neutron multiplicity.*

distribution and determine the c parameter value which makes it equal to 45°[38].

Therefore the centroid of spectator neutrons spot on the ZN front-face is estimated by means of the relations:

$$x = c\frac{\sum_{i=1}^{4} x_i w_i}{\sum_{i=1}^{4} w_i} \qquad y = c\frac{\sum_{i=1}^{4} y_i w_i}{\sum_{i=1}^{4} w_i} \qquad with \qquad w_i = {E_i}^{\alpha} \tag{6.4}$$

where α=0.395 and c varies with the neutron multiplicity as shown in Fig. 6.8.

A comparison between Fig. 6.5 and Fig. 6.9 show the improvement achieved, in the coordinate reconstruction, introducing the correction parameters, for the case of a single neutron hitting the calorimeter front face.

6.2.2 Centroid coordinate resolution estimation

Since the true coordinate is known from simulation, it is possible to calculate the difference between the centroid coordinate reconstructed by ZN and the true one for different neutrons multiplicity. The RMS of the distributions of these differences give an estimation on the resolution on the centroid coordinate. The Fig. 6.11 shows that the centroid resolution improve as

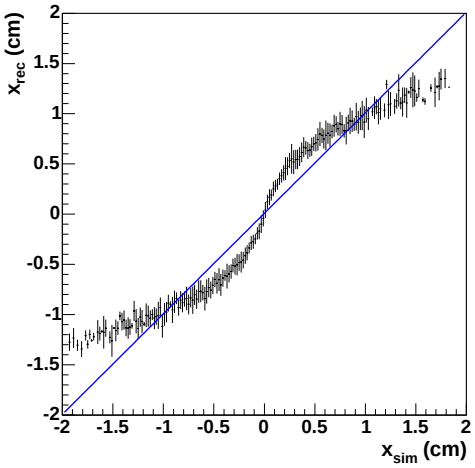

Fig. 6.9: *The average of the coordinate x_{rec}, reconstructed with a corrected weighted mean (eq. 6.4), is plotted against the true incident coordinate, known from the simulation, for a single neutron hitting the calorimeter front-face. The blue line represents a linear least square fit of the distribution.*

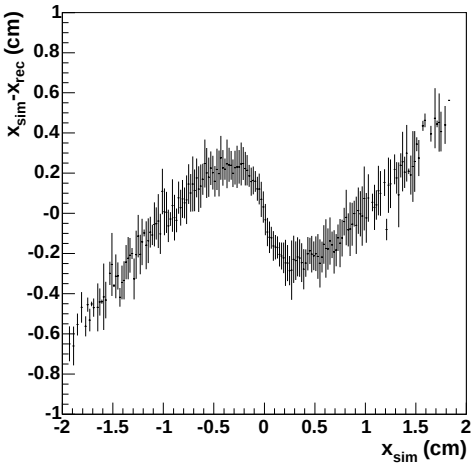

Fig. 6.10: *The average of the difference between the true position and the position calculated with the equation 6.4, is represented as a function of the true position, for a single neutron hitting the calorimeter front-face.*

the neutron multiplicity grows; a resolution value less than 1 mm can be achieved for neutron multiplicity greater than 20. The data are fitted using the function:

$$f(x) = \beta + \frac{\gamma}{x + \delta} \tag{6.5}$$

with $\beta = (0.288 \pm 0.001)mm$, $\gamma = (15.07 \pm 0.05)mm$ and $\delta = (5.35 \pm 0.03)$.

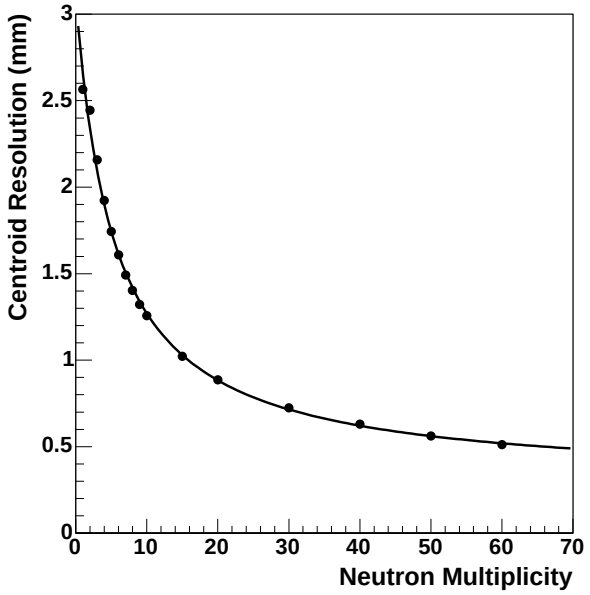

Fig. 6.11: *Resolution on the x-coordinate of the centroid as a function of the neutron multiplicity.*

6.2.3 Centroid coordinate accuracy

In the ALICE experimental sutup the ZN calorimeter will be placed between the two beam pipes, on a support platform, which can move in the vertical direction. On the contrary, the calorimeter center position, in the horizontal transverse direction, will be fixed and aligned with the LHC axis. In order to check the accuracy on the centroid coordinate reconstruction, we perform a simulation with the ZN displaced in the vertical direction from its nominal position. The y coordinate of the spectator neutrons spot centroid as a function of the ZN center vertical position is shown in Fig. 6.12. From the Fig.s 6.12 and 6.13 it is possible to infer that the centroid coordinate,

reconstructed by ZN, is accurate up to 1 cm of ZN center displacement from the nominal position. This feature, which allows to monitor and correct the detector centering, is essential. In fact, as discussed below, the centroid of spectator neutron spot, calculated from the contribution of many events, must be centered on the ZN front face in order to give a correct estimate of the reaction plane, in the single event.

The centroid resolution as a function of the ZN center position is shown in Fig. 6.14 for two different neutron multiplicity.

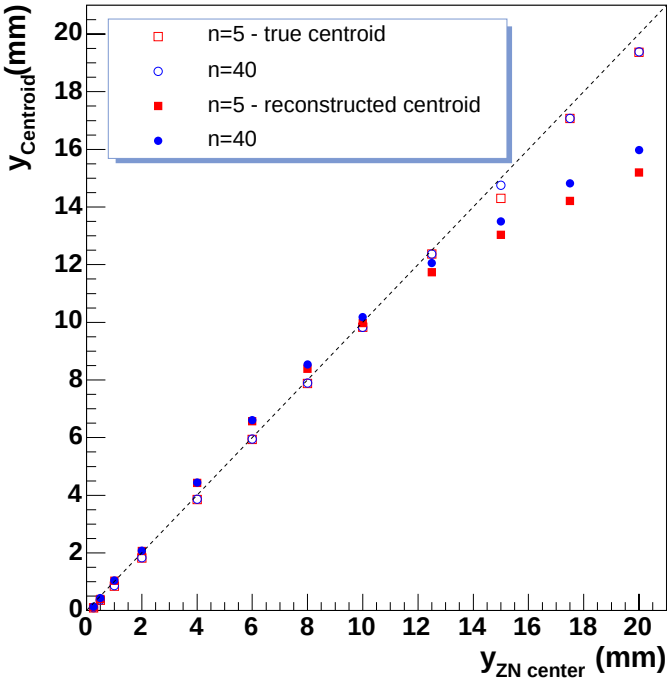

Fig. 6.12: *Centroid vertical coordinate, either true (i.e. known from the simulation) or reconstructed by ZN, as a function of the ZN center vertical position, for two different values of neutron multiplicity.*

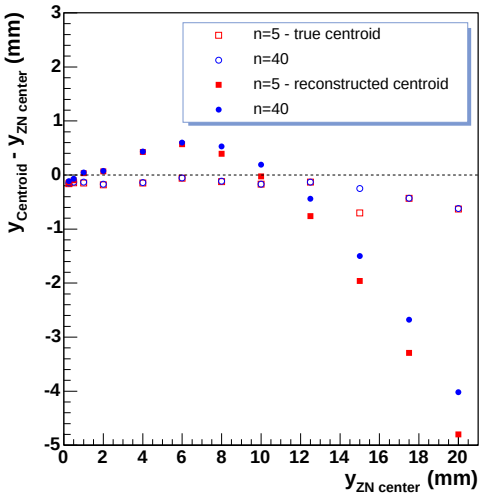

Fig. 6.13: *The difference between the centroid vertical coordinate and the ZN center vertical position is plotted against the ZN center vertical position, for different neutron multiplicity values.*

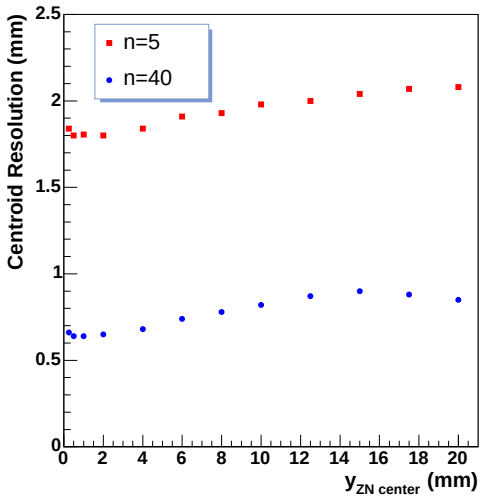

Fig. 6.14: *Resolution on the y-coordinate of the centroid as a function of the detector vertical displacement from the nominal position, for* n_{neutr}*=5, 40.*

6.3 Event plane reconstruction by means of the ZN calorimeter

The ZN localizing capability allows to reconstruct, event by event, the centroid of the spectators neutrons spot on the calorimeter front-face. The centroid position is sensitive to the directed flow v_1, that denotes the sideward deflection (*bounce off*) of the spectators neutrons, due to the expanding fireball. Therefore the centroid measurement allows to reconstruct the 1^{st}-order event plane. The event plane resolution achieved by the ZN calorimeter depends on the magnitude of the directed flow v_1 of spectators neutrons, which is expected to be quite large ($\simeq$20%) and independent of beam energy. In fact, WA98 at the SPS measured a directed flow of protons of the order of 20% in the target fragmentation region. Furthermore, STAR measurements of v_1 calculated from charged particles are in good agreement at forward rapidities with NA49 measurements, when plotted as a function of $y - y_{beam}$. This observation is consistent with the hypothesis of limiting fragmentation in this region and may suggest that v_1 among spectators nucleons could be independent of beam energy between SPS and RICH[34].

6.3.1 Fast simulation technique

The resolution on the event plane reconstructed by means of the ZN calorimeter has been evaluated through a fast simulation. Spectator neutrons have been generated with the beam nucleons energy (2.76 TeV) at the IP and travelled to the ZDC on one side of the interaction point. Their momentum distribution took into account the spread due to Fermi momentum, a transverse beam divergence at the IP (30 μrad) and a transverse beam size at the IP of 16 μm[34, 35, 36]. A random reaction plane azimuth (φ_{RP}) has been assigned to each event. Moreover following the standard prescriptions[39], a directed flow of spectator neutrons v_1 has been introduced, by changing the azimuthal angle of each neutron (and consequently changing the density in the azimuthal angle space):

$$\varphi \rightarrow \varphi' = \varphi + \Delta\varphi \tag{6.6}$$

where

$$\Delta\varphi = -2v_1 sin(\varphi - \varphi_{RP}), \tag{6.7}$$

v_1 represents the directed flow, and φ_{RP} is the reaction plane azimuth assigned to the event. The v_1 parameter has to reverse sign in the backward hemisphere.

The code tracks the spectator neutrons up to the calorimeter front face. From the simulation it is possible to calculate the true spectator neutrons centroid coordinate by means of the equations:

$$x_0 = \frac{\sum_{i=1}^{n} x_i E_i}{\sum_{i=1}^{n} E_i} \qquad y_0 = \frac{\sum_{i=1}^{n} y_i E_i}{\sum_{i=1}^{n} E_i} \tag{6.8}$$

where E_i is the energy of the *i-th* neutron and the sums go over all the n neutrons involved in the event.

Using the information on the centroid position resolution (eq.6.5), a smearing has been assigned to the true coordinates x_0 and y_0 in order to get the centroid coordinates x and y reconstructed from the four ZN tower responses.

Two event plane azimuthal angles can be calculated:

$$\varphi^0_{ZDC} = arctg(\frac{y_0}{x_0}) \tag{6.9}$$

from the true centroid, and

$$\varphi_{ZDC} = arctg(\frac{y}{x}) \tag{6.10}$$

from the reconstructed centroid.

The event plane resolution has been evaluated by means of two estimators. The first estimator is the mean cosine of the angular difference $< cos(\varphi_{ZDC} - \varphi_{RP}) >$. Moreover the angular difference $\varphi_{ZDC} - \varphi_{RP}$ (or $\varphi^0_{ZDC} - \varphi_{RP}$) distributions can be fitted with the superimposition of a gaussian plus a constant function; the variance $\sigma(\varphi_{ZDC} - \varphi_{RP})$ of this gaussian fit is the second estimator of the event plane resolution.

Two different studies have been performed: a simulation of minimum bias events and a parametric study as a function of the neutron multiplicity for three different values of the directed flow of spectator neutrons v_1=5%, 10%, 20%. Furthermore, the influence of the detector granularity and of the LHC beam divergence at the IP on the event plane resolution has been investigated.

6.3.2 Reaction plane estimate for minimum bias events

A first study of the reaction plane azimuthal angle estimation has been performed for events Pb-Pb minimum bias, produced through the Hijing generator. The Fig.6.15 shows the correlation between the neutron multiplicity and the impact parameter for this kind of events. Taking into account the production of nuclear fragments in the nucleus-nucleus collisions, the monotonic correlation between neutron multiplicity and impact parameter is partially destroyed[5]. In the same figure the neutron multiplicity distribution is plotted, showing that the expected maximum number of spectator neutrons is 60, much lower than the number of neutrons in the Pb nucleus.

In Fig.s 6.16-6.18 the results of this study are reported. The correlation between φ_{ZDC} and φ_{RP} allows to appreciate in a qualitative way how well the azimuth of the reaction plane is resolved. Nevertheless a quantitative evaluation of the event plane resolution is given by the two estimators.

For each selected value v_1, a comparison between the angular difference distributions $\varphi^0_{ZDC}-\varphi_{RP}$ and $\varphi_{ZDC}-\varphi_{RP}$ doesn't show significant differences on the event plane resolution, so we can conclude that the resolution on the centroid reconstruction doesn't affect the event plane resolution.

For minimum bias events, the event plane resolution, given as $\sigma(\varphi_{ZDC}-\varphi_{RP})$, is 64° when v_1=5%, 59° when v_1=10% and 48° when v_1=20%.

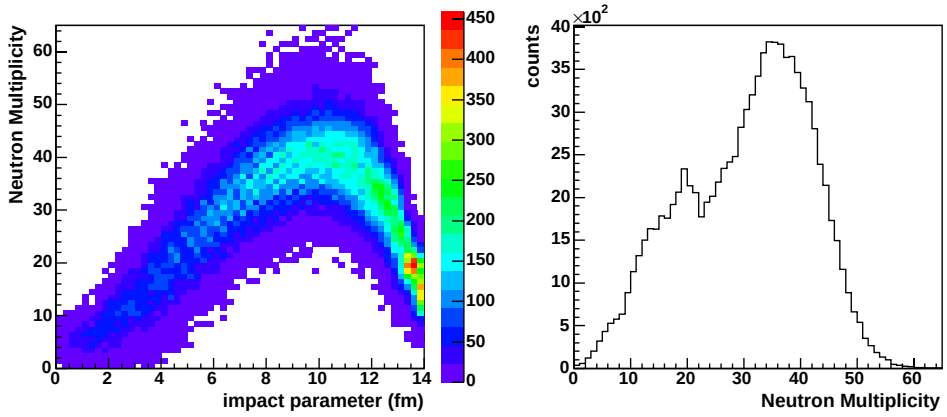

Fig. 6.15: *Correlation between the neutron multiplicity and the impact parameter, for minimum bias Pb-Pb events(left plot). In the right plot the minimum bias neutron multiplicity distribution is shown.*

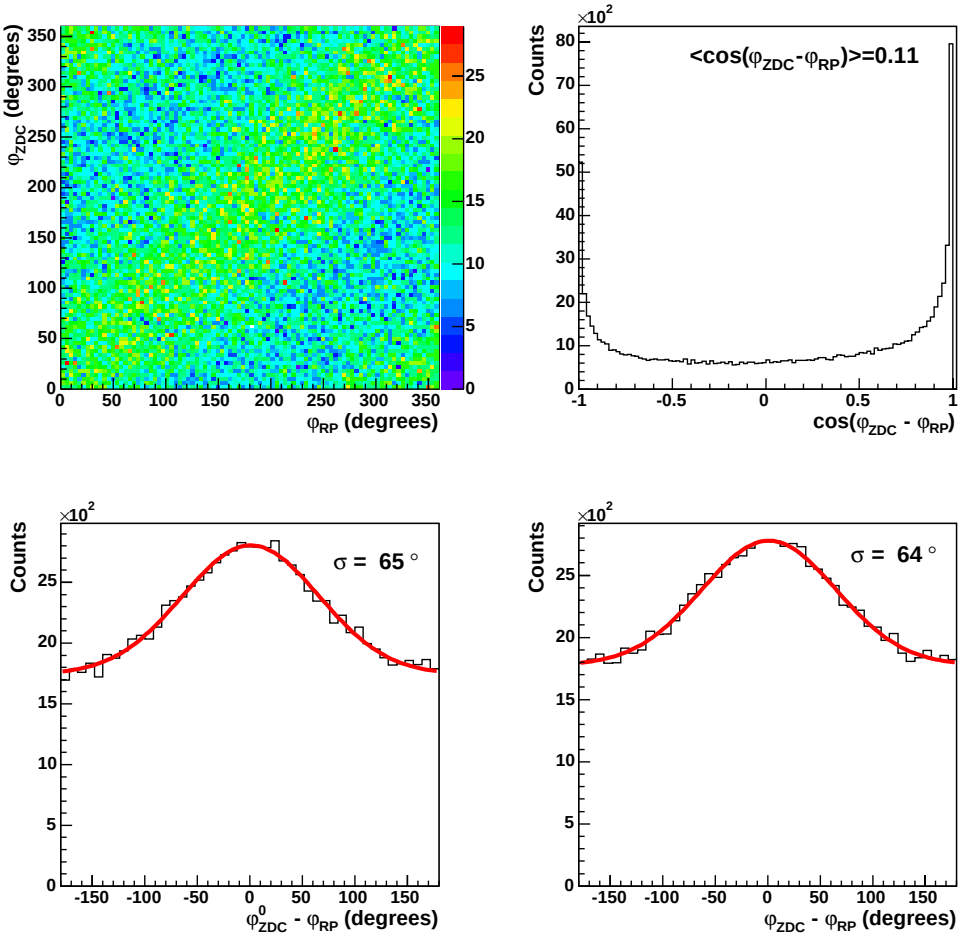

Fig. 6.16: *Reaction Plane estimation for minimum bias events when v_1=5%. The top left plot shows the correlation between φ_{ZDC} and φ_{RP}. Moreover the distributions of the cosine of the angular difference $cos(\varphi_{ZDC} - \varphi_{RP})$ (top right), of the angular difference $\varphi^0_{ZDC} - \varphi_{RP}$ (bottom left) and of the angular difference $\varphi_{ZDC} - \varphi_{RP}$ (bottom right) are represented.*

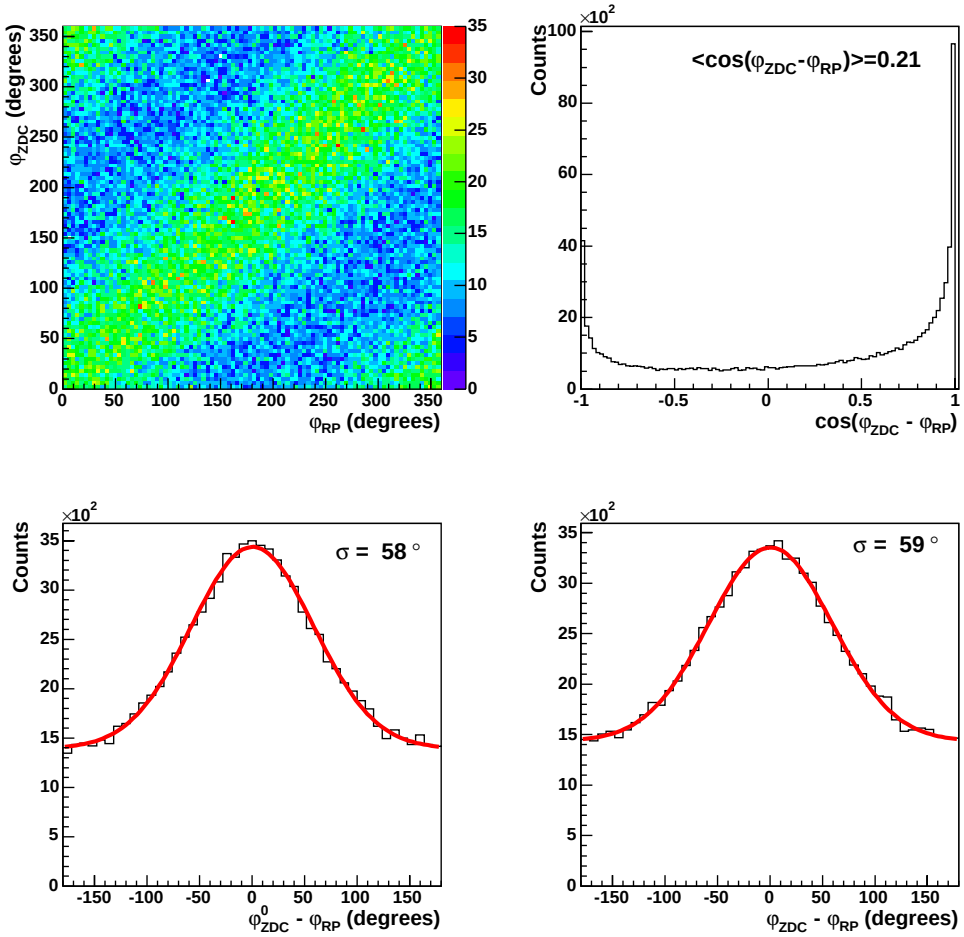

Fig. 6.17: *Reaction Plane estimation for minimum bias events when v_1=10%. The top left plot shows the correlation between φ_{ZDC} and φ_{RP}. Moreover the distributions of the cosine of the angular difference $cos(\varphi_{ZDC} - \varphi_{RP})$ (top right), of the angular difference $\varphi^0_{ZDC} - \varphi_{RP}$ (bottom left) and of the angular difference $\varphi_{ZDC} - \varphi_{RP}$ (bottom right) are represented.*

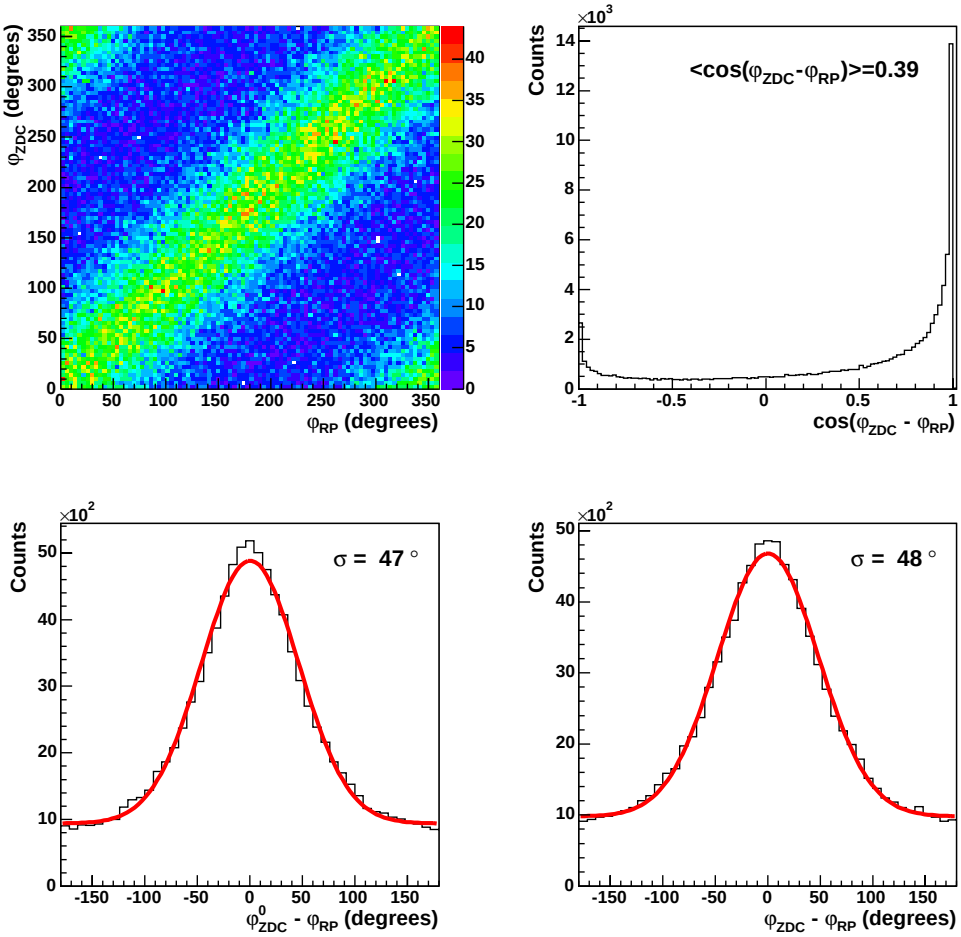

Fig. 6.18: *Reaction Plane estimation for minimum bias events when v_1=20%. The top left plot shows the correlation between φ_{ZDC} and φ_{RP}. Moreover the distributions of the cosine of the angular difference $cos(\varphi_{ZDC} - \varphi_{RP})$ (top right), of the angular difference $\varphi^0_{ZDC} - \varphi_{RP}$ (bottom left) and of the angular difference $\varphi_{ZDC} - \varphi_{RP}$ (bottom right) are represented.*

6.3.3 Reaction plane estimate as a function of the neutron multiplicity

A parametric study of the event plane resolution as a function of the neutron multiplicity n_{neutr} has been performed for three different values of v_1=5%, 10%, 20%. We have studied six different n_{neutr} values, from 5 up to 60, which is roughly the maximum number of emitted neutrons, when the production of nuclear fragments in the collision is taken into account (Fig.6.15).

Fig.s 6.19-6.22 show several examples of the event plane estimation for some values of n_{neutr} and v_1. Also in this case, a comparison between the angular difference distributions $\varphi^0_{ZDC} - \varphi_{RP}$ and $\varphi_{ZDC} - \varphi_{RP}$ shows that the resolution on the centroid reconstruction doesn't affect significantly the event plane resolution.

The results of the whole study are then summarized in Fig.6.23 and in Fig.6.24, where the event plane resolution, expressed respectively as $< cos(\varphi_{ZDC} - \varphi_{RP}) >$ and $\sigma(\varphi_{ZDC} - \varphi_{RP})$, is plotted as a function of n_{neutr}, for the three investigated v_1 values. As expected the event plane resolution depends on the magnitude of v_1 and on a lesser extent on the neutron multiplicity.

The Fig.6.25 displays the results of an analogous study performed on the STAR ZDC-SMD[40, 41]. The value of the event plane resolution estimator $< cos(\varphi_{ZDC} - \varphi_{RP}) >$, for the ALICE ZDC, is of the order of 0.40 when v_1=20% and n_{neutr}=30, slightly better than the value calculated for the STAR ZDC-SMD($\simeq$0.34).

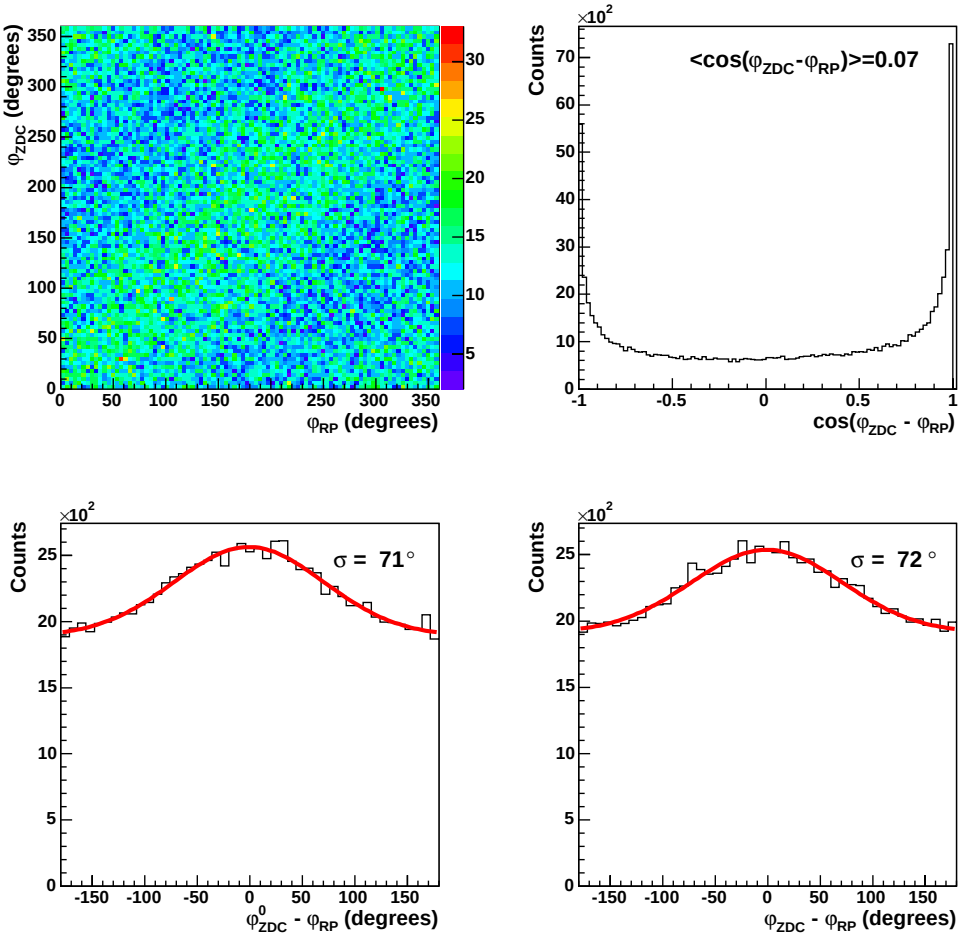

Fig. 6.19: *Reaction Plane estimation for n_{neutr}=5 and v_1=5%. The top left plot shows the correlation between φ_{ZDC} and φ_{RP}. The distributions of the cosine of the angular difference $cos(\varphi_{ZDC} - \varphi_{RP})$ (top right), of the angular difference $\varphi^0_{ZDC} - \varphi_{RP}$ (bottom left) and of the angular difference $\varphi_{ZDC} - \varphi_{RP}$ (bottom right) are represented.*

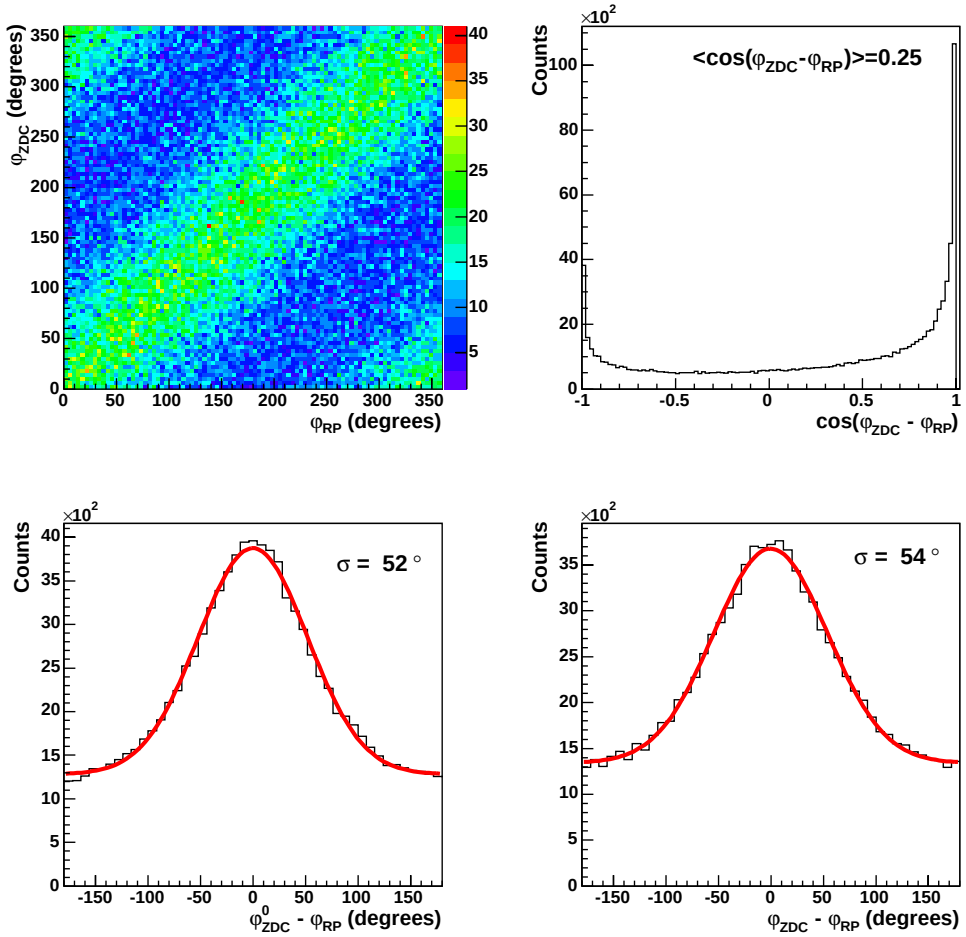

Fig. 6.20: *Reaction Plane estimation for n_{neutr}=5 and v_1=20%. The top left plot shows the correlation between φ_{ZDC} and φ_{RP}. The distributions of the cosine of the angular difference $cos(\varphi_{ZDC} - \varphi_{RP})$ (top right), of the angular difference $\varphi^0_{ZDC} - \varphi_{RP}$ (bottom left) and of the angular difference $\varphi_{ZDC} - \varphi_{RP}$ (bottom right) are represented.*

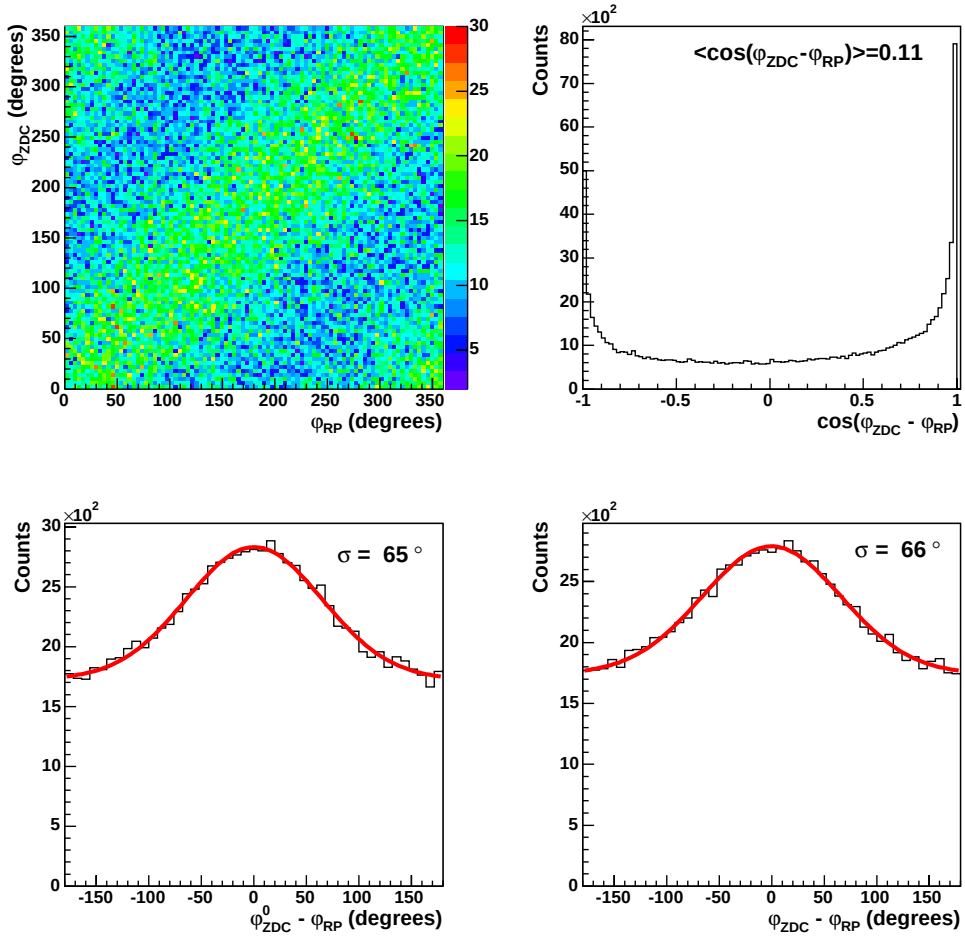

Fig. 6.21: *Reaction Plane estimation for n_{neutr}=40 and v_1=5%. The top left plot shows the correlation between φ_{ZDC} and φ_{RP}. The distributions of the cosine of the angular difference $cos(\varphi_{ZDC} - \varphi_{RP})$ (top right), of the angular difference $\varphi^0_{ZDC} - \varphi_{RP}$ (bottom left) and of the angular difference $\varphi_{ZDC} - \varphi_{RP}$ (bottom right) are represented.*

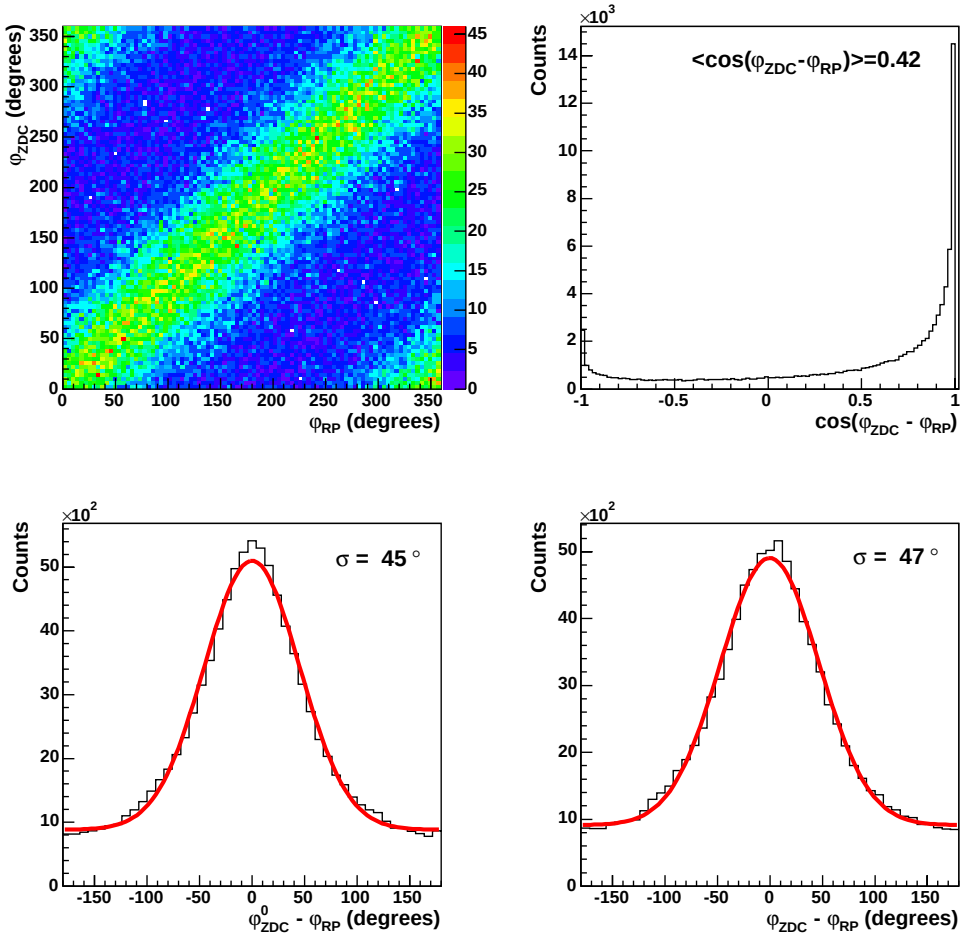

Fig. 6.22: *Reaction Plane estimation for n_{neutr}=40 and v_1=20%. The top left plot shows the correlation between φ_{ZDC} and φ_{RP}. The distributions of the cosine of the angular difference $cos(\varphi_{ZDC} - \varphi_{RP})$ (top right), of the angular difference $\varphi^0_{ZDC} - \varphi_{RP}$ (bottom left) and of the angular difference $\varphi_{ZDC} - \varphi_{RP}$ (bottom right) are represented.*

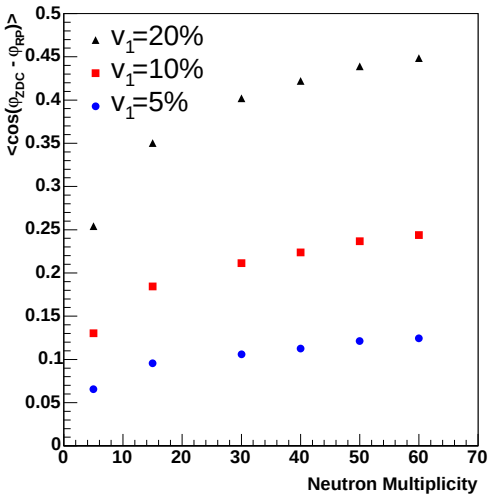

Fig. 6.23: *Reaction plane figure of merit for the ALICE ZDC. The event plane resolution, expressed as the mean cosine of the angular difference, is plotted against the neutron multiplicity.*

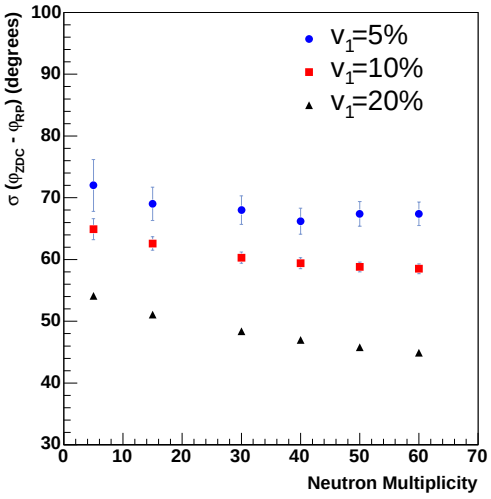

Fig. 6.24: *Event plane resolution, expressed as the variance of the angular difference $\sigma(\varphi_{ZDC} - \varphi_{RP})$, as a function of the neutron multiplicity.*

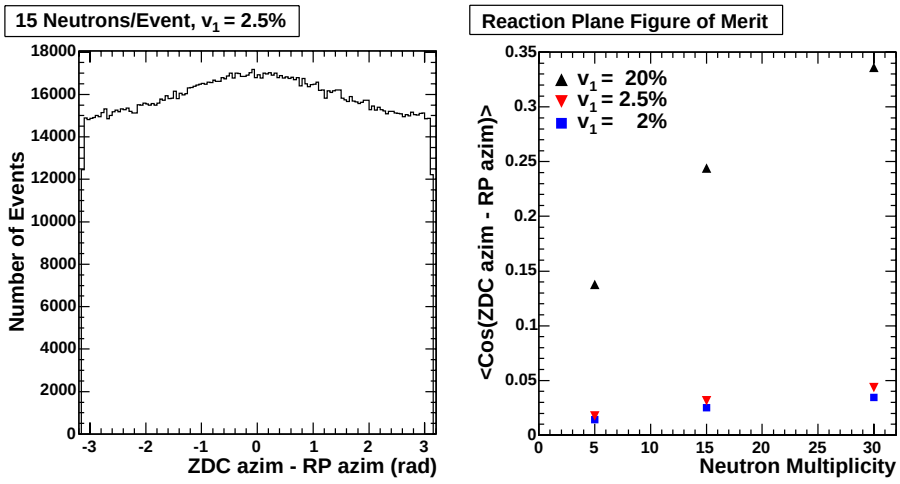

Fig. 6.25: *Reaction plane estimate in a simulation performed for the STAR ZDC-SMD. The left plot shows the angular difference $\varphi_{ZDC} - \varphi_{RP}$ distribution for n_{neutr}=15, and v_1=2.5%. On the right the reaction plane figure of merit is represented.*

6.3.4 LHC beam parameters contribution to the event plane resolution

The above study of the reaction plane estimate as a function of the neutron multiplicity has been performed taking into account a transverse beam divergence at the IP(30 μrad) and a transverse beam size at the IP of 16 μm (see Par.6.3.1). The smearing due to the reconstructed centroid position resolution has been also considered. The Fig.6.26 allows to appreciate the different contributions of the detector and of the LHC beam parameters to the event plane resolution, for the particular case of v_1=20%. When we turn off the detector contribution, i.e. the smearing due to the centroid position, only a slight improvement on the reaction plane resolution is obtained. On the contrary, if also the beam parameters, i.e. the beam transverse size and the beam divergence at the IP, are switched off, the reaction plane resolution improvement is significant: for example, the value of the estimator $< cos(\varphi_{ZDC} - \varphi_{RP}) >$ changes from 0.4655 to 0.8038, for n_{neutr}=60. Moreover, for the same neutron multiplicity n_{neutr}=60, we verified that, when the detector smearing and the beam divergence are disabled, the resolution

estimator has essentially the same value whether the beam transverse size at the IP is taken into account, $< cos(\varphi_{ZDC} - \varphi_{RP}) >$=0.8036, or not, $< cos(\varphi_{ZDC} - \varphi_{RP}) >$=0.8038. Therefore the event plane resolution predicted for the ALICE ZN is dominated by the bias due to the transverse Pb beam divergence at IP2, which is foreseen to be 30 μrad, depending on different LHC beam parameters as shown in the relation:

$$\theta_{RMS} = \sqrt{\frac{\varepsilon_n}{\beta^* \cdot \gamma}} \tag{6.11}$$

where ε_n=1.5μm rad is the transverse normalized emittance, β^*=0.5 m at IP2 is the Twiss function and γ=2963.5 is the relativistic gamma factor[42].

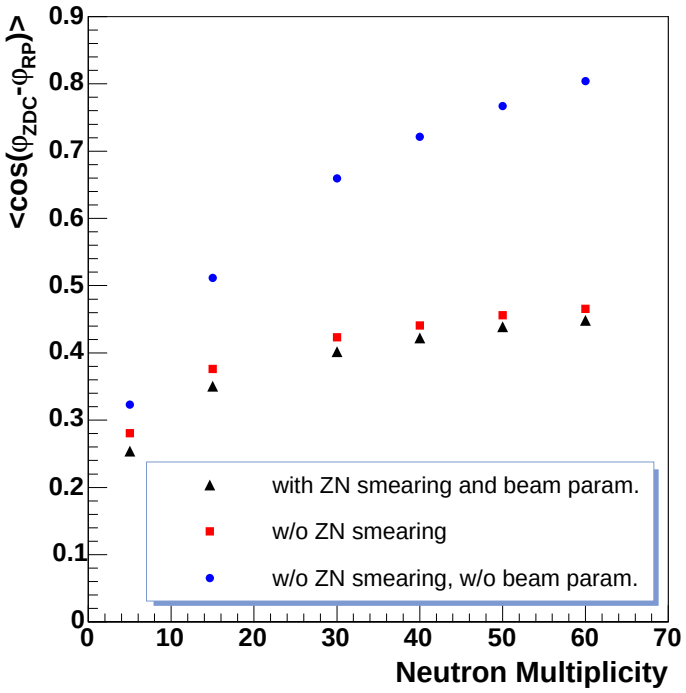

Fig. 6.26: *Detector and beam parameters contributions to the event plane resolution.*

6.3.5 Centroid position versus directed flow v_1

Event by event the spectator neutrons suffer a kick, due to a directed flow v_1 different from 0, that shifts the neutron spot centroid from its nominal position. However when we sum many events whose reaction plane azimuth (φ_{RP}) is generated random between 0 and 2π, as in the real case, the global effect of a directed flow $v_1 \neq 0$ is a widening of the neutron spot on the ZN front face and not a spot displacement, with respect to the case in which $v_1 = 0$. Therefore, in order to get a quantitative estimate of the spectator neutrons centroid shift as a function of the directed flow v_1, we performed a simulation keeping φ_{RP}=0. The Fig.s 6.27 - 6.29 show the results of this study for a neutron multiplicity n_{neutr}=40. Furthermore we verified that the centroid position does not depend on the neutron multiplicity. In fact, for example, a directed flow v_1=20% produces a shift of the spectator neutrons spot centroid on the ZN front face of the order of 1.67 mm, for n_{neutr}=40, and of 1.69 mm, for n_{neutr}=60.

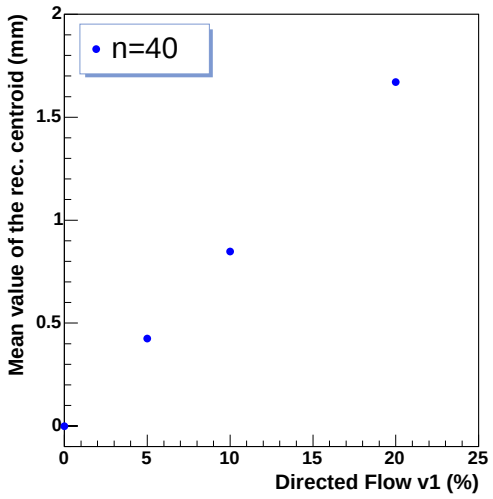

Fig. 6.27: *Shift of the centroid of spectator neutrons spot on the ZN front face plotted against the directed flow v_1.*

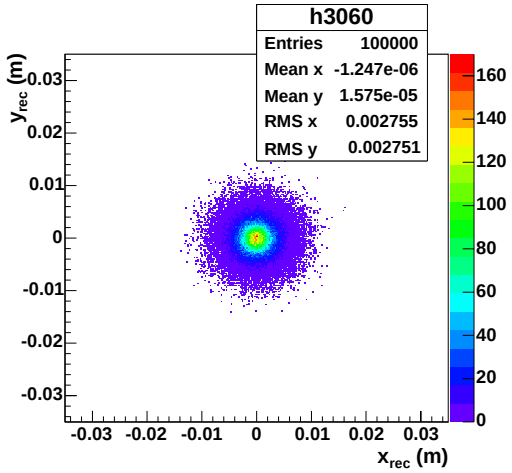

Fig. 6.28: *Reconstructed centroid distribution on ZN front face when v_1=0%; for this study φ_{RP}=0.*

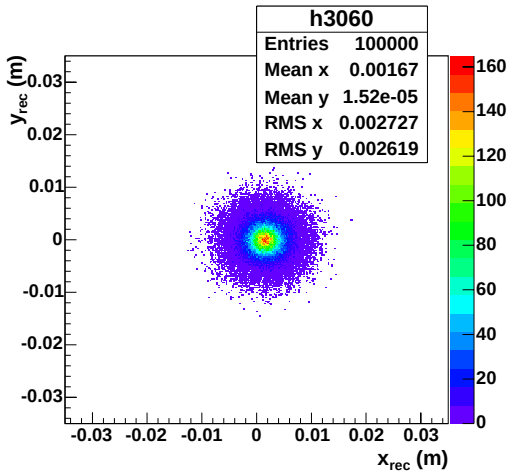

Fig. 6.29: *Reconstructed centroid distribution on ZN front face when v_1=20%; φ_{RP}=0.*

6.3.6 Detector granularity effect on the event plane resolution

The study of the resolution on the centroid reconstructed coordinate and of the event plane resolution as a function of the neutron multiplicity has been repeated considering an hypothetical 4×4 segmentation (Fig.6.30). As can be seen in Fig.6.31, the resolution on the reconstructed centroid position improves going from 2×2 to 4×4 segmentation. However this centroid resolution improvement results in a almost negligible difference in the event plane resolution (Fig.6.32). In fact, as discussed above (Par.6.3.4), the resolution on the event plane, estimated through the ZN calorimeter, is dominated by the bias due to the beam divergence.

Fig. 6.30: *Schematic representation of the 2×2 (a) and 4×4 (b) ZN segmentations.*

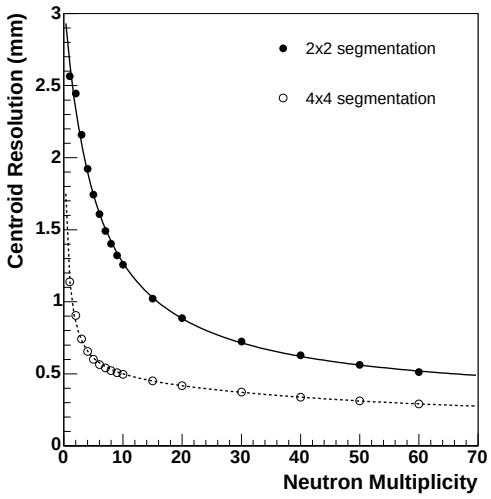

Fig. 6.31: *Resolution on the x-coordinate of the centroid as a function of the neutron multiplicity for the two considered ZN segmentations.*

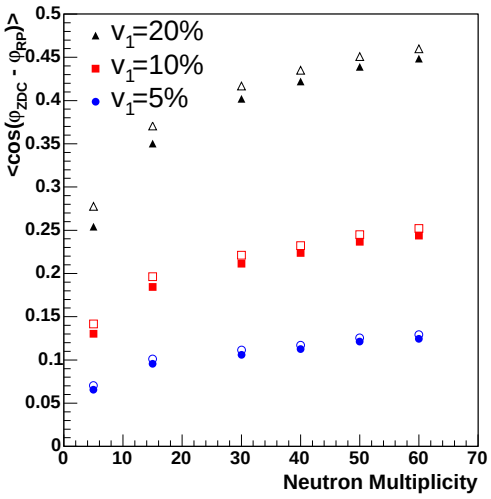

Fig. 6.32: *Event plane resolution, expressed as the mean cosine of the angular difference* $< cos(\varphi_{ZDC} - \varphi_{RP}) >$*, as a function of the neutron multiplicity, for 2×2 (full marker) and 4×4 (open marker) ZN segmentations.*

Appendix A

Simple calculation of the participant and spectator number in central collisions

We suppose that the projectile nucleus has a mass number B and a radius $R = r_0 B^{\frac{1}{3}}$, while the target nucleus has a mass number A and a radius $r = r_0 A^{\frac{1}{3}}$, where r_0 is the nuclear radius parameter ($\approx 1.16 fm$).
We are considering central collisions (*impact parameter b=0*) in the case $B > A$ (see Fig.A.1).

Here we use a very simple geometrical model, where the the nucleus is approximated to a rigid sphere with a uniform nucleon distribution.

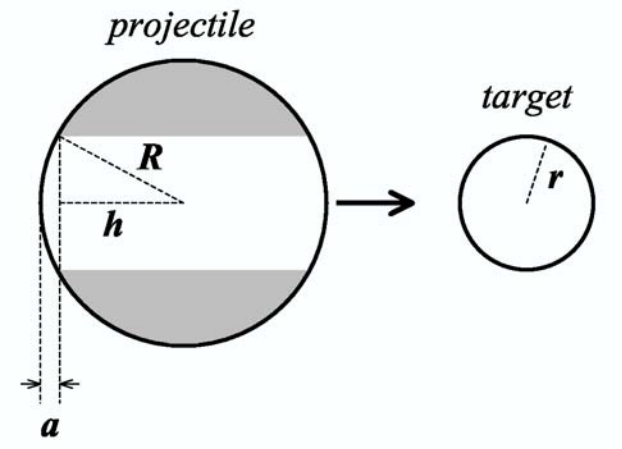

Fig. A.1: *Schematic representation of a central collision between a projectile nucleus with a mass number B and a target nucleus with a mass number A.*

Simple calculation of the participant and spectator number in central collisions

In this model the nuclear density of the projectile nucleus is simply described as:

$$\rho = \frac{B}{\frac{4}{3}\pi R^3} = \frac{3B}{4\pi R^3} \tag{A.1}$$

Moreover in this model the participating projectile nucleons are contained in the volume V mapped out by the cross-section of the target nucleus [3] (see Fig.A.1):

$$\begin{aligned} V &= 2\left\{\pi\frac{a}{2}r^2 + \frac{4}{3}\pi\left(\frac{a}{2}\right)^3 + \pi r^2 h\right\} \\ &= \frac{1}{3}\pi a^3 + 2\pi r^2 R - \pi r^2 a \end{aligned} \tag{A.2}$$

where $h = \sqrt{R^2 - r^2} = R - a$ and $a = R - \sqrt{R^2 - r^2}$.

Hence, in this simple framework, the number of projectile participants is:

$$\begin{aligned} N_p^{proj} &= \rho V \\ &= \frac{B}{4}\left\{\left(\frac{a}{R}\right)^3 + 6\left(\frac{r}{R}\right)^2 - 3\left(\frac{r}{R}\right)^2\left(\frac{a}{R}\right)\right\} \end{aligned} \tag{A.3}$$

If we put $x \equiv \left(\frac{r}{R}\right)^2 = \left(\frac{A}{B}\right)^{\frac{2}{3}}$ we obtain:

$$\begin{aligned} N_p^{proj} &= \frac{B}{4}\left\{(1-\sqrt{1-x})^3 + 6x - 3x(1-\sqrt{1-x})\right\} \\ &= B - B(1-x)^{\frac{3}{2}} \\ &= B - B\left(1 - \left(\frac{A}{B}\right)^{\frac{2}{3}}\right)^{\frac{3}{2}} \end{aligned} \tag{A.4}$$

Therefore the projectile participant number N_p^{proj}, for a central collision, is given by the equation:

$$N_p^{proj} = B - A\left[\left(\frac{B}{A}\right)^{\frac{2}{3}} - 1\right]^{\frac{3}{2}} \tag{A.5}$$

while for the spectator number N_s we get:

$$N_s = B - N_p^{proj} = A \left[\left(\frac{B}{A} \right)^{\frac{2}{3}} - 1 \right]^{\frac{3}{2}}. \tag{A.6}$$

Bibliography

[1] H.Satz, hep-ph/0405051

[2] ALICE Physics Performance Report - Vol.I

[3] H.R.Schmidt and J.Schukraft, CERN-PPE/92-42.

[4] ALICE Physics Performance Report - Vol.II

[5] Zero Degree Calorimeter Technical Design Report, CERN/LHCC, 1999.

[6] R. Arnaldi et al., *Nucl. Instr. Meth. A 411 (1998)* 1.

[7] R.Arnaldi et al., *Nucl. Instr. Meth. A 456 (2001)* 248.

[8] R.Arnaldi et al., *Nucl. Instr. Meth. A 564 (2006)* 235.

[9] P.Gorodetzky et al., *Nucl. Instr. Meth. A 361 (1995)* 161.

[10] C.Oppedisano, Ph.D.Thesis, 2001.

[11] http://aliceinfo.cern.ch/Offline

[12] http://root.cern.ch

[13] LHC Functional Specification, Function and operating conditions of the TCDD injection mask,CERN 2004.

[14] Engineering Change Order, New layout of injection protection elements around IP2 and IP8, CERN, 2004.

[15] Engineering Change Order, Integration of tertiary collimators, beam-beam rate monitors and space reservation for a calorimeter in experimental LSS's, CERN, 2004.

[16] R. Wigmans, *Nucl. Instr. Meth. A 265 (1988)* 273.

[17] D. E. Groom, *Proc. Seventh Inter. Conf. on Calorimetry in High Energy Physics, Tucson, Arizona, 9-14 November 1997, ed. by E. Cheu, T. Embry, J. Rutherfoord, R. Wigmans.*, World Scientific, Singapore, (1998).

[18] E.Chiavassa et al., *Nucl. Instr. Meth. A 367 (1995)* 267.

[19] R.Arnaldi et al., Proc. of 2004 IEEE NSS/MIC/SNPS and RTDS International Conference, Rome, Italy, October 16-22, 2004.

[20] R.Arnaldi et al., Conference on Calorimetry in Particle Physics, CALOR2006, Chicago, USA, June 5-9, 2006.

[21] N. de Marco et al., Proc. of 2006 IEEE NSS/MIC/SNPS and RTDS International Conference, San Diego, USA, October 29 - November 4, 2006.

[22] A.S. Ayan et al., *J.Phys.G:Nucl.Part.Phys. N33-N44 (2004)* 30.

[23] http://cern.ch/gatignon/partprod.html

[24] N. Akchurin et al., *Nucl. Instr. Meth. A 408 (1998)* 380.

[25] ALICE Internal Note ALICE 2002-036.

[26] GEANT 3.21, CERN Program Library Long Writeup W5013.

[27] http://wwwasdoc.web.cern.ch/wwwasdoc/psdir/fritiof.ps.gz

[28] R.Arnaldi, Study of the J/Ψ suppression in Pb-Pb collisions at the CERN SPS as a function of the centrality measured with a Zero Degree Calorimeter, Ph.D.Thesis, 2000.

[29] C. W. De Jager, H. de Vries and C.de Vries, Atomic data and Nuclear Data Tables 36(1987) 495.

[30] H.R. Collard, L.R.B. Elton, R.Hofstadter, H.Shopper, Landolt-Bornstein, Numerical data and functional relationships in science and technology, Vol.2, Springer-Verlag (1967).

[31] http://geant4.cern.ch/G4UsersDocuments/UsersGuides/PhysicsReferenceManual/html/node131.html

[32] F. Prino, "Analisi del flow con il metodo dei coefficienti di Fourier", 1° Convegno Nazionale sulla fisica di ALICE, Catania, 11-12 gennaio 2005.

[33] ALICE Physics Performance Report - Vol.II, Part 1, 359-361.

[34] ALICE Physics Performance Report - Vol.II, Part 1, 192-195.

[35] N. De Marco, "Reaction plane determination with ALICE ZDC", Alice Physics Week, Erice, December 5-9, 2005.

[36] R.Gemme, "Determinazione del piano di reazione negli urti nucleo-nucleo con il calorimetro a zero gradi per neutroni di ALICE", XCII Congresso Nazionale Societa' Italiana di Fisica SIF 2006, Torino 18-23 settembre 2006.

[37] T.C. Awes et al., *Nucl. Instr. Meth. A 311 (1992)* 130.

[38] M. Farina, "Risoluzione spaziale del calorimetro a zero gradi di ALICE", Degree Thesis, 2005.

[39] A. M. Poskanzer and S. A. Voloshin, Physical review C, vol. 58, n. 3 (1998), 1671.

[40] G.Wang, Ph.D Thesis, 2006.

[41] H.Crawford et al, STAR ZDC-SMD proposal, STAR note SN-0448 (2003).

[42] LHC Design report Vol.I, Chap.21 - http://ab-div.web.cern.ch/ab-div/Publications/LHC-DesignReport.html

List of Figures

List of Tables